(SZENT ISTVÁN UNIVERSITY formerly)

GRANULAR MATERIAL BEHAVIOUR: EXPLORING PARTICLE INDEXES AND WHEAT PACKING DENSITY

PhD Dissertation by

Mu'ath S. Talafha

Gödöllő
2024

Doctoral school

Denomination: Doctoral School of Mechanical Engineering

Science: Mechanical Engineering

Leader: Prof. Dr. Gábor Kalácska, DSc
Institute of Technology
Hungarian University of Agriculture and Life Sciences

Supervisor: Dr. Oldal István, PhD
Institute of Technology
Hungarian University of Agriculture and Life Sciences

……..…… ….....……

Affirmation of supervisor Affirmation of head of school

Table of Contents

ABBREVIATIONS AND SYMBOLS

Symbol	Explanation	Unit
η	Dimensionless elongation parameter	-
φ	Volume fraction	-
ε	Porosity	-
ev	Void fraction	-
V_{grains}	Volume of grains	m^3
V_{total}	Total volume	m^3
V_{empty}	Volume of voids	m^3
a	Major axis length	m
b	Intermediate axis length	m
c	Minor axis length	m
V	Object's volume	m^3
S	Actual surface area	m^2
S_n	Nominal surface area	m^2
e_{yx}	Elongation parameter (b/a)	-
e_{zx}	Elongation parameter (c/a)	-
e_{zy}	Elongation parameter (c/b)	-
m_i	Mass of particle i	kg
$\boldsymbol{v}_i$	The translational velocity of particle i	m/s
t	Time	s
F_{ij}^{n}	Normal force between particles i and j	N
F_{ij}^{t}	The tangential force between particles i and j	N
g	Gravitational acceleration	m/s^2
Ii	Moment of inertia of particle i	$kg*m^2$
ω_i	The rotational velocity of particle i	rad/s
$\boldsymbol{R}_i$	The vector from the centre of particle i to the contact point	m
τ_{ij}^{r}	Rolling friction torque between particles i and j	N*m
μr	Coefficient of rolling friction	-
$\hat{\omega}_i$	Unit angular velocity of particle i	rad/s
$\boldsymbol{Ri}$	The radius of particle i	m
$\boldsymbol{R}_j$	The radius of particle j	m
$\boldsymbol{r}_i$	Position of particle i (centre)	m
$\boldsymbol{r}_j$	Position of particle j (centre)	m
$\boldsymbol{v}_i$	The velocity of particle i	m/s
$\boldsymbol{v}_j$	The velocity of particle j	m/s
n_{ij}	The normal unit vector between centres of particles i and j	-
v_{ij}	Relative velocity between particles i and j	m/s
v_{ij}^{n}	Relative velocity in the normal direction	m/s
v_{ij}^{t}	Relative velocity in the tangential direction	m/s
$\hat{t}_{ij}$	Tangential unit vector	-
$\boldsymbol{k}_n$	Normal stiffness	N/m

$\boldsymbol{k_t}$	Tangential stiffness	N/m
$\boldsymbol{\eta_n}$	Normal damping coefficient	Ns/m
$\boldsymbol{\eta_t}$	Tangential damping coefficient	Ns/m
$\boldsymbol{\mu_s}$	static Friction coefficient	-
δ_{ij}^{n}	Normal displacement	m
δ_{ij}^{t}	Tangential displacement	m
v_{ij}^{s}	Slip velocity	m/s
μ	Friction coefficient	-
μr	Coefficient of rolling frictions	-
$\boldsymbol{E^*}$	Equivalent Young's Modulus	Pa
$\boldsymbol{R^*}$	Equivalent radius	m
$\boldsymbol{m^*}$	Equivalent mass	m
S_n	Normal contact stiffness	N/m
ψ	Damping ratio coefficient	-
F_{ij}^{n}	Normal force	N
F_{ij}^{t}	Tangential force	N
S_t	Tangential contact stiffness	N/m
$\boldsymbol{e}$	Coefficient of restitution	-
$\boldsymbol{G^*}$	Equivalent shear modulus	Pa
D_i	Displacement of the vibration desk	m
A	Amplitude	m
ω	Frequency	rad/s
t	Vibration time	s
ϕ_0	Initial phase angle	rad
R	Average particle radius	m
G	Particle shear stiffness	Pa
υ	Poisson's ratio	-
$T_{Rayleigh}$	Rayleigh time	s
ρ	Density	kg/m^3
C_{rp}	Coefficient of restitution for particles	-
C_{rw}	Coefficient of restitution for walls	-
μ_{0p}	Coefficient of static friction for particles	-
μ_{0w}	Coefficient of static friction for walls	-
μ_{rp}	Coefficient of rolling friction for particles	-
μ_{rw}	Coefficient of rolling friction for walls	-
S	Displacement	mm
f	Vibration frequency	Hz
t	Vibration time	s
Φ	Primary phase	-
ρ	Packing density	-
V_p	Volume of particles	m^3
V_c	The volume occupied in the container	m^3
m_p	Mass of particles	kg
ρ_p	The theoretical density of particles	kg/m^3
$\overline{H}$	Mean height of packing structure	m

D	The inner diameter of the container	m
φ	Internal friction angle	Degrees
τ	Shearing stress	Pa
σ	Normal stress	Pa
N	Normal load	N
T_{AR}	Shear load with respect to Aspect ratio	pa
T_{SI}	Shear load with respect to size index	pa
V_{SPH}	Volumetric Strain with respect to Sphericity index	%
V_{SI}	Volumetric Strain with respect to size index	%
c_{11}	model parameter	-
c_{12}	model parameter	-
c_{21}	model parameter	-
c_{22}	model parameter	-
c_{31}	model parameter	-
c_{32}	model parameter	-
c_{33}	model parameter	-
c_{41}	model parameter	-
c_{42}	model parameter	-
c_{51}	model parameter	-
c_{52}	model parameter	mm^-1
τ	Characteristic time of the process	s
ρ_i	Initial packing density	-
ρ_f	Final packing density	-
$\rho_{(t)}$	Time-varying particle packing density	-
$\rho_{(A)}$	amplitude-varying final packing density of wheat	-

Abbreviations

DEM	Discrete Element Method
SST	Simple Shear Test
AR	Aspect Ratio
SI	Size Index
TPSI	Triple Particle Size Index
SPH	Sphericity Index
FEM	Finite Element Method
SPHy	Smoothed Particle Hydrodynamics
PFEM	Particle Finite Element Method
ODE	Ordinary Differential Equation
GUI	Graphical User Interface
CAD	Computer-Aided Design
CFD	Computational Fluid Dynamics
AI	Angularity Index
NGI	Norwegian Geotechnical Institute
HCA	Hollow Cylinder Apparatus
RLP	Random Loose Packing
RCP	Random Close Packing
3D	Three-dimensional
Amp.	Amplitude

EDEM	Software for Discrete Element Method Simulations
HMN	Hertz Mindlin No-Slip
kPa	Kilopascal
Hz	Hertz
RPM	Revolutions Per Minute
mm	Millimeter
g	Gram
R^2	Coefficient of determination
CN	Coordination Number
PMMA	Polymethyl Methacrylate

1 INTRODUCTION, OBJECTIVES

1.1 Introduction

The Discrete Element Method (DEM) is a powerful numerical technique that simulates the behaviour of granular and particulate materials. Initially developed in the 1970s (Cundall and Strack, 1979), DEM has become a widely used tool in various fields, including geomechanics, civil engineering, pharmaceuticals, and food processing. The method operates by treating each particle as a discrete entity with its behaviour, considering its size, shape, and interactions with neighbouring particles and external loads (Richards et al., 2004). This results in a highly accurate and detailed representation of the complex behaviour of granular materials, including particle-particle interactions, bulk flow, and failure mechanisms. The advantages of DEM include its ability to capture the heterogeneity and anisotropy of granular materials, the possibility of investigating particle-scale phenomena and predicting macroscopic behaviour, and the potential for optimising processes and designs in various industries (Jing and Stephansson, 2007; Qi et al., 2015; Wang et al., 2022). Despite its widespread use, challenges and limitations exist in DEM, such as the computationally expensive nature of simulations, the need for accurate calibration of input parameters, and the difficulty of modelling complex geometries and boundary conditions. Nevertheless, the potential benefits of DEM in advancing our understanding and engineering of granular materials make it a promising and exciting area of research.

Additionally, The Simple Shear Test (SST) is a commonly used experimental technique for evaluating the mechanical behaviour of granular materials under shear loading. The SST involves the confinement of a sample of particles between two parallel containers and the translation of one container horizontally concerning the other, which produces a shear strain within the sample. The resulting stress-strain curve can provide valuable insights into the frictional and rheological properties of the material, which are crucial for predicting its behaviour in various engineering applications. However, the accuracy and reliability of SST results depend on several factors, including particle shape, size, surface properties, sample preparation, and testing conditions. Numerous studies have highlighted the significant effect of particle indexes, such as size distribution, shape factor, angularity index, sphericity index, and surface roughness, on the SST results. For instance, (Altuhafi et al., 2016) found that the coefficient of friction measured in SST increases with the shape factor of particles and decreases with particle size.

Similarly, (Danesh et al., 2020) investigated the influence of the angularity index and sphericity index on the shear strength of the ballast layer and the formation of a shear band using discrete element methods. Furthermore, (Kodicherla et al., 2019) examined the impact of the dimensionless elongation parameter (η) on the direct shear behaviour of granular materials using DEM. Similarly, (Kodicherla et al., 2019) reported that the degree of particle crushing and the evolution of particle size distribution during SST significantly affect the shear strength and deformation behaviour of sand samples. However, a detailed investigation of the specific effect of each particle index on SST is still lacking.

Furthermore, The efficient packing of granular materials has significant applications in various fields, from food processing and pharmaceutical manufacturing to civil engineering and geology (Chatham et al., 2019; Chen et al., 2020; Bharathi and Sampath kumar, 2022). Achieving higher packing densities than those attainable with mono-disperse cylindrical or spherical particles alone is a subject of ongoing research interest. To this end, mixed particle systems, such as combinations of cylinders and spheres, have been investigated through numerical simulations and experimental studies, demonstrating their effectiveness in achieving denser packing (Qian et al., 2016; Zhao et al., 2019; Fitzgerald et al., 2020).

However, the complex interplay between particle shape, size, and surface properties, as well as the influence of external factors such as mechanical vibration and applied stress, make the

optimisation of mixed particle packing a challenging and multi-disciplinary task. In recent years, research has focused on the factors that influence the packing density of mixed particle systems or binary mixtures based solely on diameter considerations (Zhao et al., 2019; Kiełbasa et al., 2021) or centred on the combination of spheres and fibres with a high aspect ratio (Wang et al., 2021), with a particular focus on cylindrical particles due to the wide use in practical and industrial fields (Zhang et al., 2015). However, the combined effect of mechanical vibration and normal stress on wheat packing density has not been explored through practical experiments and advanced analytical techniques.

Therefore, the present thesis aims to contribute to a better understanding of the factors that influence the packing density of mixed particle systems by employing practical experiments and advanced analytical techniques, with a particular focus on wheat particles by studying the combined effect of mechanical vibration and normal stress by identifying the optimal conditions for achieving high wheat packing density. This study seeks to identify the optimal conditions for achieving high wheat packing density and develop strategies to improve the accuracy and reliability of such measurements. Additionally, this study aims to investigate the specific effect of particle shape, including sphericity index SPH, Aspect Ratio AR, Size Index and Triple Particle size index TPSI, on the SST results for granular materials, where the SPH and AR dealing with the particles shape and the SI and TPSI deal with the particles size. By applying advanced analytical techniques, "DEM simulations", to investigate the influence of particle indexes on the macro-mechanical properties of granular materials under SST. The study involves varying particle size by increasing and decreasing the size index, adjusting the double particle clump size by 25% and 50% and manipulating the shape index by forming elongated particles from a clump initially formed as a complete sphere. The research will measure several parameters, including volume strain, stress-strain, the thickness of the shearing zone, coordination number, and particle rotation, to determine their correlation with each particle index.

This study aims to contribute to a comprehensive understanding of the mechanical behaviour of granular materials under shear deformation, with implications for various fields such as civil engineering and geology. By investigating the behaviour of granular materials and wheat particles under different conditions, the study provides valuable insights into their behaviour and offers practical implications for industries. Additionally, the study focuses on improving the accuracy and reliability of wheat packing density measurements, offering strategies to enhance measurement techniques. Furthermore, the research strives to strengthen the understanding of the mechanical behaviour of granular materials, thereby facilitating the optimisation of industrial processes involving such materials. Overall, this study encompasses a broad range of objectives, methods, and significant results, shedding light on the mechanical behaviour of granular materials and their practical applications across various industries.

1.2 Objectives

Due to their widespread use in various industrial applications, granular materials are paramount in understanding their mechanical behaviour. This study investigates the influence of critical parameters, such as sphericity index, particle size, and mechanical vibrations, on the behaviour of granular materials under different conditions. By exploring these factors, this research aims to provide insights that contribute to a comprehensive understanding of their behaviour and offer practical implications for optimising industrial processes and achieving optimal packing density.

1. Investigate the influence of particles' Sphericity index (SPH) on the Simple Shear Test (SST) outcomes for granular materials.
2. Examine the impact of the double particle Size index (SI) on the results of the SST for granular materials.
3. Explore the effect of the triple particle size index (TPSI) on the Simple Shear Test (SST) outcomes for granular materials.

4. Investigate the synergistic impact of mechanical vibration and normal stress on wheat particles' packing density, aiming to identify optimal conditions for achieving high packing density.
5. Provide comprehensive insights into the mechanical behaviour of granular materials and wheat particles across diverse conditions, contributing to an improved understanding of their behaviour.

The research objectives converge to enrich our understanding of granular materials' mechanical behaviour significantly, offer insights into optimising industrial processes, and propose practical solutions for enhancing measurements and achieving high packing density in mixed particle systems. By systematically investigating critical parameters like sphericity index, particle size, and mechanical vibrations, this research aims to bridge the gap between theoretical knowledge and practical application, ultimately contributing to advancements in various industries.

2 MATERIALS AND METHODS

2.1 Introduction:

The methodology chapter presents the framework and procedures used to investigate the mechanical behaviour of granular materials and examine the effect of particle indexes on their response, as well as the combined effect of mechanical vibration and normal stress on the packing densification of wheat particles. This chapter outlines the experimental and numerical methods employed in the study and provides a comprehensive overview of the data collection, analysis, and interpretation processes. By detailing the testing procedures, particle index calculations, and the combined effect study, this chapter aims to ensure transparency and reproducibility in the research methodology.

The following sections will discuss the direct shear test, evaluation of particle indexes, analysis of mechanical behaviour, the combined effect of normal stress and mechanical vibration, analysis of the applied parameters, and statistical analysis. Each section will outline the specific techniques and approaches to address the research objectives and answer the research questions.

The direct shear test section focuses on the theoretical setup of the experiment, test procedure, and data collection during the shear testing of granular materials. It describes the boundary conditions and loading configuration applied to the test specimens and explains the measurements and observations recorded during the tests.

The section on evaluating particle indexes elaborates on their definitions and calculations, including the sphericity index SPH, Aspect Ratio AR, size index SI, and triple particle size index TPSI. This section presents the methodologies employed to quantify these indexes and highlights their significance in understanding the mechanical behaviour of granular materials.

The analysis of the mechanical behaviour section examines the relationship between particle indexes and various mechanical properties of granular materials. It investigates the influence of particle indexes on shear stress, particle rotation, volumetric strain, coordination number, shear zone thickness, etc. This section discusses the analytical approaches to assess these relationships and presents the corresponding results.

The combined effect of normal stress and mechanical vibration section describes the experimental setup and procedure for examining the packing densification of wheat particles under the influence of normal stress and mechanical vibration. It outlines the selection of normal stress levels and vibration amplitudes and the data collection and analysis techniques used to evaluate the combined effect.

The analysis of the applied parameters section investigates the intensity effect of the used parameters, explicitly focusing on the effects of vibration amplitude and normal stress. This

section discusses the methodologies employed to analyse and interpret the results obtained from the experimental and numerical investigations.

Lastly, the statistical analysis section covers the uncertainty analysis and sensitivity analysis conducted to evaluate the robustness and reliability of the research findings. It explains the specific statistical techniques employed, such as the Grubbs test and the Morris method, to assess uncertainties and quantify the sensitivity of the model output to input parameters.

In summary, this chapter provides a detailed account of the methodology employed in the research, encompassing experimental testing, numerical analysis, particle index evaluation, combined effect study, analysis of applied parameters, and statistical analysis. By following this methodology, the study aims to contribute to understanding granular material behaviour and provide valuable insights for practical applications and future research endeavours.

2.2 Discrete Element Method

2.2.1 Software and Applications

The commercial software EDEM® is commonly used for DEM simulations, employing the "Hertz Mindlin No-Slip" contact model (*DEM Solution. EDEM 2.7.0 User Guide. Edinburgh*). It facilitates particle motion analysis in various scenarios, including examining vibration effects and flow patterns in silos. The software considers particles' shape and micro-mechanical properties to represent their behaviour accurately.

Therefore, software like EDEM® has been used and utilised by employing the DEM approach, setting the model, and specifying appropriate simulation parameters. The mechanical behaviour of granular materials can be effectively analysed, providing valuable insights for various applications and processes. The calculation is done by a loop that iteratively applies Newtonian equations of motion to compute particles' acceleration, velocity, and displacement. The contact forces and torques between particles and walls and among particles are determined based on their interactions and recent displacements. This comprehensive approach enables the accurate description of bulk material flow and the behaviour of particles over time.

2.2.2 Time-Step and Shear Velocity Selection

Choosing time step and shear velocity in our DEM simulations ensures numerical accuracy and stability. Here, we provide details on the time step selection process and the rationale behind the shear velocity chosen for our simulations.

Time Step Selection

The time step in DEM simulations plays a crucial role in capturing the dynamic behaviour of particulate systems while maintaining numerical stability. To determine an appropriate time step, we calculated the Rayleigh time step (T Rayleigh), as present in Equation 3.1, which represents the theoretical maximum time step for a quasi-static particulate collection.

$$T_{Rayleigh} = \frac{\pi R \sqrt{\frac{\rho}{G}}}{0.1631\,\upsilon + 0.8766} \qquad 2.1)$$

R represents the average particle radius, ρ denotes the particle density, G represents the particle shear stiffness, and υ is Poisson's ratio. A time step below the Rayleigh time is generally preferred to minimise errors (Yan et al., 2015; Keppler et al., 2016; Garneoui, 2020).

For our simulations, we utilised 20% of the Rayleigh time step (0.2 T_R) as the time step, which is suitable for systems with a coordination number above 4. resulting in the use of a time step of 4.5×10^{-6} s, ensuring accuracy and stability throughout the simulations.

Shear Velocity selection

The shear velocity parameter determines the rate at which the lower container moves during the shearing process. This parameter is critical for capturing the particles' essential behaviours while ensuring numerical stability.

In our simulations, the shear velocity was set to 12 mm/s, which was chosen to expedite the analysis while still accurately representing the particles' behaviour. This velocity was carefully selected to maintain numerical stability, as evidenced by the consistent behaviour of the particle system throughout the simulations. Specifically, no excessive deformation or instability was observed in the model, and the total number of particles remained constant from the beginning to the end of the simulations, indicating the stability of the simulation model under this shear velocity condition.

2.2.3 Contact Model

The contact model plays a crucial role in DEM simulations as it governs the interactions between individual particles. In our study, we utilised the Hertz Mindlin (no slip) contact model due to its accuracy and efficiency in force calculation. This contact model is the default choice in EDEM software and provides reliable results for various applications.

The Hertz-Mindlin contact model incorporates normal and tangential forces based on well-established principles. The normal force component is derived from Hertzian contact theory, as proposed by (Hertz, 1881). Meanwhile, the tangential force model is based on (Mindlin, 1949; Mindlin and Deresiewicz, 1953) work, with damping components incorporated to account for energy dissipation during collisions.

Additionally, the contact model considers factors such as the coefficient of restitution, which influences the damping coefficient in both normal and tangential forces. The tangential friction force follows the Coulomb law of friction model proposed by (Cundall and Strack, 1979) while rolling friction is implemented using a contact-independent directional constant torque model.

During collisions, particle deformation is modelled as overlap, where the contact models determine the magnitude of forces based on the amount of overlap between particles. These models consider material and interaction properties defined by the user, including shear modulus and friction coefficients. Figure 3.1 represents this process.

While the contact models are primarily developed for spherical contacts, they can be adapted to model elastic or plastic collisions for cohesive and non-cohesive materials, providing a versatile framework for studying granular materials.

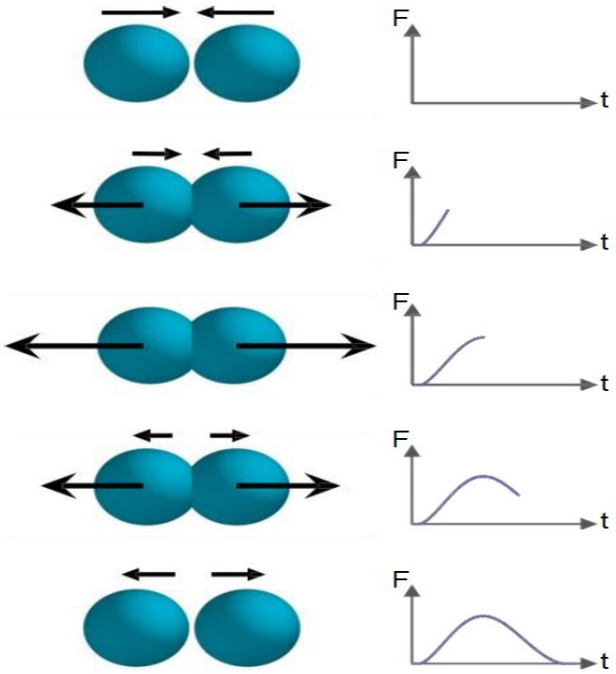

Figure 2.1. Hertz-Mindlin (no slip) contact model. A typical dependence of normal force on the normal overlap is depicted with an example of two colliding spheres. (DEM Solution. EDEM 2.7.0 User Guide.)

2.3 Simple Shear Test Modell

The direct shear test was conducted using an EDEM® numerical simulation approach. This section provides an overview of the direct shear test procedure used in the numerical experiments to investigate the mechanical behaviour of granular materials under different loading conditions. It involves simulating the response of granular material under controlled shear displacement or shear stress using the EDEM® software.

2.3.1 Test Setup and Particle Bed Preparation

The test setup and particle bed preparation process are critical aspects of conducting accurate numerical simulations to investigate the mechanical behaviour of granular materials using the EDEM® software. Therefore, several model settings and parameter selections have been considered, as mentioned in the upcoming sections.

2.3.1.1 Model Setup

Our study chose the simple shear test (SST) as the primary method to investigate the relationship between particle size and shape and particle assemblies' macro and micro behaviour. This choice was made due to the simplicity and effectiveness of the SST in capturing critical aspects of particle interactions under shear-loading conditions. However, while the SST provides valuable insights into the behaviour of granular materials, addressing the recommendation to explore particle indexes' impact on the particle set's failure curve is essential.

Our research primarily focuses on understanding the micromechanical properties of particles rather than studying the relationship between micromechanical and macromechanical properties. Therefore, the exploration of failure curves, typically used to analyse macro mechanical properties, is not within the scope of our study. Instead, we aim to investigate micromechanical properties such as particle rotation, contact number, volumetric strain, and shear strength under the influence of particle geometry parameters such as sphericity index (SPH), size index (SI), and triple particle

size index (TPSI) under validation of the numerical analysis of the failure curve. Therefore, a numerical model of the SST has been used in this study, as shown in Figure 3.2.

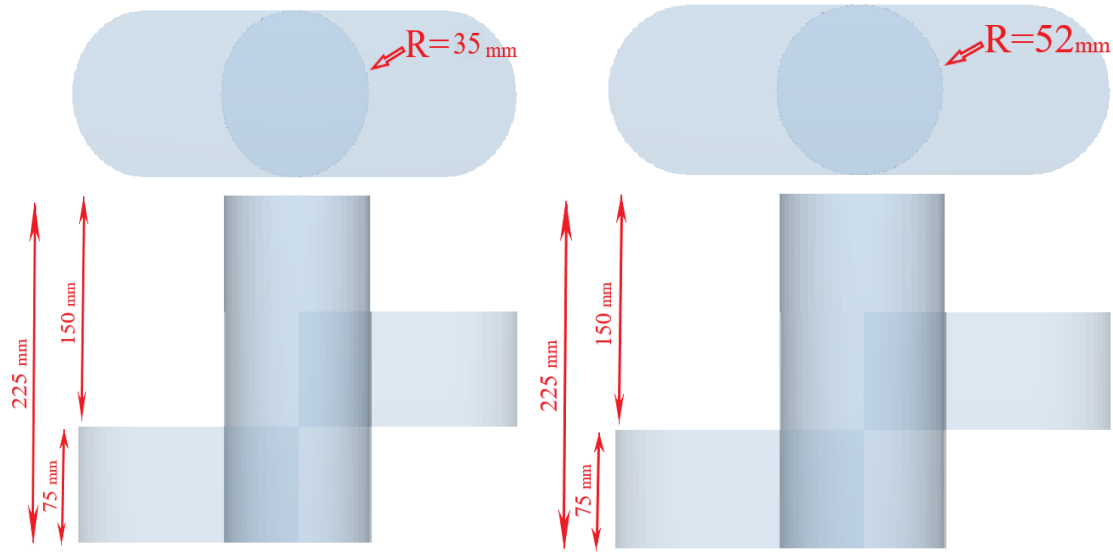

Figure 2.2. Schematic of Shear cylinders geometry

- In the simulations, a cylindrical domain was employed, characterised by a height of 225 mm and varying radii of 35 mm and 52 mm.
- The cylindrical domain was divided into a lower part (75 mm in height) and an upper part (150 mm in height).
- The lower part was set to move horizontally, while the upper part remained fixed in all directions.
- Normal stresses were applied to the particle bed using a large sphere with controlled variable densities, allowing various normal stresses to be applied to the bed.

2.3.1.2 Selection of Loading Tool

The choice of loading tool in shear tests is a critical aspect of the experimental setup, as it directly impacts the behaviour of the particulate system under shear. Our study considered carefully selecting the appropriate loading tool to mitigate potential issues such as the locking volume problem.

Mitigation of Locking Volume Problem

In our case, the large ball's spherical shape of the loading tool played a crucial role in mitigating the locking volume problem during shear tests. Unlike a flat compression plate, which could restrict the expansion of particles and lead to locking between the shear cell and the dead weight, the spherical shape of the loading tool provided greater freedom of movement.

During the initial settling phase, the large ball applied the normal load to the particles and settled on the top of the particle pile. At the subsequent shearing stage, as the particles began to rotate in the shearing zone, the total volume occupied by the particles in the container increased. This expansion pushed the large ball upward, allowing the particles to redistribute and accommodate the changing volume.

In contrast, using a flat plate to apply the normal load would have limited the total volume occupied by the particles, leading to a constant volume throughout the shearing process. That would have increased the normal load applied to the particles, contradicting the test procedure for studying shear stress under a continuous, steady, normal load condition.

Advantages of Using a Large Ball

Using a large ball to apply the normal load offered several advantages in our experimental setup. To begin with, it ensured a steady normal load during the shearing process, maintaining consistency in experimental conditions. Additionally, tracking the movement of the large ball allowed us to study volumetric strain, which represents the change in the total volume occupied by the particles in the container. That provided valuable insight into the behaviour of the particulate system under shear.

2.3.1.3 Model specifications

Previous researchers have validated the micromechanical parameters used for modelling through model dryer experiments and silo outflow tests, which are more dynamic than the simple shear test (SST) used in our study. Despite the differences in testing methodologies, our numerical model still yields stable and reliable results. The relationships between particle geometry and resulting micromechanical properties are well-established within the context of our numerical simulations. We plan to analyse failure curves to broaden our findings further and ensure the generalizability of our numerical model results. This additional analysis will enable us to examine the impact of particle geometry on shear strength and compare compressional stress ranges to the modelled shear stress. By conducting these additional analyses, we aim to comprehensively understand particle behaviour under various loading conditions and validate the relationships found in our numerical simulations.

The cylindrical domain was partitioned into two distinct sections: a lower segment measuring 75 mm in height and an upper segment spanning 150 mm in height. The decision to allocate considerable height to both containers was intentional and stemmed from the nature of our simulation model. In our model, the normal load is exerted on particles via a big spherical particle, propagating the applied normal load in an arc shape through the particle beneath. Therefore, the most significant impact of the normal load is at the centre of the cylindrical container, with a reduction in the normal load as moving away from the central axis. Our model was designed with relatively elevated heights to ensure a more uniform distribution of the applied load across the particles, eliminating this problem. The increased height of the upper container serves to counteract the curvature of the loading wave, facilitating a more uniform application of load as it propagates away from the source—the large spherical particle. The purpose of the heightened lower containers is to afford the particles greater freedom of movement. A diminished height for the lower container would close its bottom to the shear zone, potentially impeding particle movement during shearing and increasing the risk of mechanical particle interlocking. Additionally, the cylinder domain with a radius of 35 mm was utilised in simulations employing SPH and SI due to their relatively small size.

Conversely, for the TPSI simulations, a cylinder domain with a radius of 52 mm was used, ensuring adherence to a minimal recommended shear cell dimension, ideally seven times larger than the particle size. Given that the most extended TPSI particle utilised was 8 mm, the smaller radius container could accommodate a maximum of nine such particles, thus reaching its capacity limit. Consequently, adopting the second model with a radius of 52 mm was deemed imperative to mitigate the heightened risk of mechanical particle interlocking.

2.3.1.4 Bed Preparation

- A defined number of particles with similar shapes and sizes were generated for each simulation case.

- The particles were packed into the cylindrical container under the influence of gravity and allowed to settle until the bed reached a state of repose.
- This initial state of the particle bed was considered for all the simulation cases.

2.3.1.5 Simulation Stages

- The simulation scenarios were executed in four stages to represent particle behaviour accurately.
- Stage 1: Rapid particle generation - Particles were rapidly introduced into the cylinder, resulting in an elevated level of particle contact due to the dominant kinetic energy, as shown in Figure 3.3a.
- Stage 2: Settling time - The generated particles require settling time to reach a state of null kinetic energy, as shown in Figure 3.3b.
- Stage 3: Vertical and horizontal loading - The material bed was subjected to a vertical load by allowing a ball with a diameter similar to the cylinder diameter to fall onto the particle bed, as shown in Figure 3.3c. The adjustable density of the ball enabled the application of various vertical loads. The spherical shape of the loading tool (ball) helped mitigate the locking volume problem during shear tests.
- Stage 4: A direct shear test was performed by displacing the lower cylinder horizontally while maintaining the vertical load constant. Figure 3.3d illustrates the last simulation stage of the test.

After generating the particle bed and ensuring the particles are settled to reach zero kinetic energy, the next stage involves applying the normal load to the bed using the loading ball. The settling time for the big ball was empirically determined to be 1 s, allowing sufficient time to settle down and reach zero kinetic energy before the shearing stage begins.

A simulation timeline has been included to understand the simulation process comprehensively (see Figure 3.4). This timeline illustrates the different stages of the simulation, starting with particle generation and settling, followed by the large practical application of the normal load. The shearing stage commences after the settling time of one second, during which the big ball reaches zero kinetic energy.

Including the simulation timeline, the figure enhances the clarity and transparency of the simulation process, facilitating a better understanding of the experimental setup and methodology employed in our study.

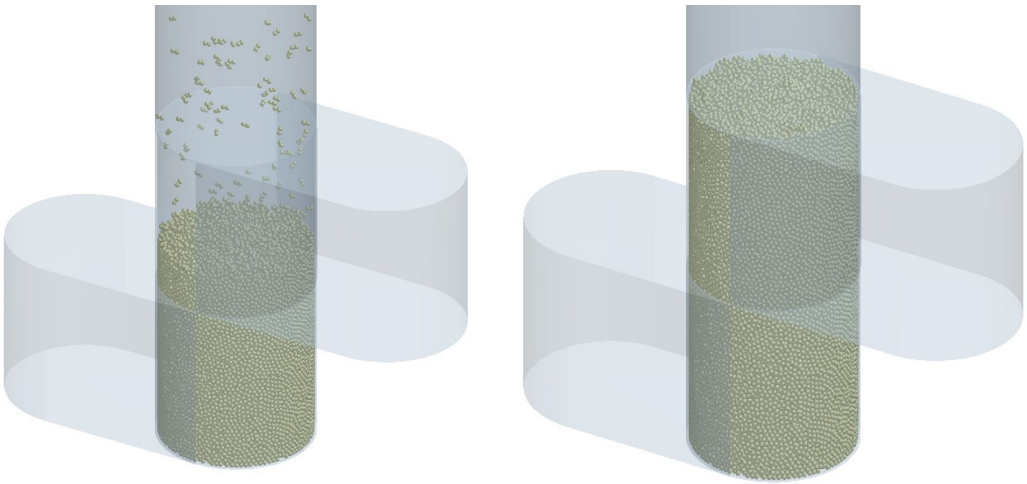

(a) (b)

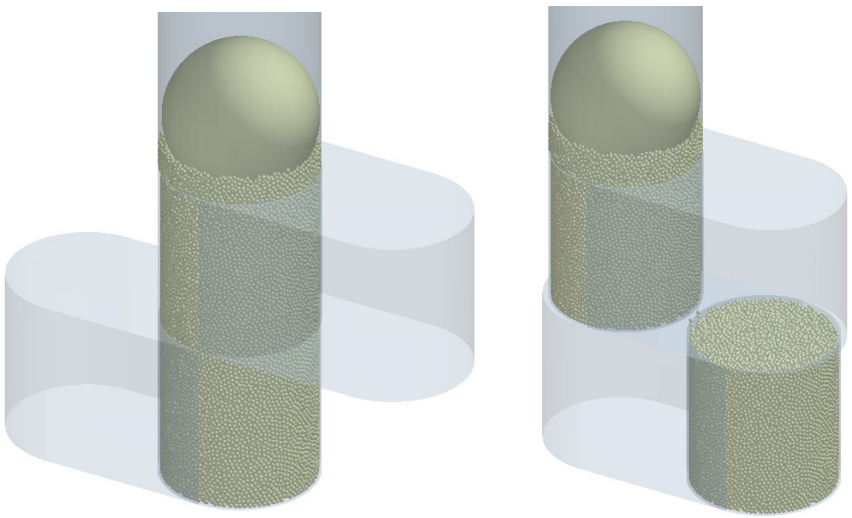

(c) (d)

Figure 2.3. Shear box Simulation and assembly generation Stages (Stages a to d)

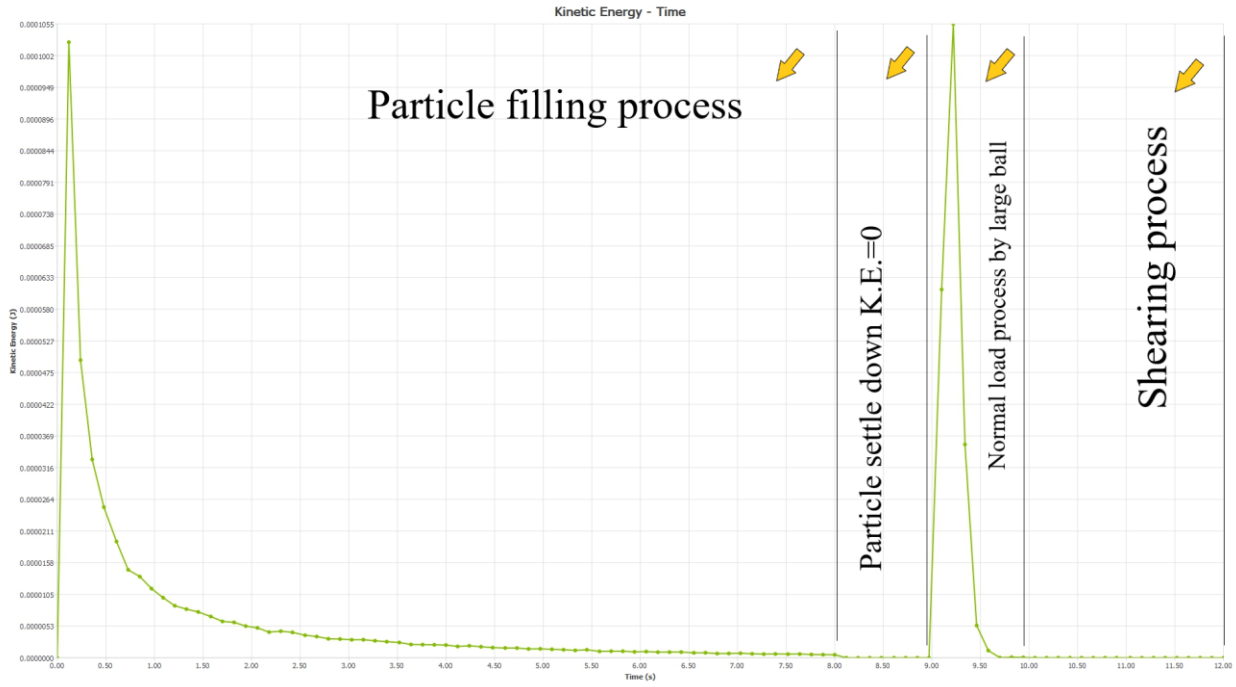

Figure 2.4. The kinetic energy of the system during the simulations

2.3.2 Micromechanical model parameters

Table 3.1 shows the micromechanical parameters of the DEM model used in simulation tests. Previous work (Keppler et al., 2012a; Oldal and Safranyik, 2015; Garneoui, 2020) has been used to achieve accurate results.

Table 2.1. micromechanical parameters of the DEM model (Keppler et al., 2012b; Oldal and Safranyik, 2015; Garneoui, 2020)

Name	N	G (MPa)	ρ (kg/m3)	C_{rp}	C_{rw}	μ_{0p}	μ_{rp}
Particles	0.4	$3.58*10^8$	1430	0.5	0.6	0.3	0.01
Wall	0.3	$8*10^8$	7500	0.6	-	0	0

1. Poisson's ratio ν: defined as the ratio of transverse contraction strain to longitudinal extension strain in the direction of the stretching force.
2. Shear modulus G: defined as the ratio of shear stress F to the shear strain A, G = F/A, where shear stress is the components of stress at a point that act parallel to the plane in which they lie, and shear strain is the components of a strain at a point that produce changes in the shape of a body (distortion) without a volumetric change.
3. Density ρ: defined as the weight per unit volume.
4. Coefficient of restitution C_r represents the ratio of separation speed to the speed of approach in a collision.
5. Coefficient of static friction μ_0.
6. Coefficient of rolling friction μ_r.

2.4 Modelling of Particle Indexes

This section evaluates various particle indexes to characterise the particles' shape properties on the macro and micromechanical behaviour of the direct shear tests. These indexes provide quantitative measures that help understand particle behaviour and its suitability for specific applications. The following subsections describe the definition and calculation methods for three particle indexes:

The Sphericity Index (SPH) and the Aspect Ratio (AR) quantify the roundness or elongation of particles. The Size Index (SI) represents the particle size, and the Triple Particle Size Index (TPSI) captures the variation in size for specific particle assemblies.

2.4.1 Modelling of Sphericity Index SPH and Aspect Ratio AR

The Sphericity Index (SPH) is a fundamental metric employed to assess the roundness of particles, signifying the degree to which a particle's shape resembles a complete sphere. Traditionally evaluated based on specific shape characteristics, particularly the ratio of a particle's volume to the volume of the smallest circumscribing sphere, SPH plays a crucial role in understanding granular materials' packing and flow behaviour (Danesh et al., 2020). In our study, we extended this concept by using another approach, as depicted in Figures 3.5 and 3.6, building upon the foundation laid by previous researchers.

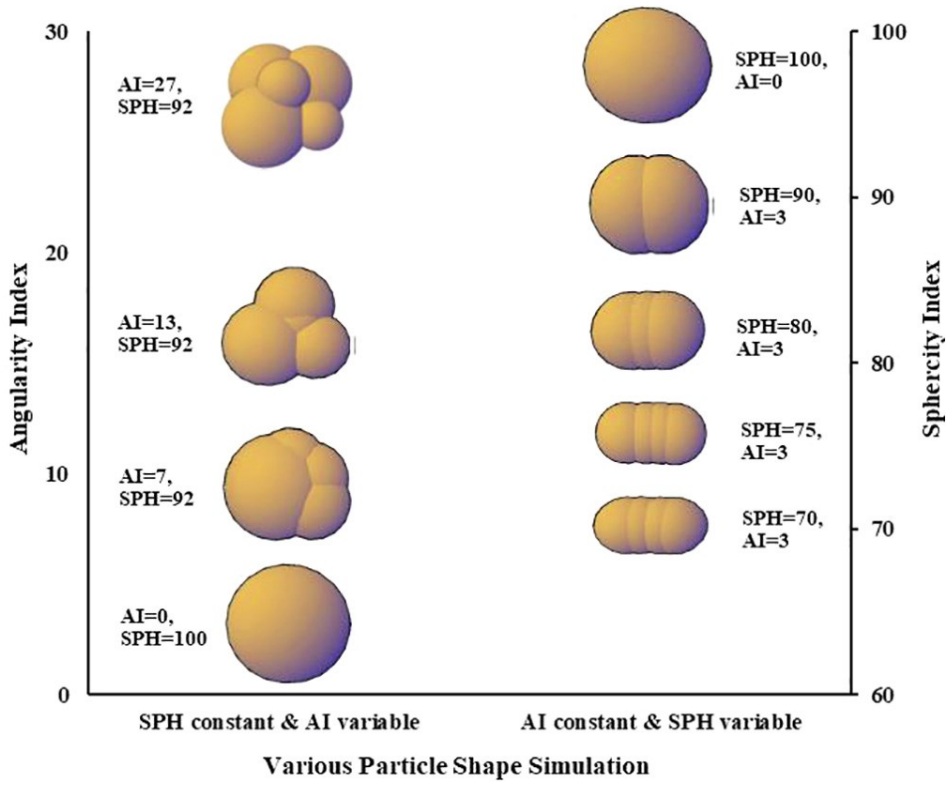

Figure 2.5. Sphericity Index Variations, according to (Danesh et al., 2020).

In Figure 3.5, the sphericity index, as (Danesh et al., 2020) studied, is presented for different particle numbers, providing a benchmark for comparison. A clump of double particles was employed to achieve a more uniform representation, systematically varying the particle sphericity by increasing the distance between the centres of the double particle clump, as shown in Figure 3.7.

In addition to SPH, the particle elongation can be quantified using another particle index called the Aspect Ratio (AR). The Aspect Ratio is defined as the ratio of b/a, as illustrated in Figure 3.6, where b is the length of the minor axis, and a is the length of the central axis of the particle (Yang et al., 2012; Xie et al., 2017).

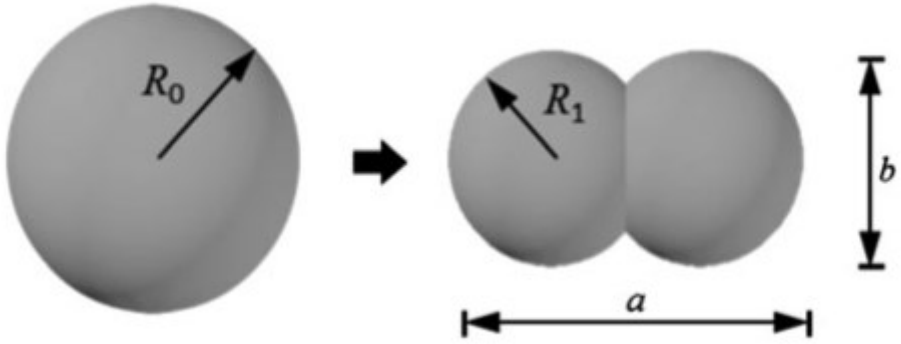

Figure 2.6. Particle Aspect Ratio (Xie et al., 2017)

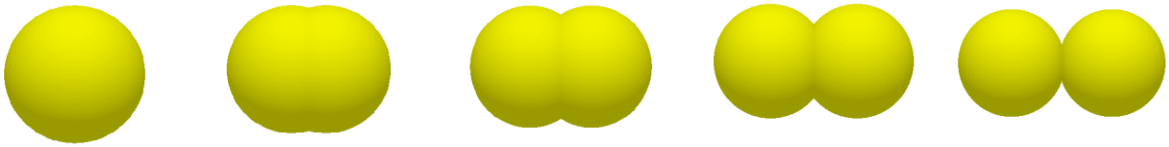

Figure 2.7. Studied Sphericity SPH and aspect ratio AR

The simulations encompassed five distinct particles, each characterised by varying AR, as demonstrated in Figure 3.7. Our modified sphericity index values for the selected particles were 100%, 98%, 94%, 88%, and 81%, corresponding to AR values of 1, 0.8, 0.667, 0.571, and 0.513, respectively. They maintained uniform particle size across all simulations (with a radius of 1mm) and minimised gradation effects. The distance between double particle centres was set as 0mm, 0.5mm, 1mm, 1.5mm, and 1.9mm for each simulation repetition, as illustrated in Table 3.2.

Table 2.2. assemblies with varying SPH

SPH Value (%)	Particle Aspect Ratio AR	Number of Particles	The length of the central axis a (mm)	The length of the minor axis b (Diameter)(mm)
100	1	80000	2	2
98	0.8	62000	2.5	2
94	0.67	51500	3	2
88	0.57	43000	3.5	2
81	0.51	40000	3.9	2

The simulated direct shear tests were conducted under various vertical stresses. The particle model incorporated different particle indexes, with the SPH and AR indexes providing a quantitative analysis of the particle shapes. The AR values ranged between one, representing a complete sphere, and 0.51, representing an elongated particle encompassing various practical shapes. Each AR configuration was subjected to four different vertical loads (1900, 4150, 5500 and 7800 Pa), resulting in twenty simulations due to the five different AR configurations.

This innovative approach broadens the scope of understanding particle shape dynamics and contributes to knowledge in granular material mechanics.

2.4.2 Modelling of Size Index SI

The Size Index (SI) is a crucial parameter for assessing the particle size distribution within granular materials. It is determined by measuring the diameter or radius of individual particles. This study's SI values of 50%, 75%, 100%, 125%, and 150% were defined to investigate the influence of different particle sizes on mechanical behaviour (Talafha et al., 2022).

Figure 3.8 depicts the defined SI for a five-particle configuration used in the simulations (Size Indexes = 150%, 125%, 100%, 75%, and 50%, respectively).

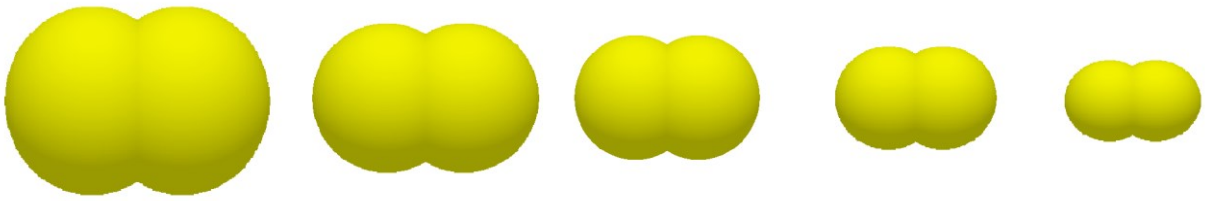

Figure 2.8. Studied Size index SI

The particle size remained constant throughout all simulations to minimise any degradation effects. However, the particle radius and distance between the centres of particles varied for each simulation repetition: R= 1.5mm, 1.25mm, 1mm, 0.75mm, and 0.5mm. For each simulation scenario, particles of specific shapes and sizes were generated. The assemblies with SI=50% consisted of 596,000 particles, SI=75% assemblies had 280,000 particles, SI=100% assemblies had 110,000 particles, SI=125% assemblies had 60,000 particles, and SI=150% assemblies had 32,000 particles. The identical SI particles compacted by normal gravity forces fill the shear cylinder to ensure a meaningful comparison, and this process was repeated for each simulation, as shown in Table 3.3.

Table 2.3. assemblies with varying SI

SI Value (%)	Number of Particles	Distance between Double Particle Centres (mm)	Particle Size (Radius) (mm)
50	596000	0.5	0.5
75	280000	0.75	0.75
100	110000	1	1
125	60000	1.25	1.25
150	32000	1.5	1.5

Moreover, to maintain the same particle shape, the ratio distance between the centres of the clumps (sphericity index=88%) was kept constant. Each SI was subjected to four different vertical loads, leading to twenty simulations due to five different SI configurations.

2.4.3 Modelling of Triple Particle Size Index TPSI

The Triple Particle Size Index (TPSI) is introduced to analyse the variation in particle size within specific assemblies. It considers the size distribution by incorporating three different particle sizes. By characterising the triple size variations, we can investigate the impact of particle size heterogeneity on the behaviour of granular materials (Talafha and Oldal, 2022).

Figure 3.9 depicts the defined TPSI for a three-particle configuration used in the simulations (Triple particle Size Indexes = 100%, 125%, and 150%, respectively).

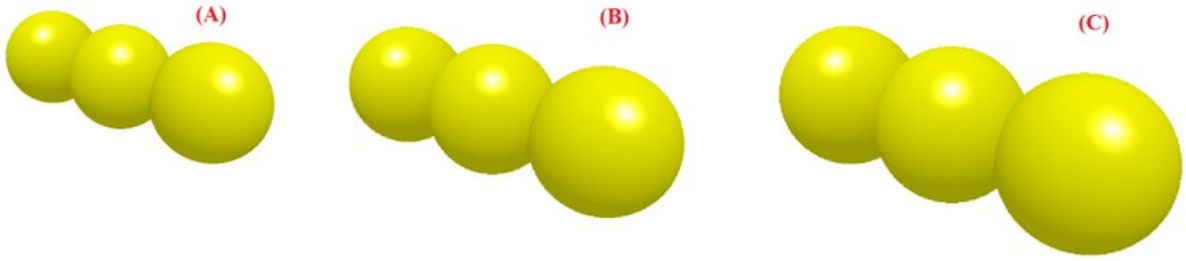

Figure 2.9. Studied triple particle size index TPSI

Various assembly series were performed for the different triple particle size index values under two different vertical stresses (4 kPa and 8 kPa) to examine the effects of normal load and Size Index on the mechanical properties of the model. Each repetition involved generating particles with the same shape and size, resulting in assemblies with specific particle distributions. The SI = 100% assembly contained 55,000 particles, the SI = 125% assembly had 28,000 particles, and the SI = 150% assembly contained 16,000 particles. The normal gravity forces were applied to compact the particles within the shear cylinder, enabling successful sample comparisons, as shown in Table 3.4.

Table 2.4. assemblies with varying TPSI

TSI Value (%)	Number of Particles	Distance between Particle Centres (mm)	Particle Size (Radius) (mm)
100	55000	1.7	1
125	28000	2.125	1.25
150	16000	2.55	1.5

2.4.4 Summary

By considering various particle indexes, including the Sphericity Index (SPH), Aspect Ratio (AR), Size Index (SI), and Triple Particle Size Index (TPSI), along with the defined simulation parameters and settings, we can conduct a comprehensive analysis of the granular material's mechanical behaviour and its dependence on different particle characteristics.

2.5 Combined Effect of Normal Stress and Mechanical Vibration

In this section, we investigate the combined effect of normal stress and mechanical vibration on the behaviour of granular materials, with a specific focus on wheat particles. The experimental design comprises two distinct segments to assess the impact of the studied parameters on wheat packing density and develop a new exponential model to predict the effect of normal stress and vibration amplitude.

2.5.1 Experimental Setup for Combined Effect Study

The experimental setup for investigating the combined effect of normal stress and mechanical vibration was meticulously designed to provide insights into particle packing density under dynamic loading conditions. It involved a commercial vibration table reminiscent of a 3D vibrator

used in prior research on the densification of various granular materials such as spheres, cube-sphere combinations, and mono-sized cylinders (Milewski, 1973; Yu et al., 1993; Zhang et al., 2006; Gámez et al., 2013). This vibration table, presented in Figure 3.10, featured a PMMA container with a 36mm inner diameter filled with 115g of wheat particles. An accelerometer was affixed to the vibration table to accurately measure the frequency and amplitude of the applied vibration. The experiments were organised into four groups, each subjected to various levels of normal stress (free load, 13.3kPa, 22.9kPa, and 42.3kPa) and five different vibration amplitudes, ranging from 0 to 6.7mm. Each test was repeated three times to ensure reliable data collection, yielding approximately eighteen readings for each group, as depicted in Figure 3.11. Careful consideration was given to standardising these factors to address potential variations in initial packing density due to pouring parameters such as drop height, concentricity, and opening orifice. Specifically, the drop height, concentricity, and opening orifice were fixed for the entire experiment to minimise variability in initial packing density.

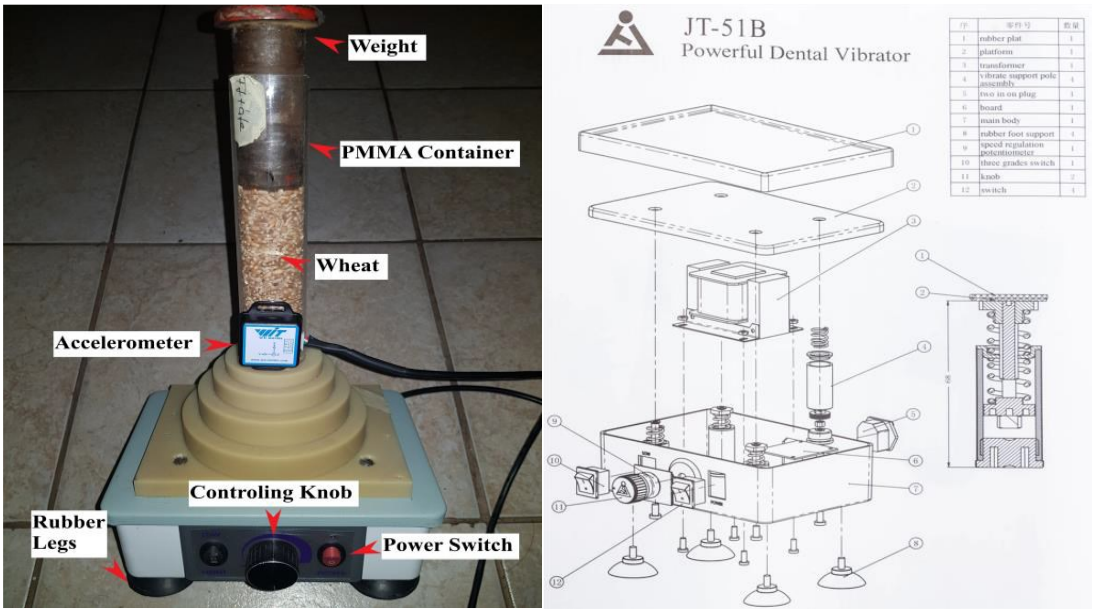

Figure 2.10. (a) the schematic graph of the vibration device. (b) the experimental device after mounting the PMMA container, weights, accelerometer and filled wheat particles.

Test Configurations	Normal Stress kPa	Vibration Amplitude (mm)	Number of Readings
Free Load	-	0	3
	-	2.8	3
	-	3.55	3
	-	5.6	3
	-	6.6	3
13.3 kPa	-	-1	3
	13.3	0	3
	13.3	1.3	3
	13.3	2.30	3
	13.3	4.70	3
	13.3	6.70	3
22.9 kPa	-	-1	3
	22.9	0	3
	22.9	1	3
	22.9	1.20	3
	22.9	2.90	3
	22.9	4.80	3
42.3 kPa	-	-1	3
	42.3	0	3
	42.3	0.7	3
	42.3	0.8	3
	42.3	1.35	3
	42.3	3.4	3
The Sum of the Readings			69

Figure 2.11. Model test configurations

Before applying vibration and normal stress, the initial height of wheat particles in the container was measured to determine the initial wheat packing density. The vibrator utilised in the study allowed precise control of vertical (Z direction) vibrations with a constant frequency of 50 Hz, achieved through a steady RPM. Analysis of the vibration data revealed that vertical amplitude exhibited a predominant influence compared to vibrations recorded in the horizontal (X and Y) directions. Table 3.5 presents an example of low and high-vibration tests.

Table 2.5. The vibration amplitude in the three axes.

3D directions	**z-direction**	**y-direction**	**x-direction**
Low amplitude test	2.4 mm	0.65 mm	0.2 mm
High amplitude test	6.6 mm	0.65 mm	0.2 mm

Hence, this investigation focused on the vertical direction (z-axis) due to the negligible amplitude of vibrations in the horizontal directions (x and y).

The vibration displacement was mathematically defined by Equation 3.2:

$$S = A \sin\ (2\,\pi\,f\,t + \Phi) \qquad 2.2)$$

Where the displacement S [mm], the amplitude in the z-direction A [mm], the vibration frequency f [Hz], and the vibration time t [s], along with the primary phase (Φ), are critical parameters in the experimental process that directly influence the packing density of wheat. Further details regarding the vibrator can be found in Figure 3.10.

Before experimentation, the container was thoroughly cleaned with water and dried in an oven set at 60°C. Subsequently, the wheat particles were weighed using an electronic scale and carefully placed into the container to establish the initial packing structure and prevent segregation. The average height of the initial packing structure at various locations was measured, and equation 3.3 was employed to estimate the initial packing density (ρ).

$$\rho = V_P/V_C = \frac{m_P/\rho_P}{(\pi * D^2/4)^*\overline{H}} \qquad 2.3)$$

In this study context, the packing density ρ [-] is defined as the ratio of the volume of the particles. V_P [m^3] to the volume the particles occupy in the container V_C [-]. The mass of particles m_P [kg], while the density of particles ρ_P [kg/m^3] The mean height of the packing structure $\overline{H}$ [m]; moreover, the inner diameter of the container is represented as D [m].

The wheat particle density utilised in Equation 3.3 was determined experimentally using a specific procedure to account for variations in particle volume due to physical behaviours such as moisture content. Initially, a constant weight of 115g of wheat was used in the experiments. It was necessary to determine the volume they occupied in the container to calculate the density of the wheat particles. That was achieved by pouring enough water into the container to fill the gaps between the wheat particles, as illustrated in Figure 3.12. The mass of the poured water and the volume occupied in the container were measured. The volume occupied by the wheat particles alone was obtained by subtracting the water volume from the water-wheat mixture's total volume. The volume of water filling the gaps between the wheat particles was determined by dividing the mass of the water by its density. The wheat particle density was calculated by dividing the wheat mass by its volume, Using the mass and volume of the wheat particles. Mathematically, this process can be represented as follows:

Wheat Particle Density = (Mass of Wheat) / (Volume of Wheat)

Volume of Wheat = Total Volume - Volume of Water

Volume of Water = (Mass of Water) / (Density of Water)

Density of Wheat = (Mass of Wheat) / (Total Volume - (Mass of Water) / (Density of Water))

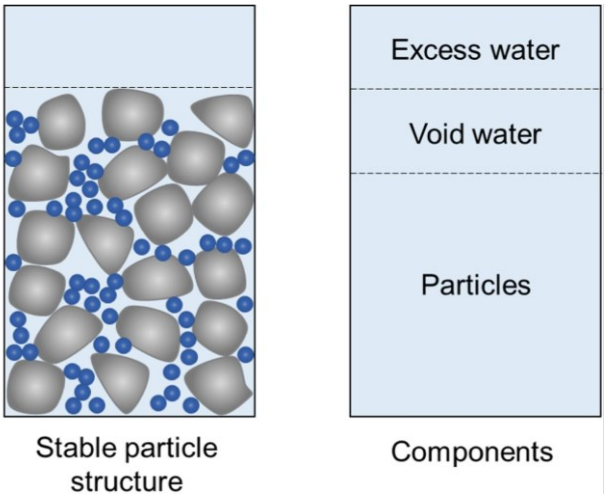

Figure 2.12. The total volume of the wheat and the water mixture (left-hand side) compared to the volume occupied by the wheat particles' structure (Fennis et al., 2013)

This method ensured that our wheat particles' density matched how they behaved in our experiments. We did this at the very end of all our tests to accurately determine the wheat particles'

density. Then, we calculated the wheat's packing density by measuring the wheat pile's height at the beginning and end of each test. Moisture content can affect how much space the particles occupy and how tightly they're packed. For instance, more moisture can cause the particles to swell, creating more gaps between them and reducing packing density. Conversely, less moisture can shrink the particles, causing them to fit together more tightly and increase packing density. Therefore, the moisture content has an insignificant effect on our results.

2.5.2 Test Procedure

The experimental procedure for the combined effect study entails two distinct protocols. Wheat is introduced into a container, and the initial grain height is meticulously measured to establish the initial packing density. Specific parameters are selected, including normal stress vibration amplitude (ranging from 0 to 6.7 mm). The experiment unfolds over a total period of 10s, divided into discrete 1s intervals. Throughout each second, the vibration table is activated for 1s and then deactivated, with the resulting packing density recorded meticulously. This process iterates every second until the completion of the 10s experimental period. Each run is replicated three times to ensure data reliability and mitigate potential human errors. Figure 3.13 illustrates the flowchart processes of the first experiment. During the test procedure, meticulous care was taken to replicate the initial packing density for each experiment. That involved remaking the procedure by refilling the container using the filling cone. Adherence to standardised pouring processes and consistent parameters, such as drop height and opening orifice, facilitated achieving the same initial packing density for all experiments. Using the filling cone was pivotal in eliminating potential variations in initial packing density, ensuring the reliability and reproducibility of the experimental results.

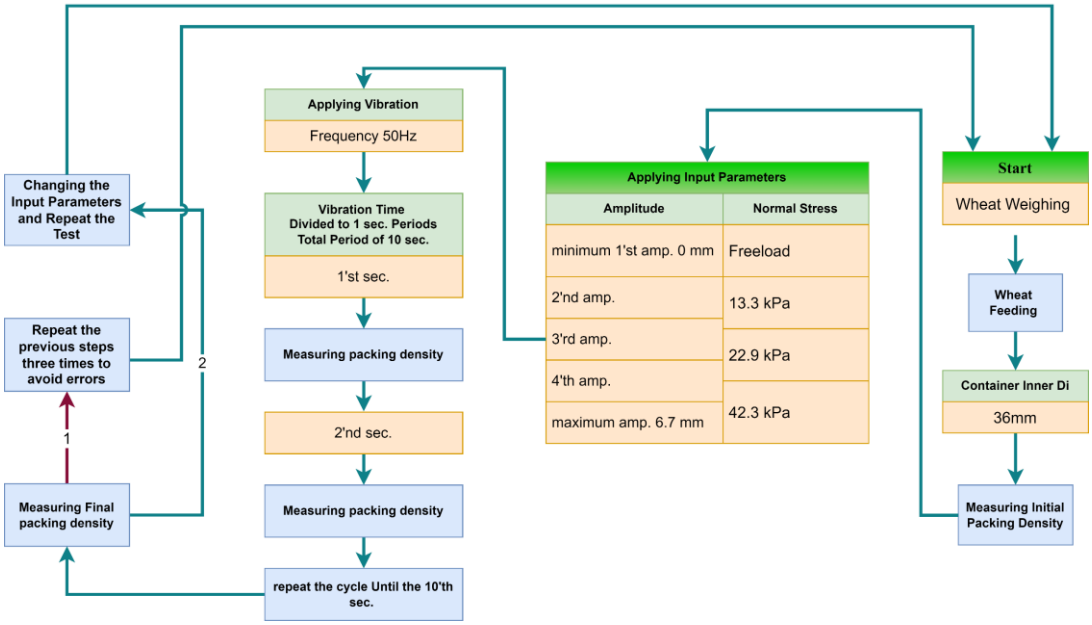

Figure 2.13.The flowchart processes of the first experiment.

The second experimental protocol mirrors the first, with a significant deviation in the testing approach. Following the initial measurement of the wheat's packing density, the vibration table operates continuously for 10s. Upon deactivating the vibration table, the final packing density is meticulously gauged. The fixed frequency ω is maintained at 50 Hz throughout these experiments, and the container's inner diameter (D) remains at 36 mm. Additionally, dead weights, including free weight, 1.375 kg, 2.380 kg, and 4.390 kg, are employed in the experiments. The variable parameters are the vibration amplitude A and the use of dead weights, which are systematically varied while keeping other conditions constant. This precise methodology, depicted in Figure 3.14, comprehensively evaluates each component's influence on wheat's packing density.

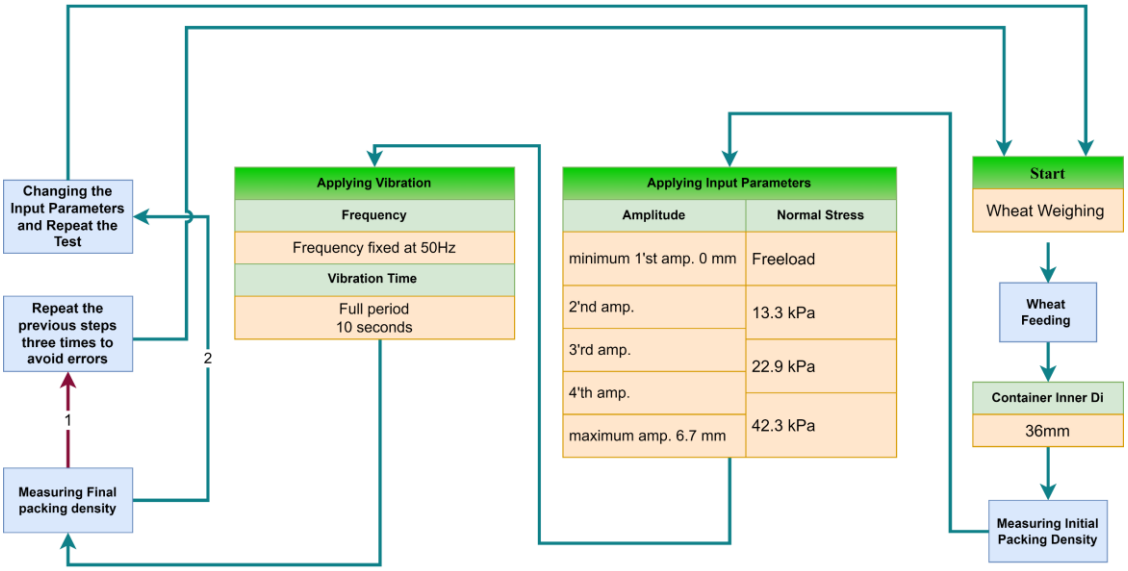

Figure 2.14.The flowchart processes of the second experiment.

2.5.3 Data Collection and Analysis

Data collection includes measuring the packing density of wheat particles during each second of the experiment to evaluate the impact of varying parameters on the final packing density. The obtained packing density values are analysed based on a predefined set of operating parameters, including vibration amplitude, frequency, and normal stress levels. Statistical methods and data visualisation techniques are employed to identify patterns and trends in the experimental results.

2.5.4 Analysis of the Applied Parameters

In the conducted experiments, the investigated parameters include the variable parameter A (vibration amplitude ranging from 0 to 6.7 mm), the fixed frequency ω (set at 50 Hz), the container with inner diameter D of 36 mm, and the use of dead weights (including free weight, 1.375 kg, 2.380 kg, and 4.390 kg), each parameter is varied individually to evaluate its influence on the packing density of wheat while keeping the other parameters constant. Figure 3.15 shows the dead weight used in the experiment.

Figure 2.15. The experiment deadweights

The experimental results are analysed to understand the interaction between normal stress and mechanical vibration on wheat packing density. The impact of each parameter and their combined

effect on the packing behaviour of wheat particles is assessed. The proposed exponential model is validated to predict the packing density under different loading conditions.

In conclusion, the "Combined Effect of Normal Stress and Mechanical Vibration" section presents the experimental setup, procedure, data collection, and analysis for investigating the interaction between normal stress and mechanical vibration on the packing density of wheat particles. The results and insights gained from this study contribute to a better understanding of granular material behaviour under realistic loading conditions. They can be applied to optimise various industries' material design and process parameters.

2.5.5 Statistical Analysis

Considering the presented information, uncertainty analysis plays a pivotal role in comprehending the accuracy and reliability of the data obtained in our wheat packing density study. Using various analytical techniques, such as the Grubbs test, we identified and eliminated outliers from the dataset, thus ensuring the utmost precision in our results. As depicted later in Figure 4.38, the uncertainty of wheat packing density is illustrated for different applications of normal stress with the applied amplitude, and the highlighted area within the fitted line represents the corrected standard deviation for the collected data.

It is noteworthy that sensitivity analysis is also paramount in assessing the influence of diverse parameters on the obtained outcomes. By conducting a comprehensive uncertainty and sensitivity analysis, we can establish the robustness and reliability of our findings, thereby providing valuable insights for future research and practical applications in this field.

2.5.5.1 Uncertainty Analysis

Uncertainty analysis evaluates the precision and reliability of our experimental measurements and data processing. This study uses the Grubbs test to detect and remove outliers from the collected dataset. We eliminate outliers and ensure the calculated packing density values accurately represent the experimental conditions.

The uncertainty analysis enhances the credibility of our findings, allowing us to make meaningful comparisons and draw reliable conclusions from the experimental data. It also provides valuable information for assessing the variability in the results and guiding future research efforts.

2.5.5.2 Sensitivity Analysis

Sensitivity analysis is a vital component of our investigation, which aims to understand the impact of varying input parameters on the packing density of wheat particles. In this study, we adopted the Morris method for sensitivity analysis, which involves systematically varying the model's input parameters within predefined ranges and observing the resulting output.

The Morris indices were calculated to quantify the sensitivity of the model output to each input parameter, and the parameters were ranked based on their relative importance.

3 RESULTS AND DISCUSSION

3.1 Introduction

In this Chapter, we explore the influence of shape indexes on granular materials, beginning with an in-depth analysis of the failure curve (4.2). We dissect the failure curve to understand how particle cohesion and internal friction angle vary concerning the shape indexes, particularly SPH and SI. Transitioning to examining shear stress patterns (4.3), we delve into the variations observed under different shape indexes, including SPH, AR, SI, and TPSI. Subsequently, we investigate the behaviour of volumetric strain (4.4) to discern how particle morphology impacts material volumetric strain, shedding light on the intricate interplay between shape indexes and volumetric behaviour. Moving forward, we explore average contact numbers (4.5) and contact force chain

dynamics (4.6), unravelling the complex relationships between particle shape and contact behaviour. Additionally, we scrutinise shear zones and particle rotations (4.7), elucidating the unique imprints left by shape indexes on shear behaviour. Finally, we unravel the combined effect of normal stress and mechanical vibration on wheat packing density (4.8), providing valuable insights for granular material engineering. While acknowledging the limitations of our study, we chart future research paths, aiming to advance our understanding of granular material behaviour and its practical implications.

3.2 Failure Curve Analysis

Failure curve analysis is pivotal to understanding the mechanical behaviour of granular materials under shear loading conditions. In this section, we delve into drawing and interpreting the failure curve, clarifying the calculation of cohesion and internal friction angle and analysing the influence of shape indexes, specifically the Sphericity Index (SPH) and Size Index (SI).

Analysing the Influence of Shape Indexes

We conducted three experiments for each index to investigate the influence of shape indexes, namely SPH and SI, resulting in four figures 4.1- 4.4 illustrating the relationship between shear stress and shear strain. The first two figures, 4.1 and 4.2, depict the response of SPH 81% and SI 100% samples to multi-normal stresses of 50, 75, and 100 kPa for SPH and 30, 45, and 60 kPa for SI. Subsequently, by averaging the data points from the three experiments at quasi-static state conditions, the following figures, 4.3 and 4.4, present the failure curves, showcasing the relationship between shear stress and normal stress for SPH 81% and SI 100% samples.

We can see that the quasi-static condition dominant after the assembly surpasses the peak shear stress and reaches the stable shear stress with the shear strain.

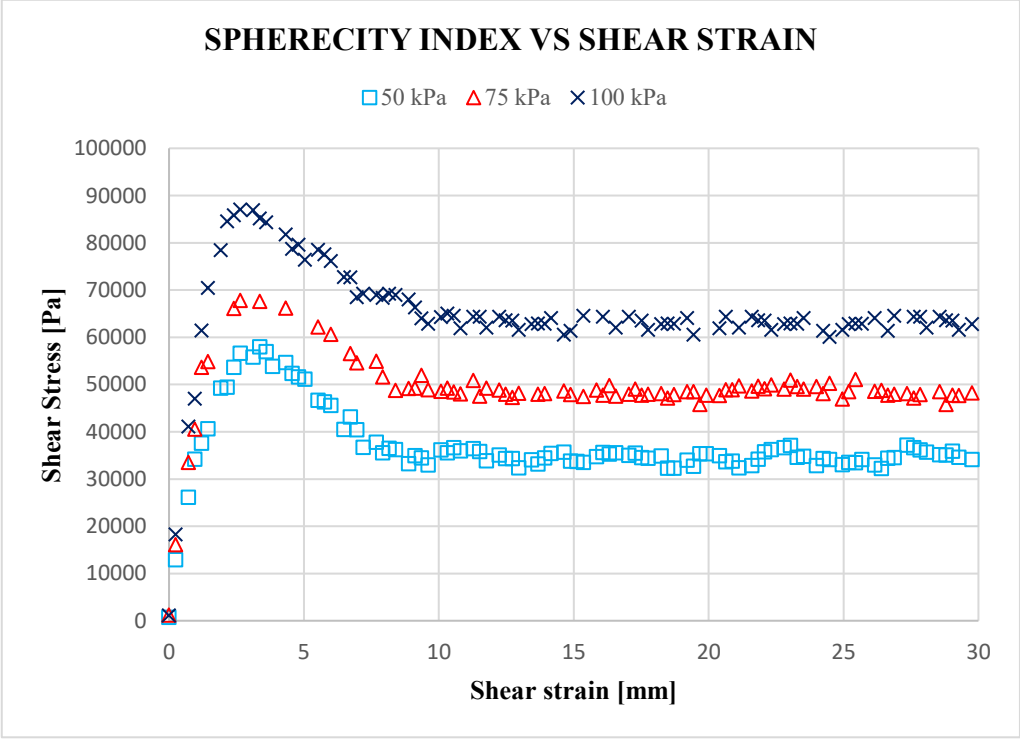

Figure 3.1. relationship between shear stress and shear strain for the SPH under multi-normal stress

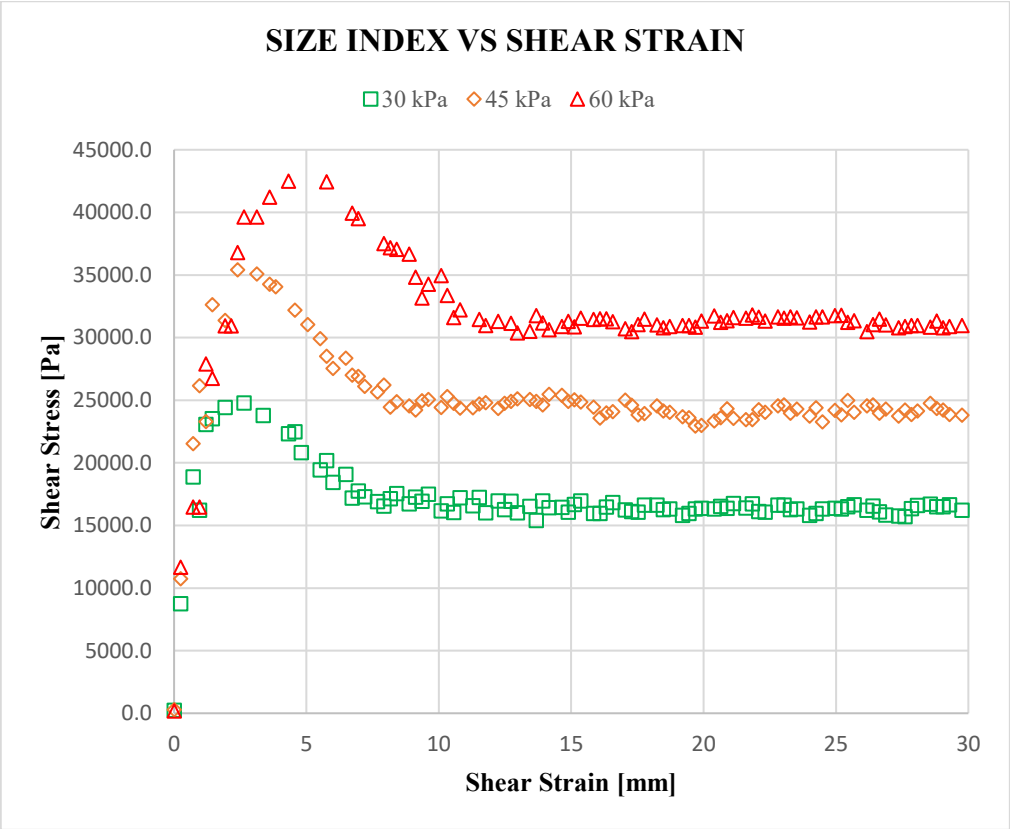

Figure 3.2. relationship between shear stress and shear strain for the SI under multi-normal stress

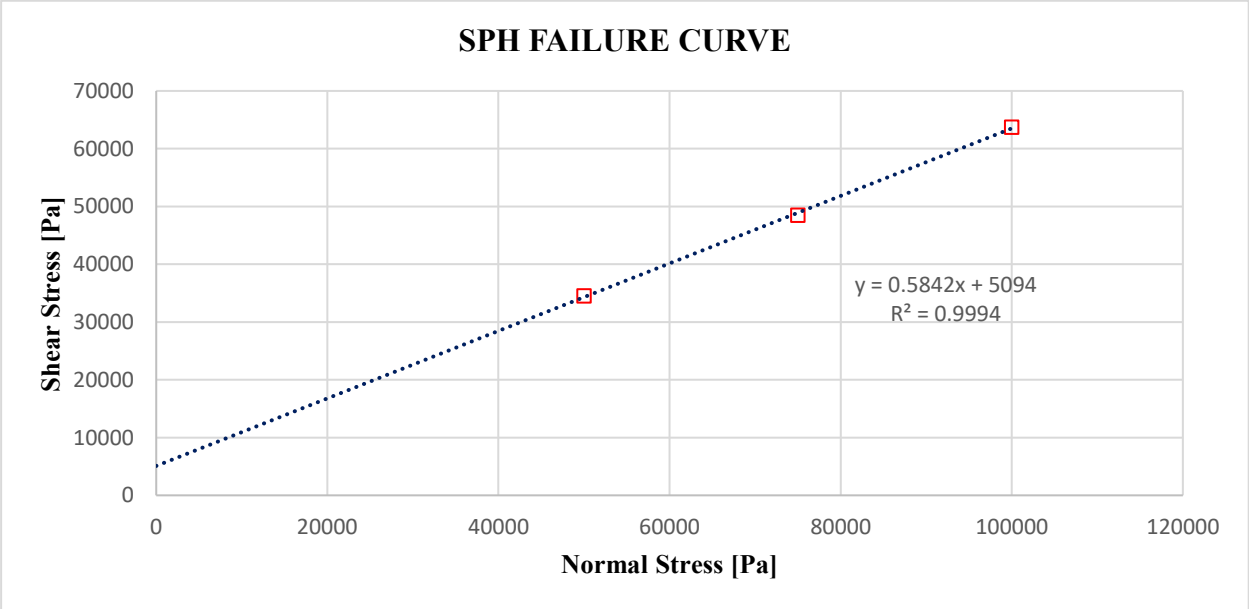

Figure 3.3. SPH failure curve

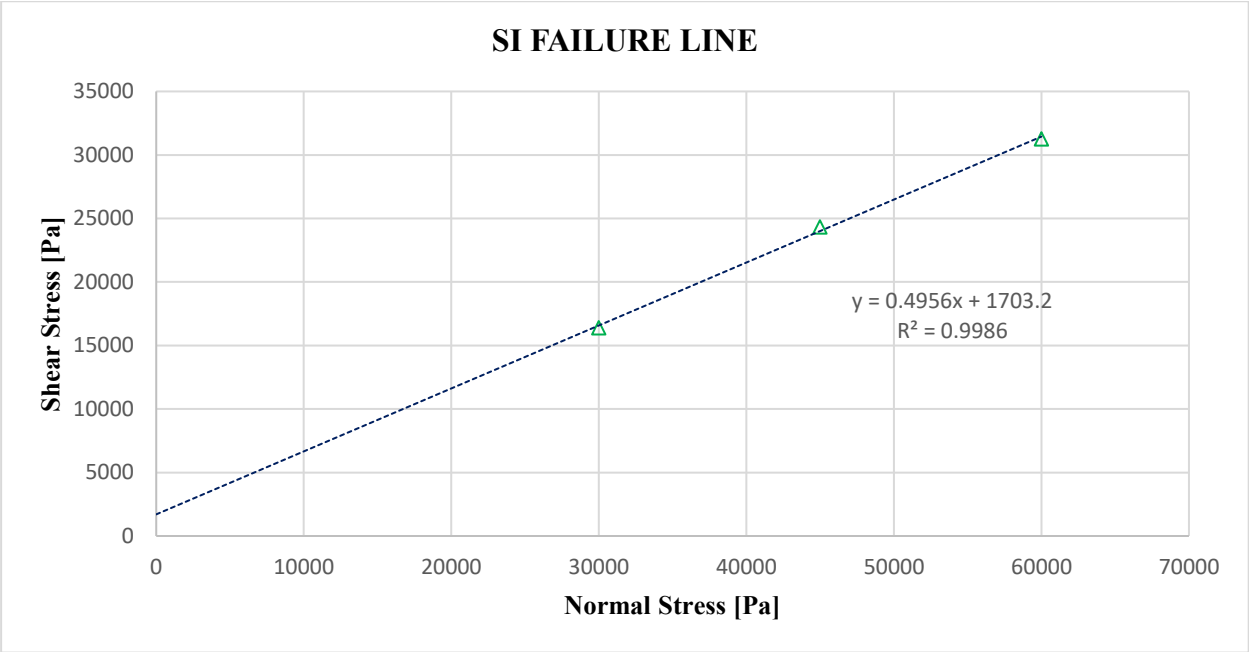

Figure 3.4. SI failure curve

Calculation of Cohesion and Internal Friction Angle

The failure curve analysis provides insights into granular materials' shear strength and flow behaviour, deriving two fundamental parameters: cohesion (c) and internal friction angle (φ). Cohesion (c) signifies the intercept of the failure curve with the shear stress axis (τ-axis) under zero normal stress (σ = 0). Mathematically, cohesion is expressed as:

$c = \lim_{(\sigma \to 0)} \tau$

The internal friction angle (φ) is determined by the slope of the failure curve in the Mohr-Coulomb representation and can be calculated using the formula:

$\phi = \tan^{-1}(\Delta\tau/\Delta\sigma)$

Here, Δτ represents the change in shear stress, and Δσ indicates the change in normal stress between two data points on the failure curve. From Figures 4.3 and 4.4, we compute the internal friction angle (φ) and cohesion (c) as follows:

For SPH:

ϕ = tan^(-1) * 0.5842

ϕ = 0.5287 rad

ϕ = 0.5287 * 180 / π

ϕ = 30.3°

Similarly, for SI:

ϕ = tan^(-1) * 0.4956

ϕ = 0.4601 rad

ϕ = 0.4601 * 180 / π

ϕ = 26.4°

Cohesion is directly obtained from Figures 4.3 and 4.4 by extracting the shear stress value at the intersection point between the failure curve and the y-axis:

For SPH:

(c) = 5094 Pa

For SI:

(c) = 1703 Pa

Interpretation of Results

Analysing the figures and derived internal friction angle and cohesion values, we observe notable differences between the SPH and SI samples. The SPH sample exhibits a higher internal friction angle and cohesion, attributed to increased particle interlocking resulting from its elongated shape. In contrast, the SI sample's shape impacts shear stress by enhancing frictional contact areas between particles, resulting in a minor effect compared to the interlocking behaviour observed in SPH samples. Consequently, the higher cohesion observed in SPH samples compared to SI samples can be attributed to the superior particle interlocking behaviour inherent to long particles.

3.3 Shear Stress Analysis

This section intricately examines the relationship between the sphericity index (SPH), aspect ratio (AR), size index (SI), triple particle size index (TPSI), and shear stress within granular materials. The analysis delves deeply into the complex interplay between particle morphology and shear stress, especially when subjected to constant normal stresses. The "average shear force" calculation involved determining the residual shear strength under quasi-state shear conditions, offering insight into the average force required to sustain shear deformation within the system. Regarding the representation of results, while stress values could provide more detailed information by considering the cross-sectional area of shearing, our study primarily presents results in a force, following the default representation in the simulation program EDEM. We acknowledge that stress values might offer greater insight when considering the cross-section area of the model; however, delivering results in terms of force does not impede understanding, as it is a concept widely comprehended within the scientific community.

3.3.1 Influence of Sphericity Index (SPH) on Shear Stress

Our investigation commences with a series of illustrative figures, brightly portraying shear stress variations concerning horizontal strain for particle samples characterised by diverse sphericity indexes under constant normal stresses. We derive the internal friction angle by employing the arctangent of the ratio of shearing stress to normal stress ($\varphi = \arctan(\tau/\sigma)$).

Remarkably, our findings showcase an inverse correlation between the sphericity index and the internal friction angle. As sphericity decreases, the peak friction angle tends to reach its limit with significantly higher values. This sphericity reduction influences shear stress behaviour, particularly for 2D elliptical particles. Notably, previous research conducted by experts in the field has reported similar results for 3D ellipsoid multi-sphere assemblies (Rothenburg and Bathurst, 1992; Gong and Liu, 2017).

The impact of sphericity on particle specimens becomes even more pronounced. This phenomenon illustrates the increasing interlocking connections between particles under normal stress, with longer particles exhibiting more noticeable particle interlocking. For instance, under a normal load of 15N, we observed a substantial increase in shear load (from 5N to 9N) when transitioning from spherical (SPH = 100%) to non-spherical particles (SPH = 81%). However, it is noteworthy that the increase in shear stress diminishes for strongly spherical particles and vice versa.

There was a necessity for a more thorough assessment of the influence of the sphericity index on particles' shear behaviour under constant normal stress. Figure 4.5 illustrates the sphericity index's impact on particles' shear stress. Lower sphericity index values enhanced interlocking among particles, increasing the shear stress. Additionally, figure 4.6 demonstrates that reduced stress on the particles led to the dilation of interlocking particles, consequently decreasing shear strength. Decreasing the sphericity index intensified particle interlocking, gradually raising shear stress. These tightly interlocked particles face difficulty moving against each other due to high normal stress, resulting in anisotropy. Reduced anisotropy in the sample correlates with a lower friction angle (Rothenburg and Bathurst, 1991). Moreover, the shear strength of particle samples increases with lower spheric particles. For instance, shear force rises by approximately 26% as particles transition from complete spherical particles (SPH = 100%) to particles with (SPH = 98%) under a normal load of 15N, as illustrated in Table 4.1.

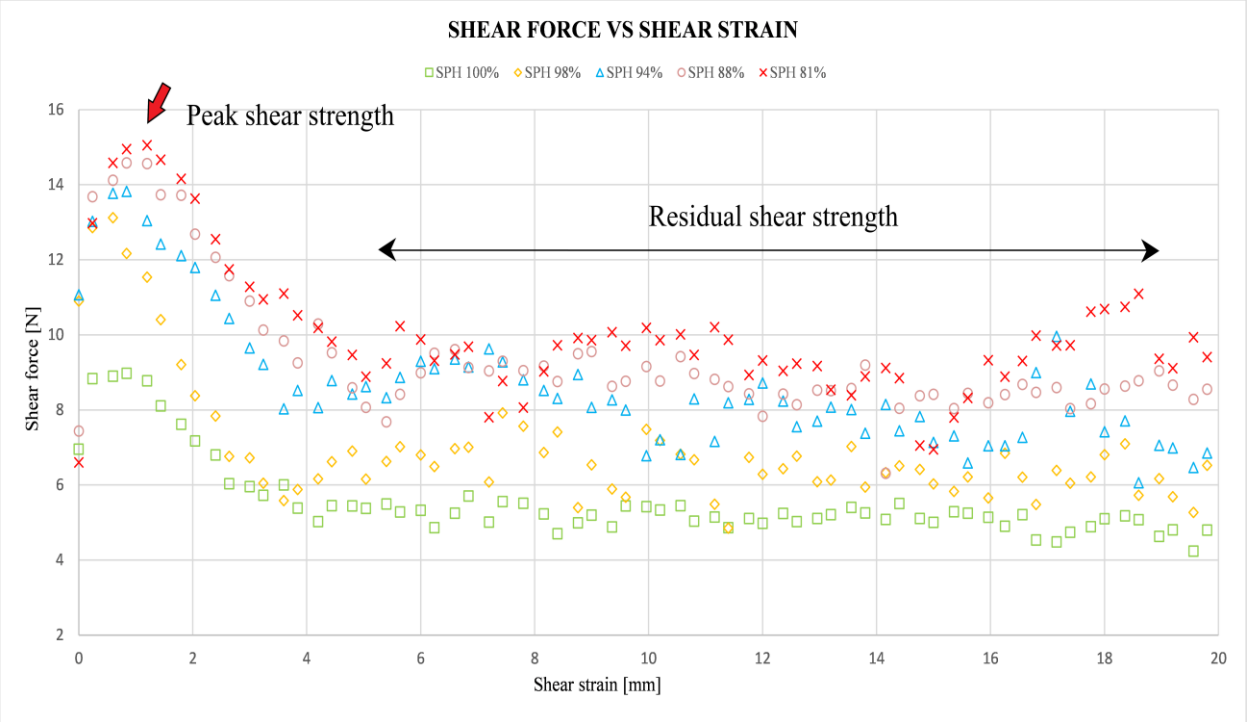

Figure 3.5. Shear stress–shear strain curves of samples with various sphericity at a normal load of 15N

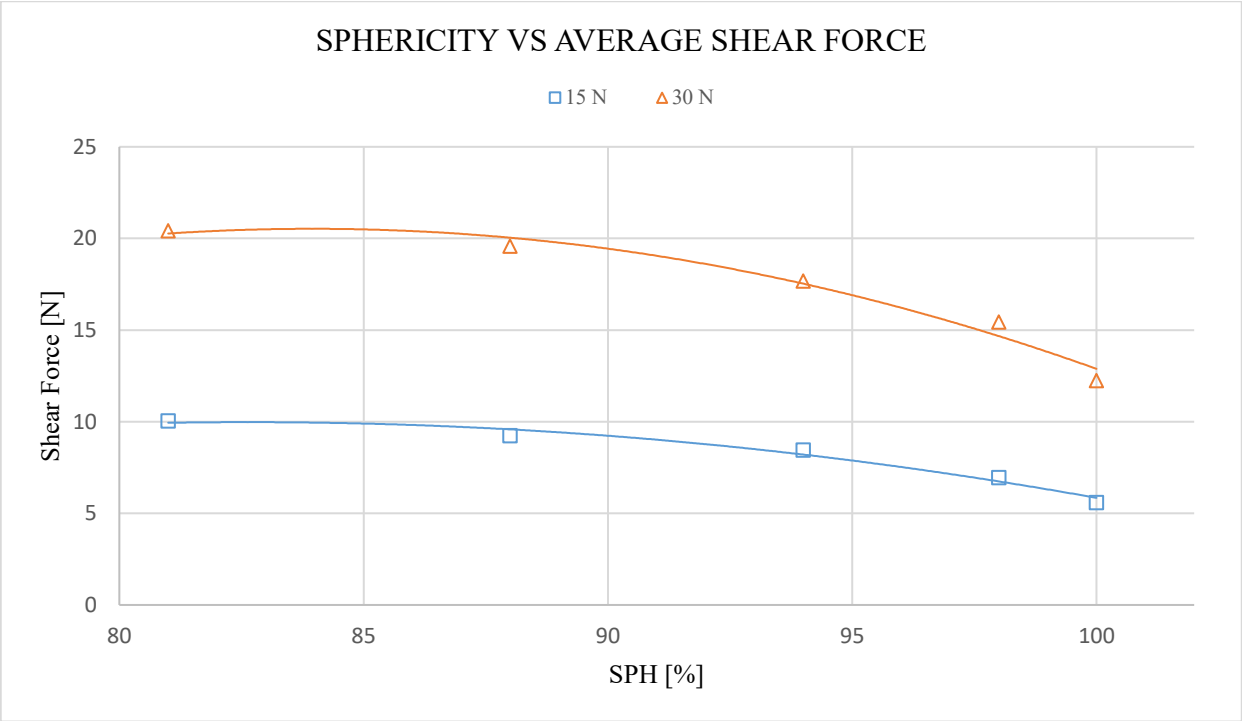

Figure 3.6. Shear stress with various sphericity at original and double normal load 15 and 30 N

Table 3.1. Shear force corresponding to the SPH and AR at the original and double normal load.

Sphericity index SPH %	**Particle Aspect Ratio AR**	**Shear force N**	**Shear force Increased percentage %**	**Shear force for the double normal load N**	**Increasing in shear percentage %**
100	1	5.588485	0.0	12.25857	0.0
98	0.8	6.964829	24.6	15.4422	26.0
94	0.67	8.469422	51.6	17.6862	44.3
88	0.57	9.247369	65.5	19.58606	59.8
81	0.51	10.04465	79.7	20.42614	66.6

Figure 4.6 shows a nonlinear correlation between the sphericity index and shear force. An exponential model effectively uses the particle Aspect Ratio AR to capture and represent this nonlinearity. The Aspect Ratio is defined as the ratio of b/a, as illustrated in Chapter 3, where b is the length of the minor axis, and a is the length of the particle's central axis.

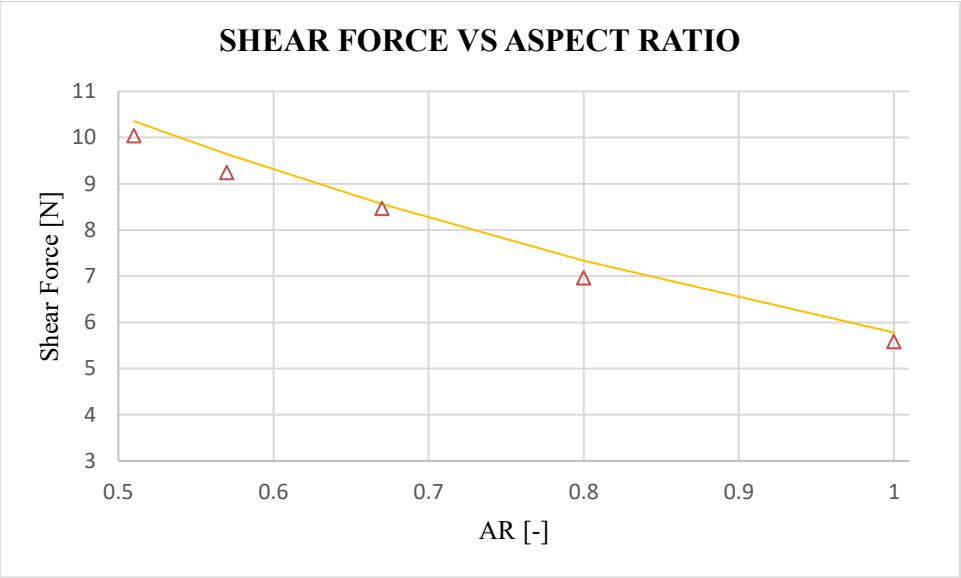

Figure 3.7. The correlation between the sample's AR and shear force under a normal load of 15N

Figure 4.7 visually presents the correlation between the sample's AR and shear force under a normal load of 15N. The figure introduces a new exponential model used to depict this correlation. The mathematical expression for this exponential model is detailed in Equation 4.1.

$$T_{AR} = c_{12}\, N\, e^{(-AR\, c_{11})} \qquad 3.1)$$

The shear aspect ratio T_{AR} [N] determines the shear force value through the function of AR [-]. The exponential function is characterised by two parameters, c_{11} [-] and c_{12} [-], shaping its behaviour. Additionally, N [N] represents the applied normal load to the particles.

Moreover, figure 4.8 demonstrates the suitability of the exponential model in representing and predicting the correlation between shear force and the AR. The model's effectiveness is particularly highlighted by its ability to predict shear force values for the second data group. This group corresponds to tests conducted under a doubled normal load of 30N, while the first group represents tests conducted under the normal load of 15N. The model achieves a remarkable coefficient of determination R^2 value of 0.96, affirming its reliability in capturing the correlation under varied normal load conditions. Table 4.2 shows the R^2 and the model parameter values.

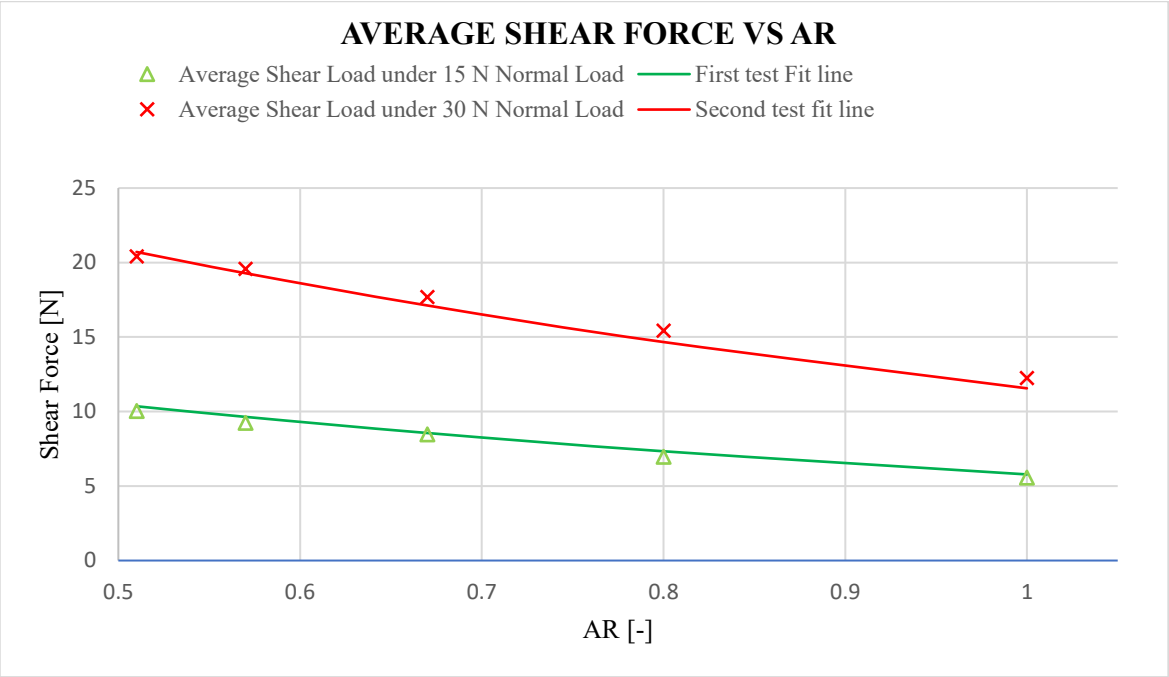

Figure 3.8 Shear force and the Aspect Ratio under the application of the exponential model

Table 3.2. Aspect Ratio exponential model parameters

Parameters	c_{11}	c_{12}	R^2
Parameter values of the First experiment 15N	0.19	1.2667	0.966
Parameter values of the second experiment 30N	0.19	1.2667	0.964

Our exploration of the SPH and the AR influence on shear stress in granular materials offers a nuanced understanding of how granular materials' morphology shapes behave under varying normal stress conditions.

3.3.2 Effect of Size Index (SI) on Shear Stress

This section delves into the impact of Size Index (SI) on shear stress within granular materials. Illustrated graphs vividly demonstrate SI's effect on the relationship between horizontal strain and shear stress under a consistent normal stress rate. Calculating the internal friction angle using the arctangent of the shear stress ratio with the normal stress ratio ($\varphi = \arctan(\tau/\sigma)$) shows a clear positive correlation emerges between the internal friction angle and particle size, denoted by φ. The internal friction angle increases proportionally with particle size, indicating a considerable influence of the particle size on the shear strength.

Comparative analysis of diverse particle samples underscores the profound impact of SI on shear strength characteristics. This phenomenon underscores the intricate interplay between moment force development and the evolution of interlocking connections between particles under normal stress. Larger particles exhibit a more pronounced interlocking due to the elevated moment force required for their rotation. For instance, under a normal load of 350N, shear force increased from 136 N to 158 N as particle SI transitioned from 50% to 150%. Notably, this substantial increase in shear force diminishes for particles with smaller SI values. These findings align with previous

research by (Alias et al., 2014), who demonstrated that the shear strength of granular materials is significantly influenced by particle size. Larger particles inherently possess enhanced shear strength due to increased contact points, interlocking, and effective stress transfer area. Additionally, larger particles exhibit greater resistance to deformation and displacement, further contributing to their superior shear strength characteristics. Moreover, the optimised packing arrangement facilitated by larger particles reduces the void ratio and strengthens interparticle forces, further augmenting shear strength.

Figures 4.9 and 4.10 provide deeper insights into SI's impact on particles' shear behaviour under constant normal stress. Figure 4.9 comprehensively illustrates how SI influences shear stress in particles. Higher SI values promote interlocking among particles, leading to an increase in the shear stress values. Additionally, figure 4.10 illustrates that reduced normal stress on particles leads to the dilation of interlocking particles, decreasing the total shear force. Furthermore, as the normal stress rate increases, particles experience a more effective interlocking rate and a gradual increase in shear stress. However, high normal stress restricts movement between particles, leading to anisotropy. Samples with reduced anisotropy correlate with lower friction angles.

In Fig. 4.9, the continuous lines represent the best-fit line of the readings. These lines are included in the figure's shear force representation to provide a more straightforward visual depiction of the variations between different experimental datasets. While the peak shear stress, indicative of shear failure, is not explicitly represented by the continuous lines, they highlight trends and differences in shear force behaviour across the various experiments.

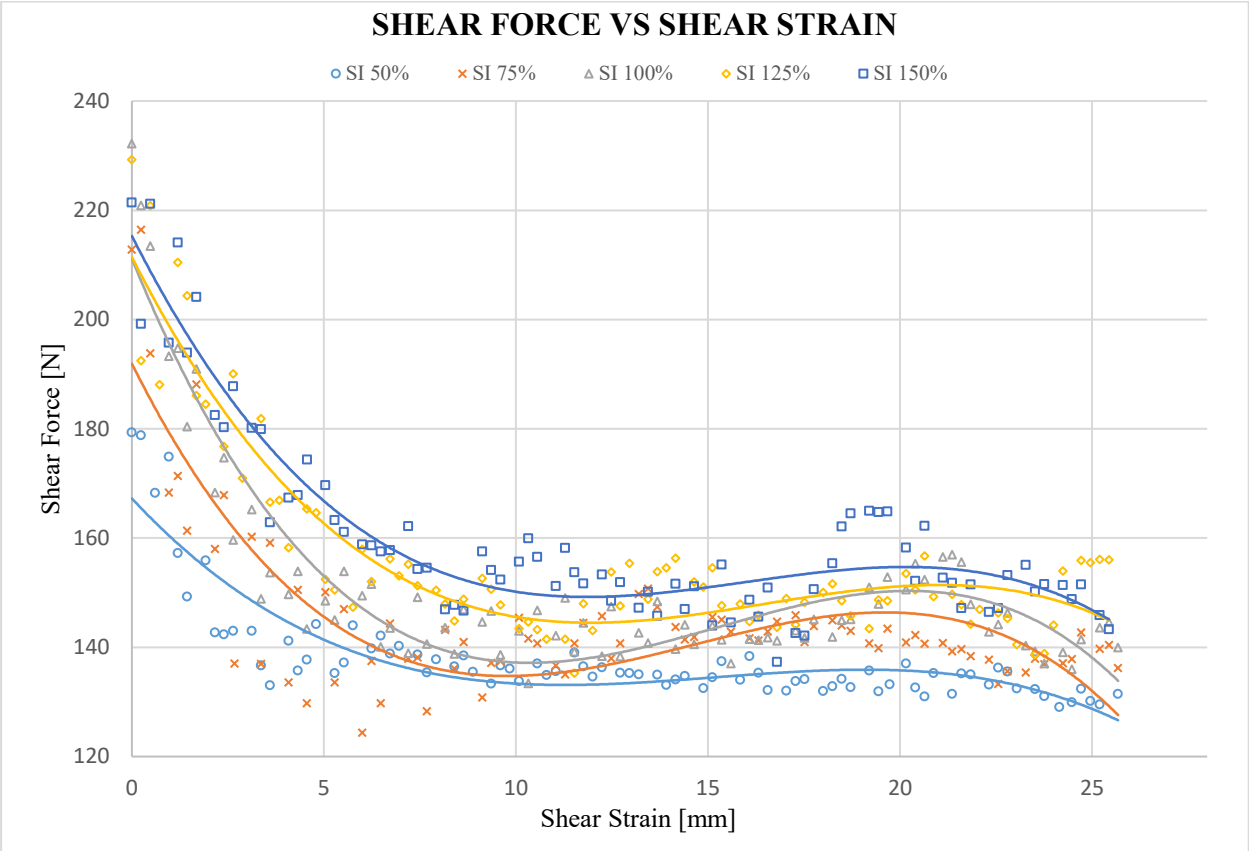

Figure 3.9. Shear force vs shear strain plots of samples with varying SI at 350N normal load

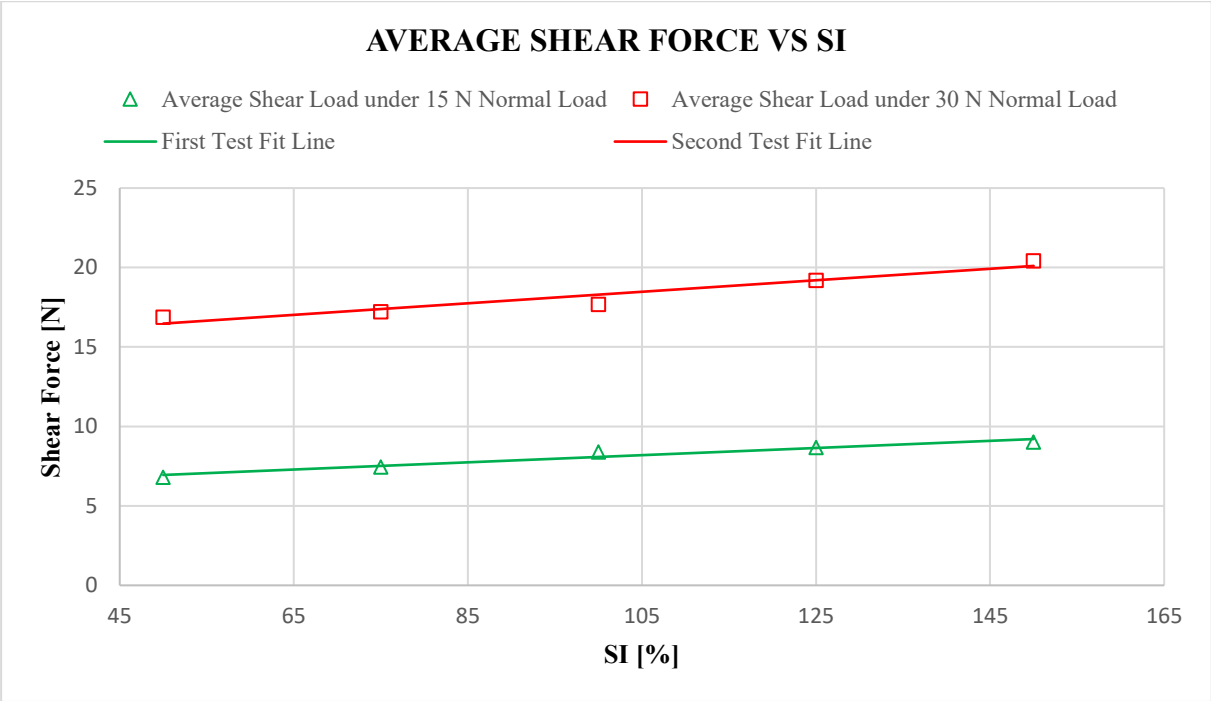

Figure 3.10. Shear stress with a variety of SI at 15 N and 30 N normal load

Simultaneously, an increase in SI corresponds to a rise in shear force. For example, under a 30 N normal load, increasing particles' SI from 50% to 150% results in a shear load increase of approximately 18%. Further, Table 4.4 provides more details.

Figure 4.10 demonstrates a linear relationship between the size index (SI) and shear load. A corresponding rise in SI accompanies the increase in the shear load, and this correlation is well-described by linear regression Equation 4.2, as evidenced by the high R^2 value.

$$T_{SI} = SI\ c_{21} + N\ c_{22} \qquad 3.2)$$

The shear size index T_{SI} [N] determines the shear load value through a size index (SI) [-] function. The shear size index function is characterised by two parameters, c_{21} [-] and c_{22} [-], which shape its behaviour. Additionally, N [N] represents the applied normal load to the particles. Equation 4.2 represents the shear loads corresponding to 15 and 30N normal loads. Table 4.3 illustrates the parameters of equation 4.2.

Table 3.3. The fit parameters of Equation 4.2

Parameters	c_{21}	c_{22}	R^2
Parameter values of the First experiment 15N	0.0226	0.3879	0.95
Parameter values of the second experiment 30N	0.0363	0.4886	0.93

Table 3.4. Shear load corresponding to the size index at the original and double normal load

Size index %	shear load	Shear load Increased percentage %	shear load for the double normal load	Shear load Increased percentage %
50	6.816099	0.0	16.88417	0.00
75	7.460942	9.5	17.22805	2.04
100	8.400623	23.2	17.68707	4.76
125	8.675094	27.3	19.19909	13.71
150	9.033017	32.5	20.43415	21.03

3.3.3 Triple Particle Size Index (TPSI) and Shear Stress Behaviour

This section delves into the intricate relationship between the Triple Particle Size Index (TPSI) and shear stress in granular materials under constant normal stresses. In the figures presented below, the connection between shear stress and horizontal strain for particle samples, varying in size indexes, is vividly represented. The internal friction angle demonstrates a positive correlation with particle size. As particle size increases, the peak friction angle approaches higher limits, indicating the pivotal role of growing particle size. This effect is especially significant for 2D elliptical particles, with similar outcomes reported in previous studies (Rothenburg and Bathurst, 1992). Moreover, compatible findings were observed in 3D ellipsoid multi-sphere assemblies (Gong and Liu, 2017).

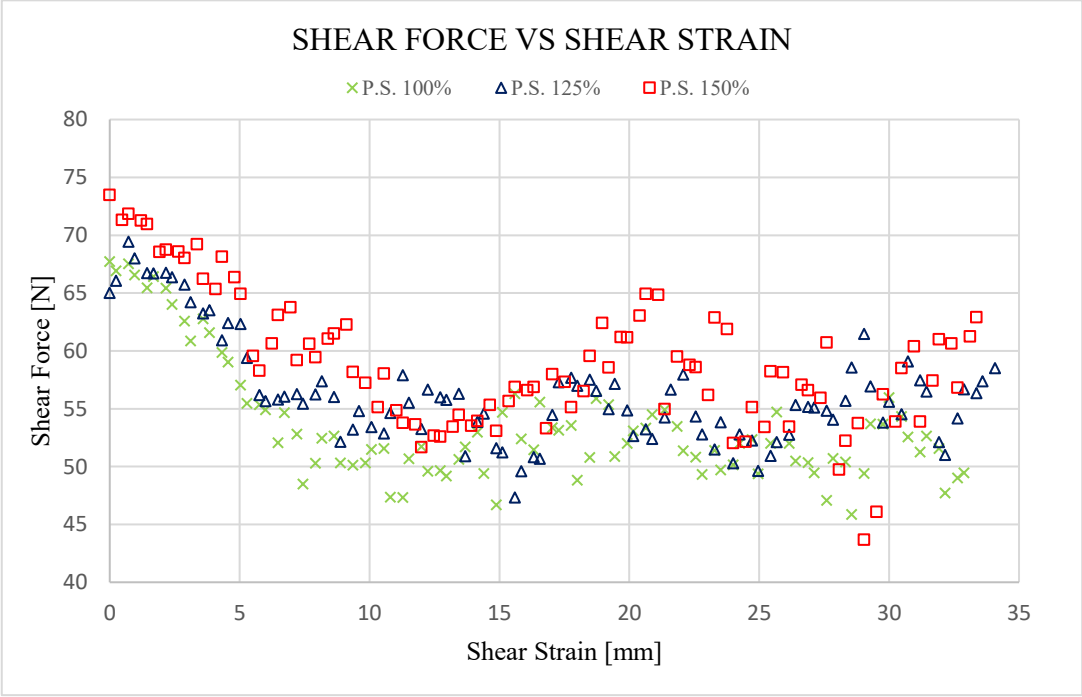

Figure 3.11. The shear load with shear displacement curves of samples with various SI at a normal load of 70N

The Size Index (SI) impact becomes even more visible in particle specimens, as highlighted in Figure 4.11. This representation captures SI's influence on particle shear load. The phenomenon is explained by the amplification of moment force and the intricate interlocking connections between particles under normal stress conditions. Larger particles become more frictionally interlocked due to the augmented particles' contact area, increasing the critical moment required to rotate the particle. For instance, when the particle's SI transitioned from 100% to 150% at a normal load of

70N, the shear force increased by approximately 13%, escalating from 51N to 58N—conversely, the change in shear force diminished for smaller size index particles, and vice versa.

3.3.4 Shear Stress Responses to the Shape Indexes

In the context of shear stress responses to different shape indexes, our investigation has revealed several crucial findings:

Influence of Sphericity Index (SPH):

1. The sphericity index (SPH) and aspect ratio (AR) of particles significantly impact shear stress in granular materials.
2. Lower sphericity index values enhance interlocking among particles, increasing the shear stress.
3. The shear strength of particle samples increases with lower sphericity particles.
4. Reducing stress on the particles leads to the dilation of interlocking particles, consequently decreasing shear strength.
5. The impact of sphericity on particle specimens becomes more pronounced at higher normal stresses.
6. An exponential model using the particle Aspect Ratio AR effectively captures the non-linear correlation between the sphericity index and shear force.
7. The exponential model achieves a remarkable R^2 value of 0.96, affirming its reliability in capturing the correlation under varied normal load conditions.

Effect of Size Index (SI):

1. There is a positive correlation between SI and internal friction angle. As SI increases, the peak friction angle also increases.
2. Larger particles exhibit enhanced shear strength due to increased contact points, interlocking, and effective stress transfer area.
3. Larger particles resist deformation and displacement more effectively, contributing to their superior shear strength characteristics.
4. Reduced normal stress on particles leads to the dilation of interlocking particles, decreasing shear force.
5. As the normal stress rate increases, particles experience a more effective interlocking rate and a gradual increase in shear stress.
6. An increase in SI corresponds to a rise in shear force.

Effect of Triple Particle Size Index (TPSI):

1. There is a positive correlation between TPSI and internal friction angle. As TPSI increases, the peak friction angle also increases.
2. Larger particles exhibit enhanced shear strength due to increased contact points, interlocking, and effective stress transfer area.
3. Larger particles resist deformation and displacement more effectively, contributing to their superior shear strength characteristics.
4. Reduced normal stress on particles leads to the dilation of interlocking particles, decreasing shear force.
5. As the normal stress rate increases, particles experience a more effective interlocking rate and a gradual increase in shear stress.
6. An increase in TPSI corresponds to a rise in shear force.

Summary

These studies found that particle indices (SPH), (AR), (SI), and (TPSI) play significant roles in determining the shear stress behaviour of granular materials. The results suggest that these

parameters can be used to predict the shear stress behaviour of granular materials in various applications.

3.4 Volumetric Strain Behaviour

In this section, we delve into the analysis of volumetric strain, a critical parameter in understanding the mechanical behaviour of granular materials under shear loading conditions. Volumetric strain, denoted by the change in the total volume occupied by particles, offers valuable insights into the compaction and deformation processes occurring within the particle assembly. Our approach involves tracking the movement of a large sphere that is responsible for applying normal load during the shear test, facilitated by the simulation program EDEM. We aim to elucidate the intricate relationship between particle morphology, applied loading conditions, and resulting volumetric changes within the granular material system through meticulous analysis and interpretation of volumetric strain data.

3.4.1 SPH Impact on Volumetric Strain

Our investigation of volumetric strain behaviour reveals intriguing insights into how the sphericity index (SPH) influences granular materials under varying normal stresses.

Figure 4.12 compares volumetric strain changes against horizontal strain under different normal stresses. Notably, we observe an inverse relationship between normal stress and volumetric strain. As normal stress increases, the overall volumetric strain decreases, indicating a reduced level of dilation under higher normal stress conditions.

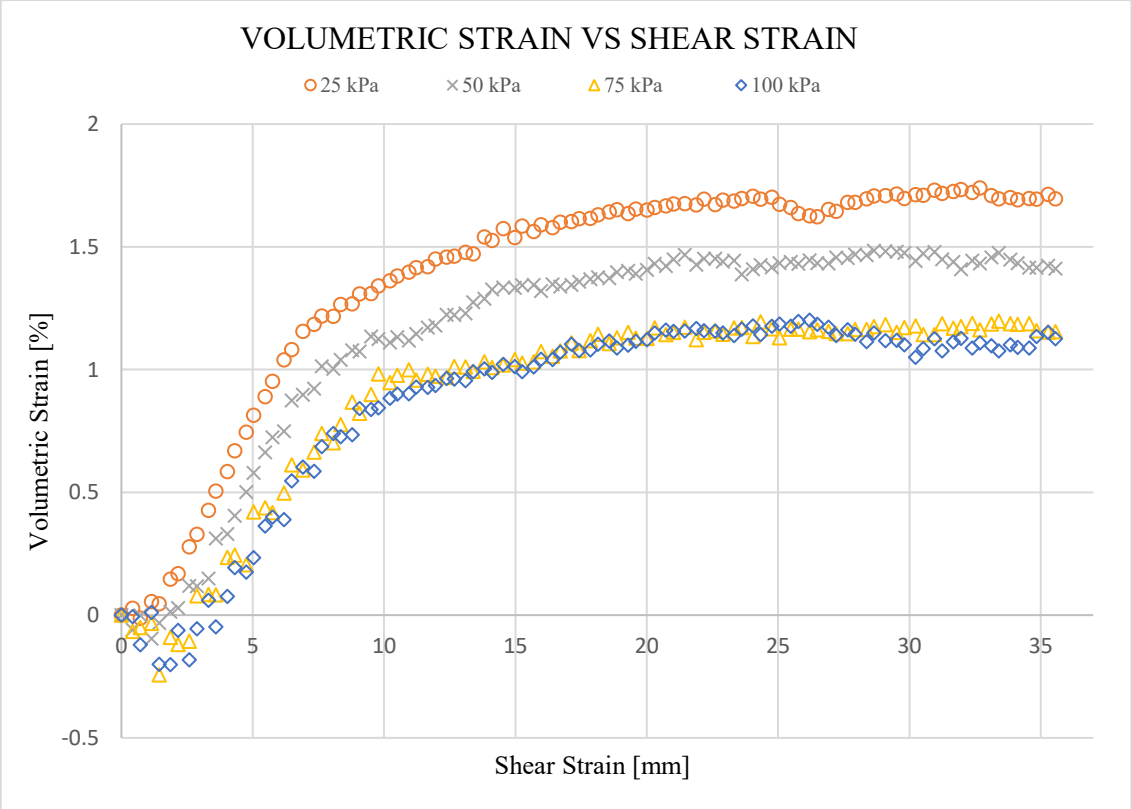

Figure 3.12. Volumetric-shear strain for various normal stresses (SPH = 81%)

Figure 4.13 further clarifies the impact of sphericity on the volumetric strain. It highlights a significant increase in dilatancy with lower SPH values, suggesting that shape characteristics and normal stress influence particle dilatancy.

To quantify this impact, we note that at a normal load of 15N, an assembly with sphericity particles of (SPH=81%) exhibits a volumetric strain 44% higher than an assembly with SPH values of

100%. This substantial difference emphasises the role of SPH in governing volumetric strain behaviour.

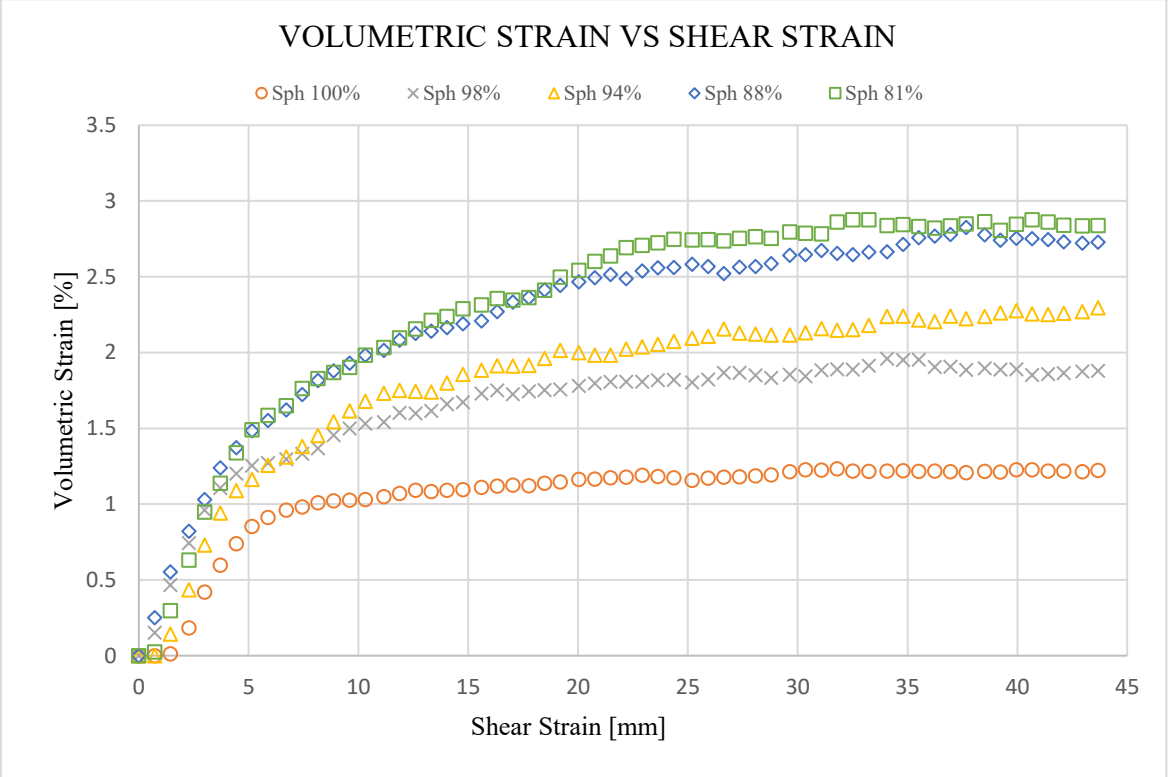

Figure 3.13. Volumetric-shear strain with various sphericity at a normal load of 15N

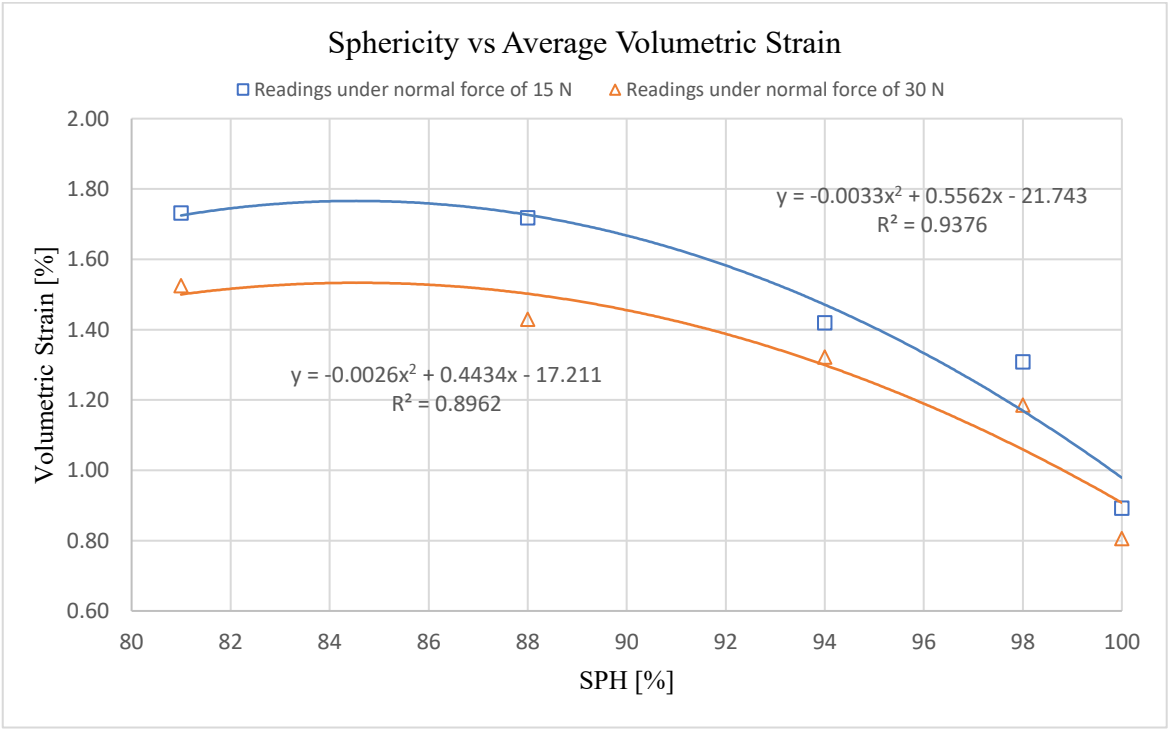

Figure 3.14. Volumetric strain for different Sphericity values at a normal load of 15 and 30 N

Figure 4.14 presents the average volumetric strain for different SPH values subjected to 15 and 30 N normal loads. The results indicate an inverse correlation between SPH and volumetric strain, with an increase in the volumetric strain as the SPH values decrease. A squared equation 4.3 accurately describes this nonlinear relationship with a high R^2 value, where equation 4.3 represents

the readings under normal loads of 15 and 30N. At the same time, Table 4.5 describes the parameters of the equation 4.3. Figure 4.14 underscores the influence of normal load on dilatancy, demonstrating that higher normal loads lead to a reduced level of volumetric strain compared to lower normal load. This finding further emphasises the intricate interplay between normal load and volumetric strain.

$$V_{SPH} = c_{31}\, SPH^2 + c_{32}\, SPH + c_{33} \qquad 3.3)$$

Table 3.5. The fit parameters of the Equation 4.3

Load	c_{31}	c_{32}	c_{33}	R^2
15N	-0.0033	0.5562	-21.743	0.94
30N	-0.0026	0.4434	-17.211	0.9

The volumetric strain V_{SPH} determines the volumetric strain value through a sphericity index (SPH) function. The function is characterised by three parameters, c_{31} [-], c_{32} [-] and c_{33} [-], which shape its behaviour.

3.4.2 SI's Influence on Volumetric Strain

Examining the influence of Size Index (SI) on volumetric strain provides crucial insights into the behaviour of granular materials under varying normal loads.

Figure 4.15 depicts the volumetric and horizontal strain relationship under different normal loads. A clear reverse correlation emerges between overall volumetric strain and normal load; as normal load increases, the overall volumetric strain decreases, highlighting a lower dilation of particle volume strain under higher normal load conditions.

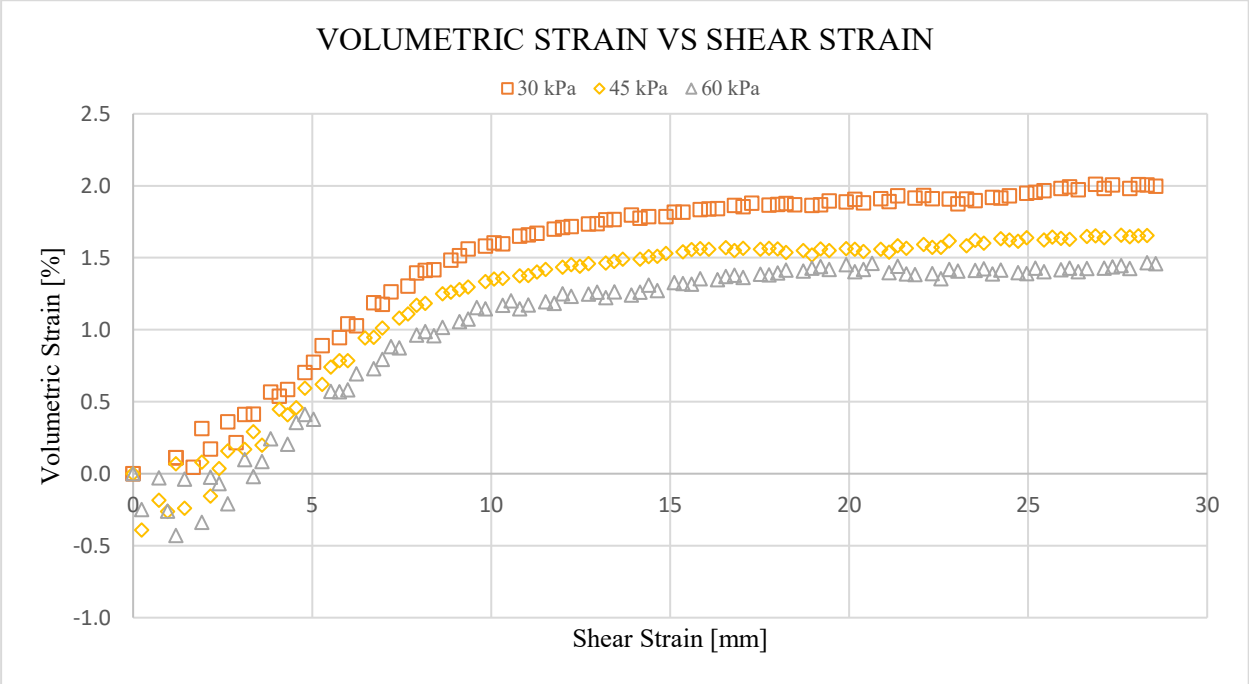

3.15. Variations of volumetric strain with shear strain for various normal stresses (SI 150%) normal stress 30kPa, 45kPa, 60kPa

Figure 4.16 explores the impact of particle SI on volumetric strain. It illustrates that as the particle's SI increases, its volume dilation also increases. This relationship underscores the dependency of particle volume dilation on particle shape and the applied normal load levels (Talafha and Oldal, 2021).

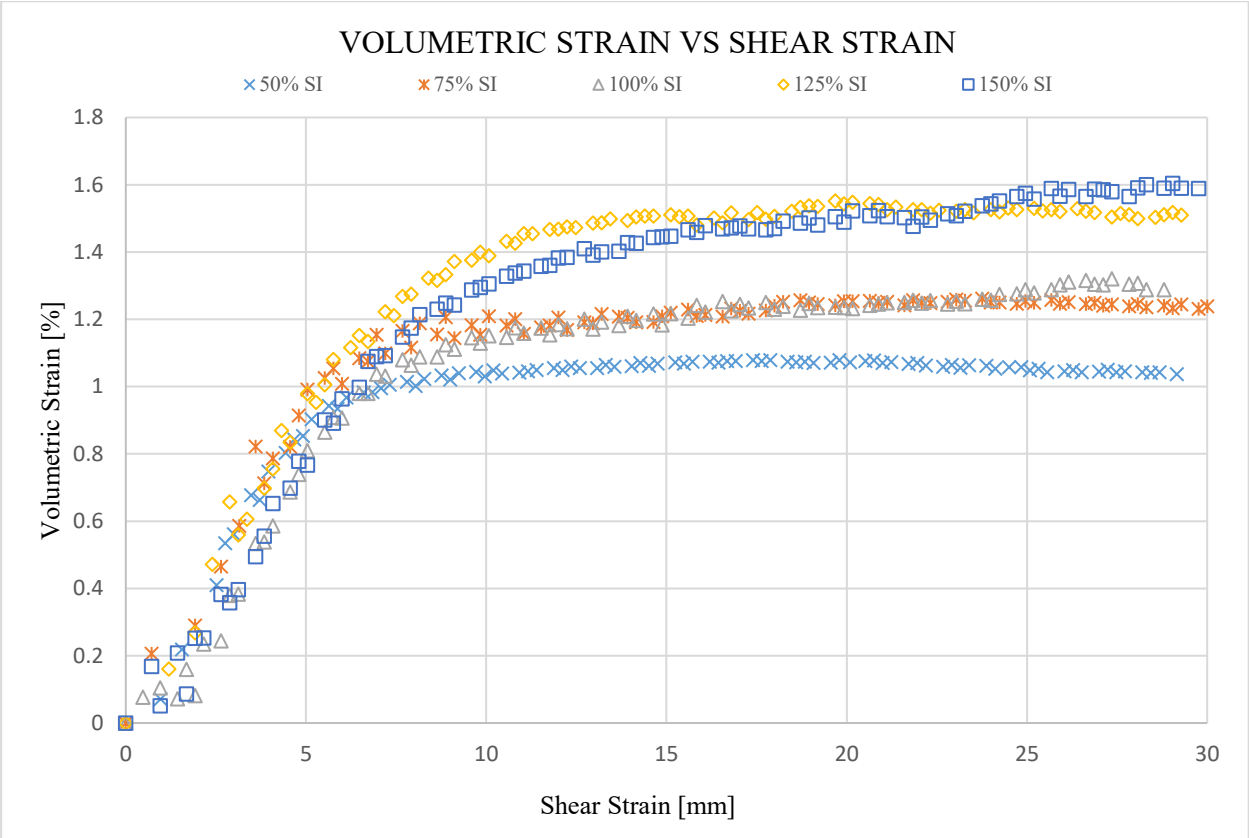

Figure 3.16. Variations of volumetric strain with shear strain for different size indexes at normal Stress of 30 kPa

Figure 4.17 presents the average volumetric strain values obtained from tests conducted with different size index (SI) values under varying normal stresses of 3 and 30 kPa. The results highlight a positive linear correlation between SI and volumetric strain. This relationship is captured by the linear equation 4.4, representing the readings under normal stress of 3 kPa and 30 kPa, while Table 4.6 describes the equation 4.4 parameters. Furthermore, Figure 4.17 underscores the influence of normal stress on dilation. The data demonstrate that higher normal stresses lead to lower levels of dilation. For instance, at a normal stress of 30 kPa, the dilation value is significantly reduced compared to the normal stress of 3 kPa. Notwithstanding this effect, the correlation between volumetric strain and SI remains evident, as the value increases by approximately 28% when the assembly particles' SI changes from 50% to 150%. This observation underscores the complex interplay between SI, normal stress, and volumetric strain, highlighting the intricate nature of granular material behaviour under varying conditions.

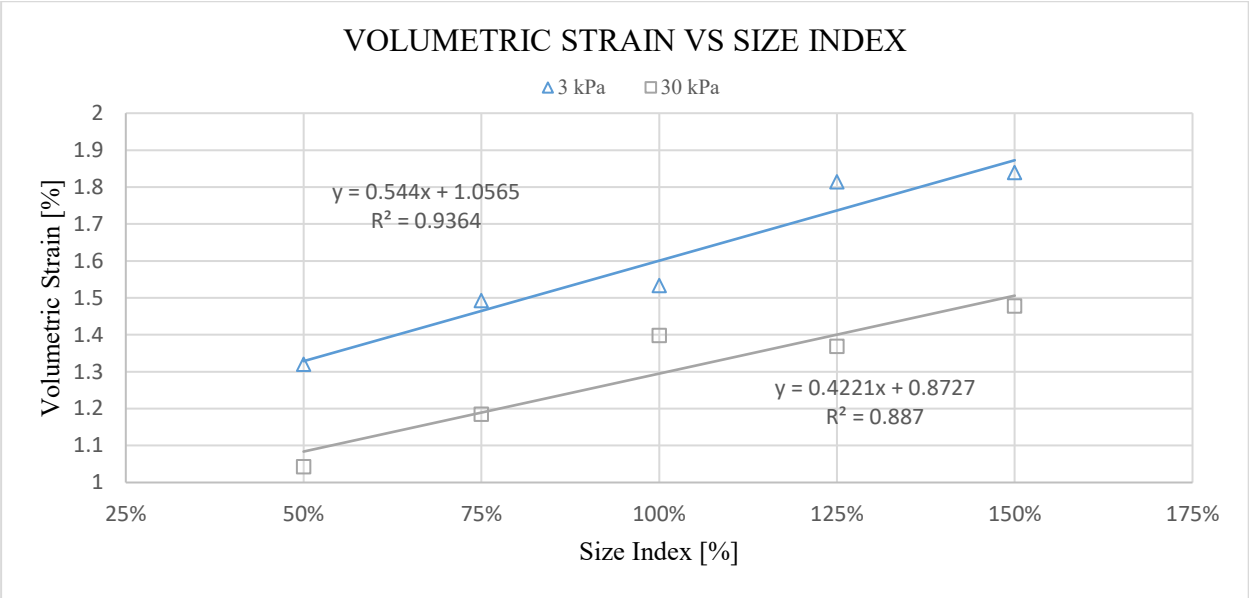

Figure 3.17. Volumetric strain for different size index at a normal stress of 3 and 30kPa

$$V_{SI} = c_{41}\, SI + c_{42} \qquad 3.4)$$

Table 3.6. The fit parameters of the Equation 4.4

Load	c_{41}	c_{42}	R^2
15N	0.544	1.0565	0.94
30N	0.4221	0.8727	0.89

The volumetric strain V_{SI} determines the volumetric strain value through a size index (SI) function. The function is characterised by two parameters, c_{41} [-] and c_{42} [-], which shape its behaviour.

3.4.3 TPSI and Volumetric Strain Characteristics

Understanding the relationship between the Triple Particle Size Index (TPSI) and volumetric strain sheds light on the intricate behaviour of granular materials under constant normal stresses.

Figure 4.18 presents a comparative analysis of volumetric variations concerning horizontal strain for different triple particle Size Indices (TPSI) under consistent normal stresses. An apparent trend emerges: the overall volumetric strain increases proportionally with the increase of TPSI. This pattern signifies that dilatancy in larger particles intensifies as TPSI increases, underscoring the significant influence of particle shape on dilatancy under varying normal loads.

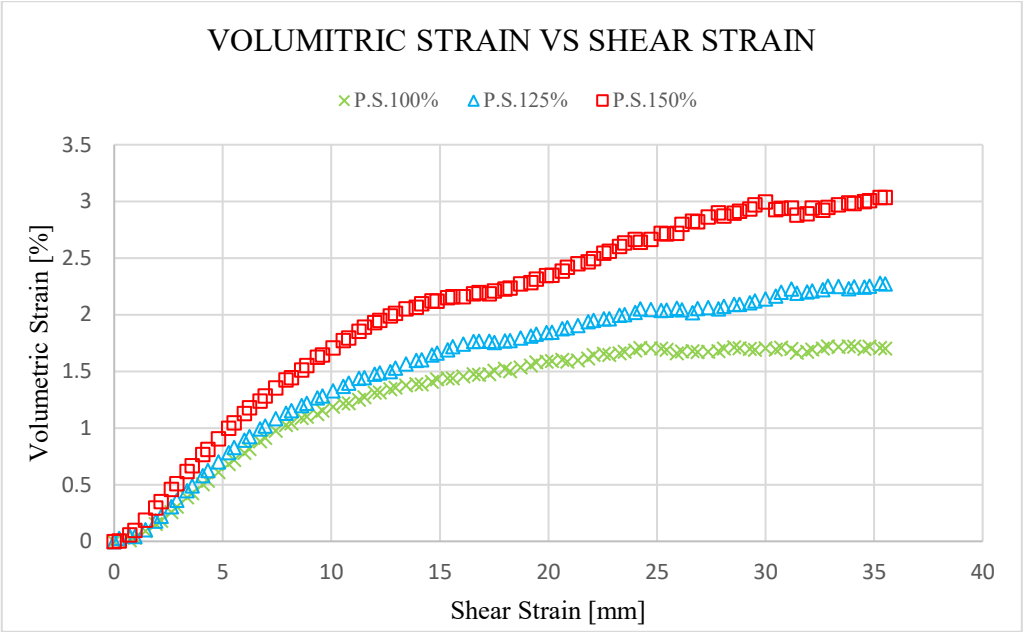

Figure 3.18. Variations of volumetric strain with shear strain for different size indices at a normal stress of 8 kPa.

To illustrate the volumetric strain characteristics, the assembly with SI=150% exhibits dilation values 57% larger than those with SI=100% at a normal stress of 8 kPa. This substantial difference emphasises the pivotal role played by TPSI in shaping volumetric strain characteristics, highlighting the complex interplay between particle size, shape, and normal stress in granular material behaviour.

3.4.4 Volumetric Strain Responses to Different Shape Indexes

In the study of volumetric strain behaviour, several key factors were analysed:

SPH Impact on Volumetric Strain

1. A comparison of volumetric strain changes versus horizontal strain under different normal stresses revealed that the overall volumetric strain decreased as normal stress increased, indicating lower dilation levels under higher normal stress.
2. Dilatancy in larger strains increases with a lower sphericity index (SPH), suggesting a correlation between dilatancy and particle shape features and normal stress.
3. Specifically, assemblies with elongated particles (SPH=81%) showed 44% higher dilation values than complete sphere particles with SPH values of 100% under normal stress of 4150 Pa.

SI's Influence on Volumetric Strain

1. A reverse correlation was observed between overall volumetric strain and normal stress. Higher normal stress led to lower volumetric strain and vice versa.
2. Increasing the size index (SI) resulted in higher particle volume dilation. The particles' volume dilation depended on particle shape and the applied normal stress. For instance, at a 30 kPa normal stress, the dilation value increased by 28% when the assembly particles' SI changed from 50% to 150%.
3. Higher normal stresses lead to a lower dilation than lower normal stresses.

TPSI Impact on Volumetric Strain

1. Comparing volumetric strain variations with horizontal strain for various TPSI under constant normal loads revealed that overall volumetric strain increased with higher TPSI values. Indicating that dilatancy in larger particles increased with higher TPSI.
2. Dilatancy was found to be influenced by both particle shape and normal load. For instance, assemblies with TPSI =150% exhibited 57% larger dilation values than those with TPSI =100% under a normal stress of 8 kPa.
3. TPSI plays a significant role in shaping volumetric strain characteristics.

Summary

the study highlights the crucial influence of varied factors, such as TPSI, SI, and SPH, along with normal stress, on determining the volumetric strain behaviour of granular materials. The findings underscore that these parameters can serve as reliable predictors for understanding and anticipating the volumetric strain behaviour of granular materials.

3.5 Average Contact Numbers Investigation

3.5.1 SPH's Effect on Average Contact Numbers

Understanding the interactions within granular materials is central to comprehending their behaviour. One crucial parameter in this study is the coordination or contact number (CN), representing the average number of particles in contact within the assembly. This parameter offers valuable insights into the granular material's dynamics as it directly correlates with the contact points between particles. As a result, CN can be used as a descriptor for the behaviour of granular materials, encapsulating the details of their interactions (Danesh et al., 2020).

The link between the Sphericity Index (SPH) and the Coordination Number reveals an interesting pattern. Decreasing SPH, indicating a departure from a perfectly spherical shape, leads to a continuous increase in the coordination number. This phenomenon suggests additional interlocking among particles as the sphericity decreases. The relationship between CN and SPH, as depicted in Figure 4.19, demonstrates this tendency. This discovery contradicts the findings of a study conducted by (Asadi and Mirghasemi, 2018), which focused on elliptical particles. Their research indicated an initial rise in contacts as eccentricity increased, followed by a decline at higher eccentricity levels. In contrast, our investigation revealed an inverse relationship: as the (SPH) decreased, there was a simultaneous increase in the coordination number (CN) between the particles.

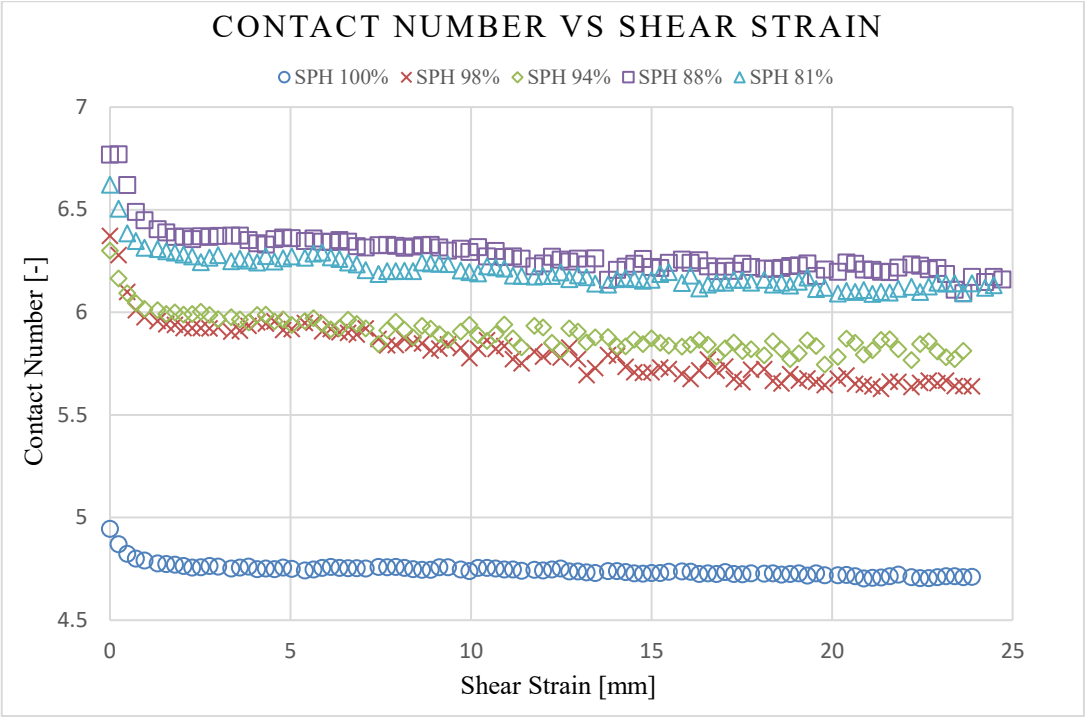

Figure 3.19. Variation of CN versus shear strain with various sphericity at a normal stress of 4150 Pa

Figure 4.20 provides a nuanced perspective on CN under varying conditions of stress. Interestingly, it illustrates that applying high stress to the sample consistently results in a higher coordination number regardless of the SPH index. This observation underscores that stress shapes particle interactions within granular materials. However, it is crucial to note that the initial strain levels induce an immediate decrease in CN at lower normal stress due to pronounced dilatation. This drop is attributed to the dilation effect caused by the initial strain, highlighting the complex interplay between normal stress, dilation, and contact numbers.

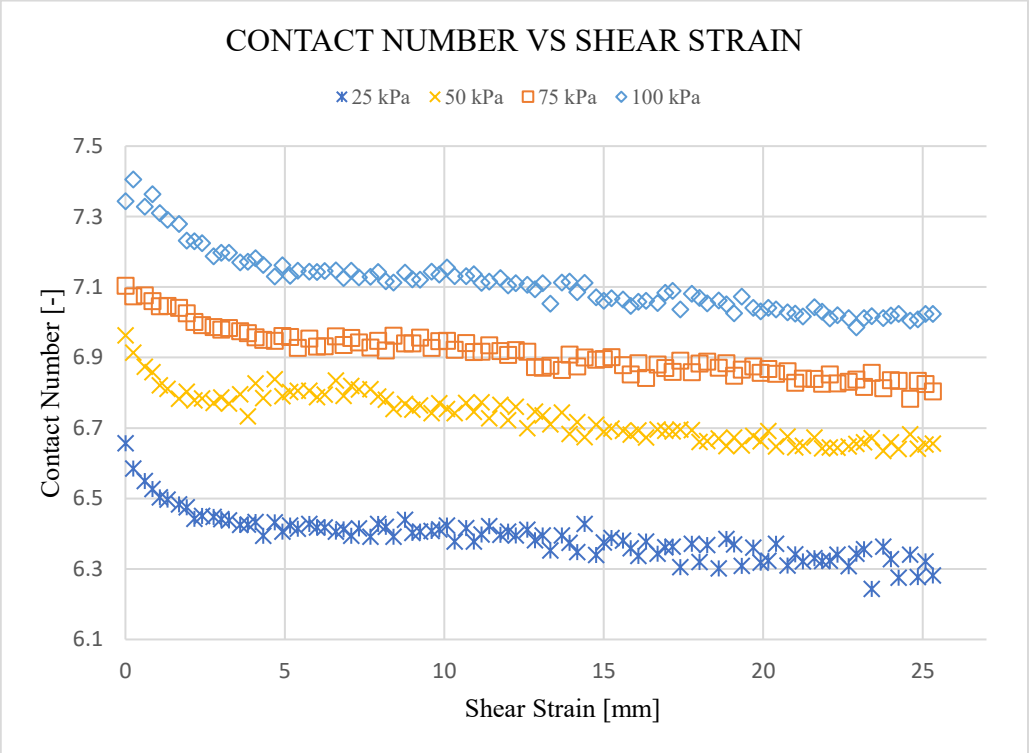

Figure 3.20. Variation of CN versus shear strain for various normal stresses (SPH = 81%)

Exploring SPH's effect on average contact numbers reveals intricate dynamics within granular materials. The continuous increase in CN with decreasing SPH challenges existing theories and invites further exploration into the relationship between particle shape, interlocking, and contact behaviour. Furthermore, Table 4.7 details the relationship between the contact number and the sphericity index.

Table 3.7. correlation between the SPH and the CN

Sphericity index %	Average contact No.	Average contact No. Increased percentage %	Average contact No. For double normal load	Average contact No. Increased percentage %
100	4.760355	0.0	4.804665	0.0
98	5.756527	20.9	6.05698	26.1
94	5.864372	23.2	6.627593	37.9
88	6.270317	31.7	6.431181	33.9
81	6.189114	30.0	6.635899	38.1

3.5.2 SI's Influence on Average Contact Numbers

Understanding the interactions between particles is paramount in the study of granular materials. The coordination number (CN) effectively characterises the behaviour of granular materials by shedding light on the intricate network of particle interactions. This concept is particularly relevant because these interactions are closely tied to contact points.

As depicted in Figure 4.21, an intriguing pattern emerges when investigating how the CN responds to changes in the SI. What becomes evident is that as the SI fluctuates, the CN remains relatively stable. This observation opens a fascinating window into the behaviour of granular materials. It suggests that altering the SI predominantly triggers variations in three-dimensional particle shapes, with minimal influence on the particles' sphericity. In simpler terms, while SI influences particle size, it does not interfere with the inherent sphericity of the particles. Consequently, the density of particle connections within the assembly remains relatively consistent, as SI variations do not disrupt the SPH index. It is a compelling notion highlighting the unique dynamics at play within granular materials.

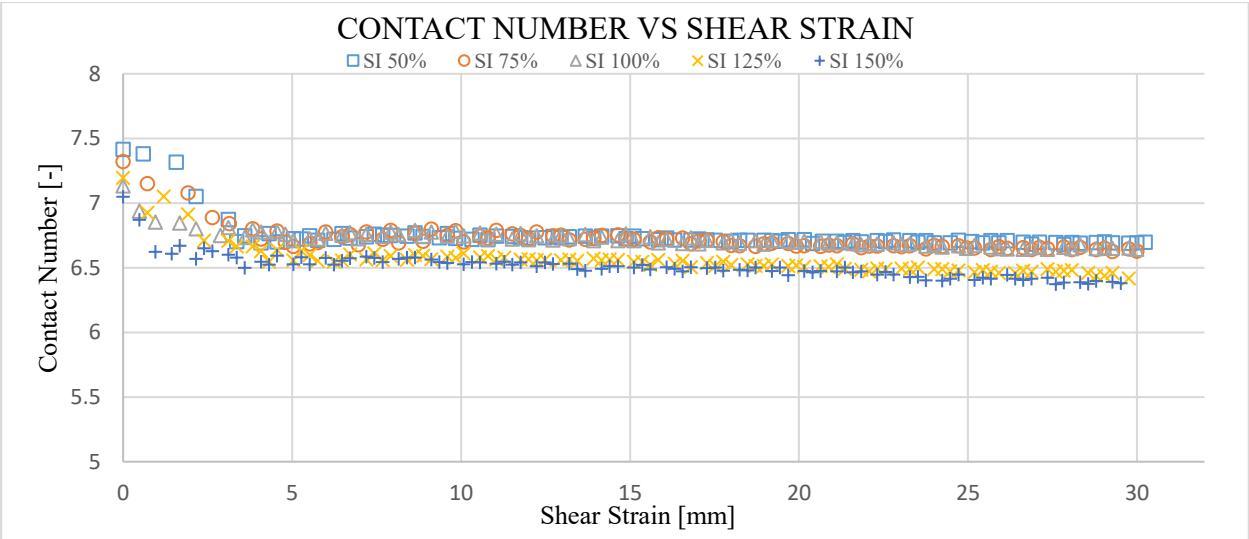

Figure 3.21. Variations of CN versus shear strain for normal stress of 30kPa (SI effect)

Researchers have also weighed on this phenomenon, drawing parallels with particle changes in the Sphericity Index (SPH). They propose that when SPH is altered, it leads to variations in particle shape along a single dimension, effectively elongating the particles. This change promotes increased interlocking among the particles, allowing for more contact points. To encapsulate this, we can conclude that an increase in CN is associated with this condition (Talafha and Oldal, 2021).

Figure 4.22 provides an intriguing perspective on the CN related to SI and stress. It demonstrates that regardless of the SI index, applying high stress to the sample results in a noticeable increase in the CN. However, it is important to note that CN decreases immediately as normal stress levels decrease, primarily attributable to the dilatation effect induced by the initial strain, which signifies granular materials' complex and dynamic nature.

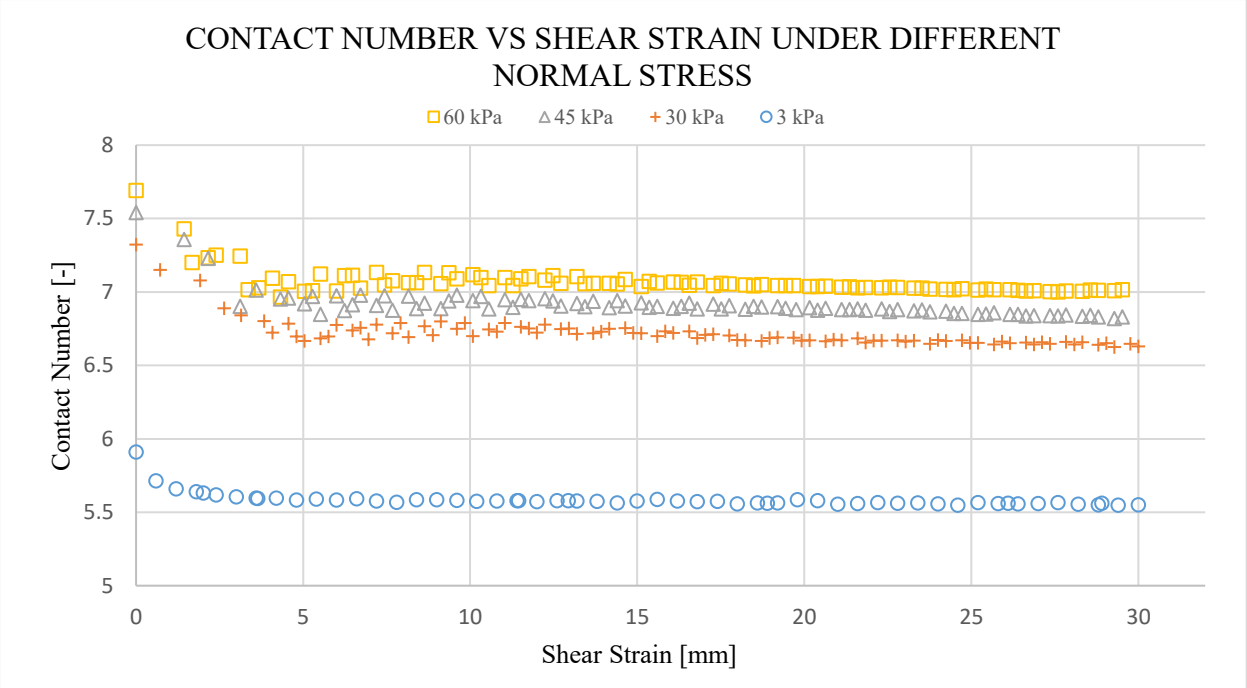

Figure 3.22. Variations of CN versus shear strain for various normal stresses (SI 150%)

This insightful exploration into SI's influence on average contact numbers unveils fascinating complexities within the world of granular materials, shedding light on how variations in SI can significantly impact particle interactions and the coordination number.

3.5.3 TPSI and Average Contact Numbers

Interestingly, a unique pattern emerges concerning the coordination number (CN) when focusing on the Triple Particle Size Index (TPSI). Despite variations in TPSI, CN demonstrates stability, as visually depicted in Figure 4.23. This constancy in CN, even amidst changes in TPSI, can be attributed to the size index (SI), which indicates that alterations in TPSI do not significantly affect the fundamental regularity of the particles. Consequently, the sphericity index retains its constancy across these variations. Researchers have elucidated that modifying the Sphericity Index (SPH) results in a one-dimensional elongation of the particle shape, intensifying interlocking among particles and enhancing the coordination number accordingly.

The calculation of the average contact number involved summing the total number of contacts across all particles within the system and subsequently dividing this sum by the total number of particles. This computation yielded an average value indicative of the typical number of contacts per particle in the system under consideration.

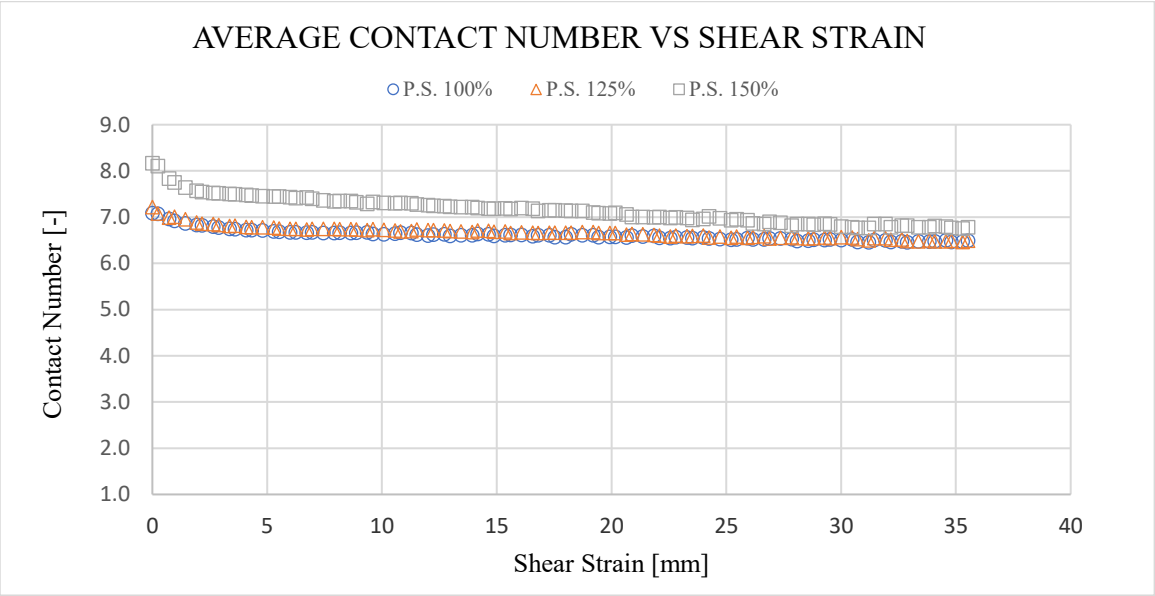

Figure 3.23. Variations of CN versus shear strain for normal stress of 8 kPa (SI effect).

Furthermore, as the previous finding mentions regarding the SI and the SPH, a notable increase in CN is observed when subjecting the sample to high stress, regardless of the specific TPSI index, as depicted in Figure 4.24. It emphasised the significant role of stress in augmenting the connections among particles within the granular assembly. However, it is essential to note that initial strain induces an immediate decline in CN at lower normal stress levels due to pronounced dilatation. This rapid decrease in CN underscores the intricate interplay between shear stress, dilatation effects, and contact numbers within granular materials.

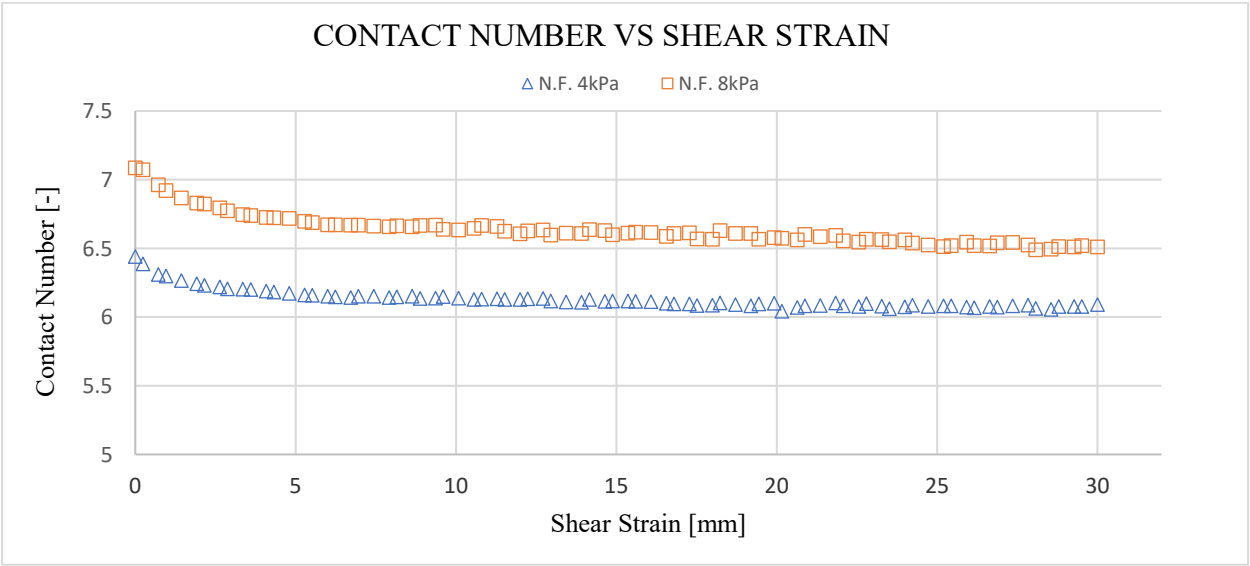

Figure 3.24. Variations of CN versus shear strain with various normal stresses 4kPa and 8kPa for a sample of (SI = 100%).

This analysis of TPSI's influence on average contact numbers reveals a nuanced interconnection between particle shape, interlocking dynamics, and the impact of shear stress. These findings contribute to a deeper understanding of the intricate behaviours exhibited by granular materials under varying conditions, laying a robust foundation for further exploration and analysis.

3.5.4 Variation in Average Contact Numbers with Shape Indexes

In the investigation of granular materials, the Average Contact Number (CN) is a crucial metric, representing the average number of particles in contact within the assembly. As we delve into the nuances of particle shape defined by the Shape Indexes (SPH, SI, and TPSI), a coherent pattern emerges regarding CN.

SPH's Effect on Average Contact Numbers

1. Decreasing SPH leads to a continuous increase in CN.
2. The relationship between CN and SPH is inverse, as shown in previous research on elliptical particles.
3. High stress consistently results in a higher CN regardless of the SPH index.
4. CN decreases with reduced normal stress levels due to the initial strain-induced dilatation effect.
5. The complex interplay between normal stress, dilation, and contact numbers is highlighted.

SI's Influence on Average Contact Numbers

1. CN remains stable even as the Size Index (SI) fluctuates, indicating consistency in particle connections.
2. SI changes affect particle shapes, not inherent sphericity, maintaining the stable density of particle connections within the assembly.
3. High stress increases CN regardless of the SI index, promoting more contact points among particles.
4. CN decreases with reduced normal stress levels due to the initial strain-induced dilatation effect, highlighting the complex nature of granular materials.

TPSI and Average Contact Numbers

1. CN remains stable despite changes in the Triple Particle Size Index (TPSI), as shown in Figure 4.23.
2. Alterations in TPSI do not disrupt the fundamental sphericity of particles, maintaining particle shape.
3. Maintaining particle shape ensures an unchanged density of connections between particles within the assembly.
4. Figure 4.24 shows that higher stress increases the CN regarding the TPSI value, emphasising stress's role in augmenting particle connections.

Summary

this study investigates the impact of varied factors, including TPSI, SI, and SPH, on average contact numbers (CN) in granular materials. For TPSI and SI, a stable relationship with CN is observed, indicating their predominant influence on particle shape and stability. However, high Stress significantly increases CN irrespective of SPH, TPSI or SI. Additionally, the study introduces a novel finding regarding SPH, noting an inverse relationship with CN that challenges existing theories, emphasising the need for further exploration into the complex interactions between particle shape, interlocking, and contact behaviour in granular materials.

3.6 Contact Force Chain Analysis

3.6.1 SPH Impact on Contact Force Chain Formation

Contact force chain analysis is pivotal in understanding the behaviour of granular materials under different stress conditions. In this section, we delve into the influence of the SPH on the formation of contact force chains. These force distributions for different SPH values under continuous normal stress at distinct phases of a direct shear test are shown in Figures 4.25 and 4.26.

The figure particles' colour signifies the intensity of the contact forces, with red, green, and blue particles representing high, moderate, and low forces within the assembly. Initially, before shear loading (at a strain of 0%), contact forces are uniformly distributed within the shear container regardless of particle shape.

However, as shear force is applied and the material undergoes deformation, we observe a stark contrast between 0% and 15% strain in contact force chains. During the shearing process, the initial stage Figure 4.25 exhibits a thicker contact chain than the shearing stage Figure 4.26. This phenomenon is linked to the dilation behaviour of granular samples during shear, reducing the number of contacts.

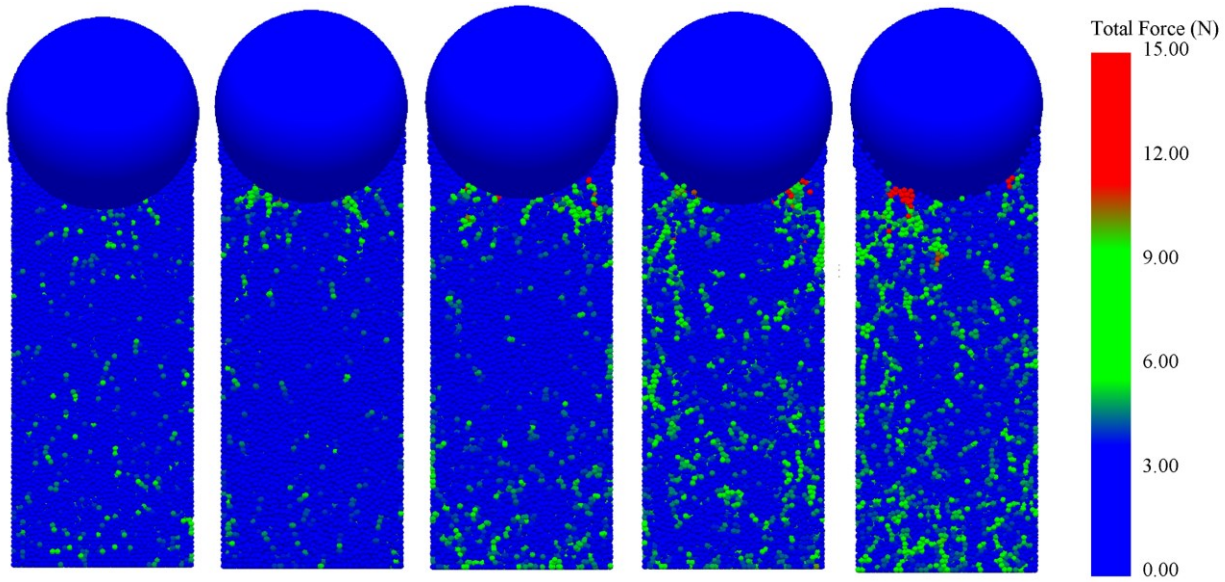

Figure 3.25. Contact force chain distribution for different particle sphericity at the shear strain of 0% and 15N normal load (Particles SPH= 100%, 98%, 94%, 88%, 81%, respectively)

Remarkably, as the material shears, an increased number of contacts is oriented in directions bearing higher loads, primarily in the shear direction, leading to higher magnitudes of the associated contact forces. Additionally, it is noteworthy that samples with lower sphericity values manifest higher shear forces in the shear stage. This occurrence is closely tied to improved interlocking in assemblies with lower sphericity values, leading to elevated contact numbers and their magnitudes in the shear direction.

These findings align with earlier observations by (Yang et al., 2016), underscoring that force chains in samples with lower sphericity contribute more significantly to the assembly's overall contacts. Consequently, this structural rearrangement leads to the formation of a shear band that traverses the upper left to the lower right of the shear box. This ensures effective load transfer within the samples, resulting in a more stable structure for force chains.

Conversely, particles positioned away from the shear band exhibit minimal participation in bearing the applied load. This unique insight into the impact of SPH on contact force chains provides a valuable perspective on the behaviour of granular materials under shear. It sheds light on the intricate interplay between particle shape and force distribution.

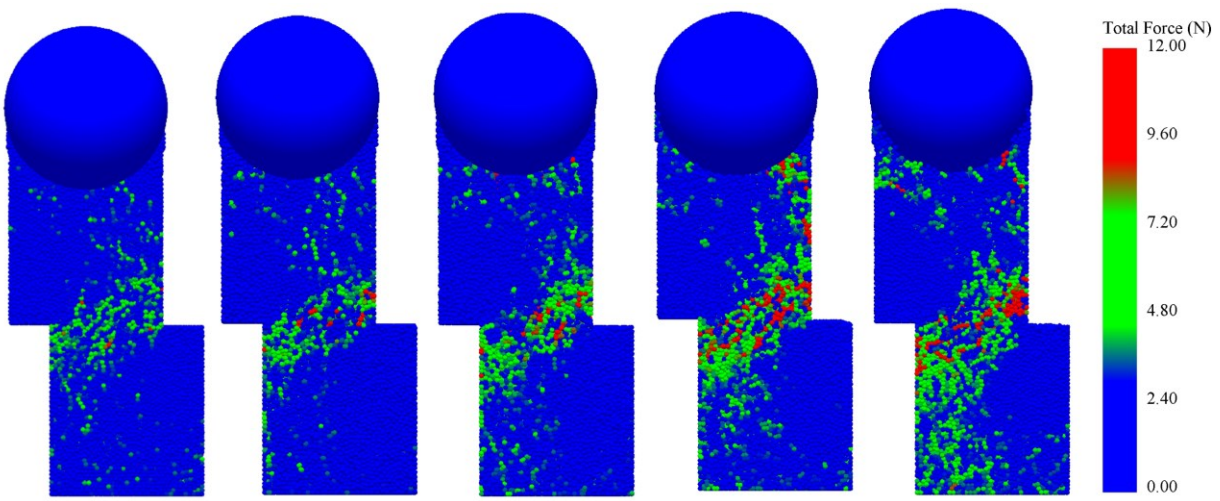

Figure 3.26. Contact force chain distribution for different particle sphericity at the shear strain of 15% and 15N normal load (Particles SPH= 100%, 98%, 94%, 88%, 81%, respectively)

3.6.2 SI's Influence on Contact Force Chains

In our analysis of contact force chains, we examined the force distribution within the model at various stages of the SST, focusing on different SI values and normal stresses. Figures 4.27 and 4.24 offer a comprehensive view, highlighting inter-particle and particle-wall forces in different shades: red denotes high contact forces, green represents moderate forces, and blue indicates low forces.

At the initial stage, before applying shear stress (0% strain), particles in the model displayed a uniform distribution, irrespective of SI values. However, as shear forces were applied, significant variations in contact force chains emerged, notably between 0% and 15% strain. Figure 4.27 depicts a denser contact force chain during the first stage (0% strain), attributed to particle dilation behaviour induced by shear, leading to decreased particle CN.

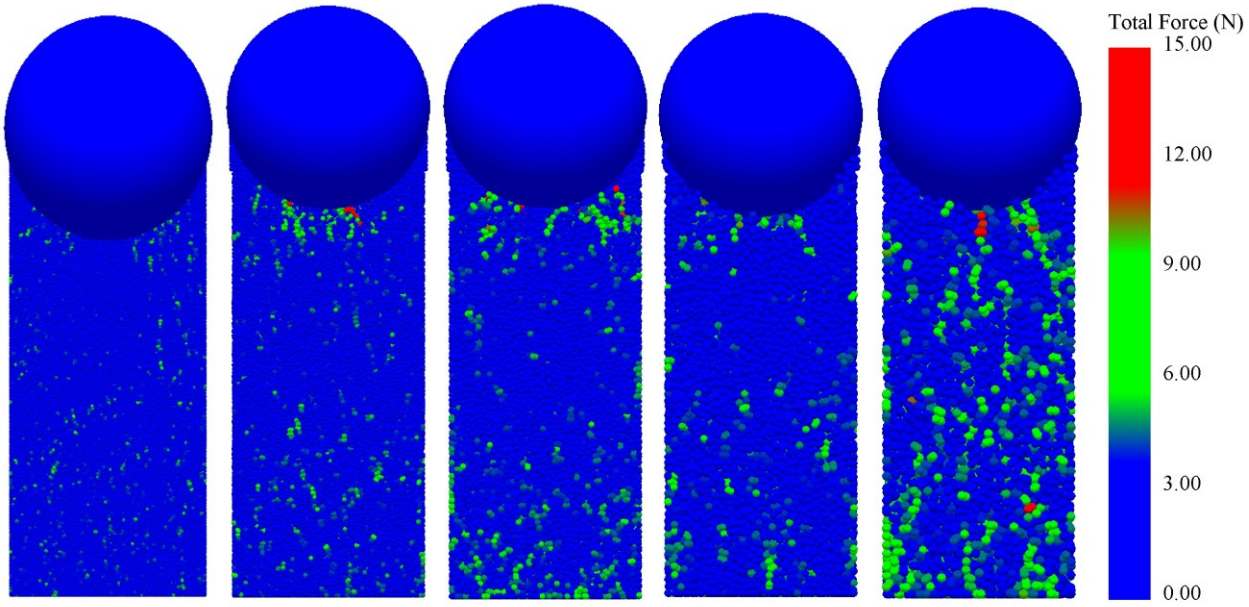

Figure 3.27. Contact force chain distribution for different size index particles at the shear strain of 0% and 15N normal load (Size index SI= 50%, 75%, 100%, 125%, 150%, respectively)

During the shearing process, particles' CN aligned with the direction of higher loads, precisely the shear direction. Gradually applying the shearing forces reduces the interaction cross-sectional area

between the two cylinders, leading to a decline in shear stress. Notably, samples with higher SI values exhibited increased shear forces during the shearing stage due to interaction contact area, indicating better interlocking as SI values increased.

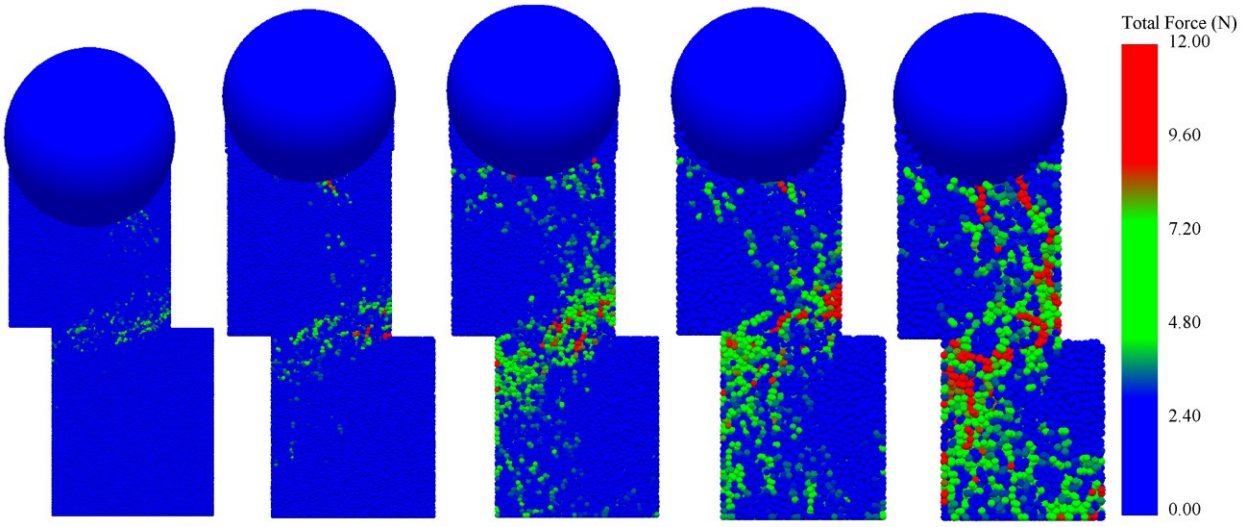

Figure 3.28. Contact force chain distribution for different size index particles at the shear strain of 15% and 15N normal load (Size index SI= 50%, 75%, 100%, 125%, 150%, respectively)

This observation aligns with a related study, which found that higher force chains in higher SI samples led to more significant particle contacts (Yang et al., 2016). As the lower cylinder initiated movement to apply shearing stress, a shear band formed from the bottom left of the lower cylinder to the top right of the upper cylinder. This shear band efficiently distributed most of the load within the assembly, establishing a stable force chain structure. Consequently, particles outside the shear band did not actively participate in bearing the load, as illustrated in Figure 4.28.

3.6.3 TPSI and Contact Force Chain

This section delves into the intriguing interplay between the Triple Particle Size Index (TPSI) and the contact force chains within granular materials. Our investigation, guided by the insights from Figures 4.29 and 4.30, unveils the intricate forces that shape these materials' behaviour under the influence of TPSI.

Figures 4.29 and 4.30, which accurately detail our observations, lay the foundation for our understanding. These visual aids showcase the distributions of inter-particle and particle-wall forces in granular assemblies with varying TPSI values. To aid in interpretation, we have employed a colour scheme: red, green, and blue particles correspond to strong, moderate, and low forces, respectively.

Before beginning shear loading at an original strain of 0%, we observed that contact forces were uniformly distributed throughout the granular medium. Interactions exhibited a harmonious equilibrium within the shear container regardless of the particle shape. However, as we initiated the shearing process, introducing a strain of 15%, the landscape of contact force chains underwent a dramatic transformation compared to its dormant state at a strain of 0%.

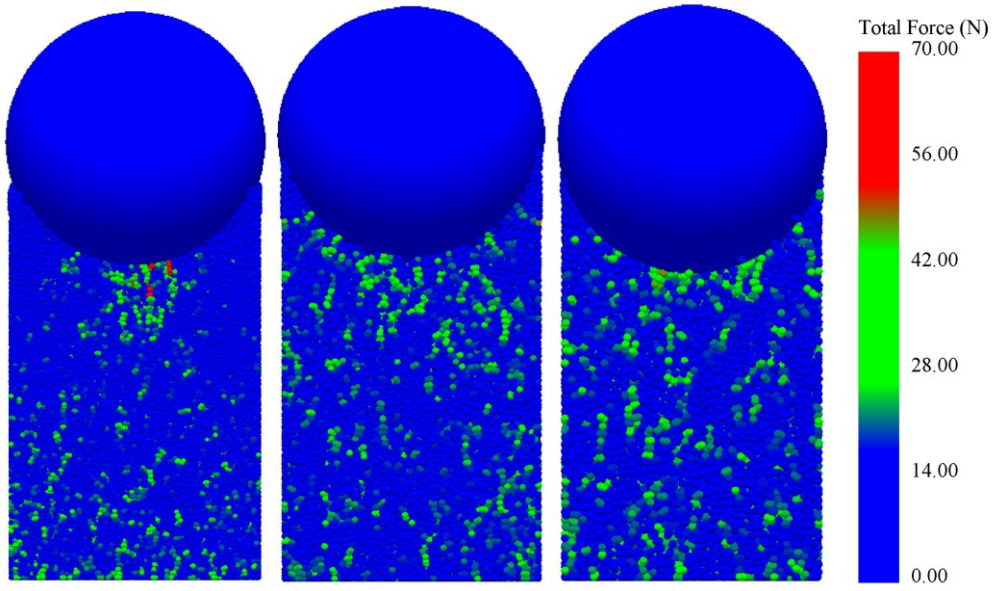

Figure 3.29. Contact force chain distribution for different size index particles at the shear strain of 0% and 70N normal load (Size index SI= 100%, 125%, 150% respectively)

The initial stage, illustrated in Figure 4.29, revealed a robust contact chain network. This thicker web of contact forces can be attributed to the particles' dilation behaviour during shear, which inherently reduces the number of interactions. Shear stress is progressively applied, as represented by Figure 4.30.

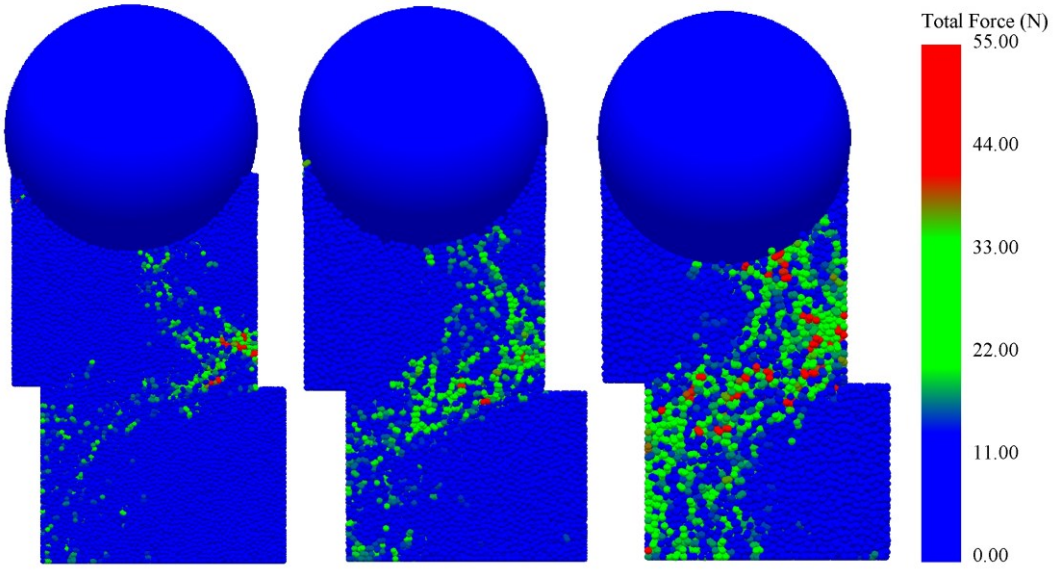

Figure 3.30. Contact force chain distribution for different size index particles at the shear strain of 15% and 70N normal load (Size index SI= 100%, 125%, 150% respectively)

In the shear stage, we noticed a marked difference in contact forces. These forces were not only oriented in the direction of higher loads, which aligns with the direction of shear, but we also observed a decrease in shear forces due to the reduction of the contact area. It became evident that samples with a higher TPSI demonstrated a more substantial shear force during this stage. This observation can be linked to the enhanced rough interlocking behaviour that emerges as TPSI values increase. Consequently, assemblies with higher TPSI values exhibited greater strength, a phenomenon that can be attributed to the concentration of forces around the vertical walls of the top shear cylinder.

These findings align with previous research (Yang et al., 2016), reinforcing that robust force chains form a more substantial portion of assembly contacts in granular samples with higher TPSI values. This structural rearrangement significantly impacts the formation of shear bands extending from the top right to the bottom left of the shear cylinder, facilitating effective load transmission within the granular material. This results in a more stable architecture for force chains. However, particles located outside of the shear band have minimal involvement in bearing the applied load.

3.6.4 Contact Force Chain Patterns in Different Shape Indexes

The study investigated the influence of sphericity index (SPH), size index (SI), and triple particle size index (TPSI) on contact force chains in granular materials. The results showed that:

SPH Impact on Contact Force Chain Formation

Contact forces were observed to vary with changes in SPH values.

1. Higher SPH values and a more robust contact force chain network increased contact forces.
2. Assemblies with lower SPH values exhibited a concentration of force near the upper shear cylinder vertical walls, promoting effective load transmission.
3. Shear bands formed entirely from the shear box's upper right to the lower left.
4. At 0% strain, contact force chains are uniformly distributed.
5. As the material shears, contact force chains become thicker and more concentrated in the shear direction.
6. Samples with lower sphericity values exhibit higher shear forces in the shear stage.

SI's Influence on Contact Force Chains

Contact forces were significantly affected by changes in Size Index (SI).

1. Samples with a higher SI demonstrated more substantial shear forces during shearing due to enhanced interlocking contact area.
2. The concentration of forces around the top shear cylinder's vertical walls in higher SI samples played a critical role in load transmission.
3. Force chains in higher SI samples formed more extensive assembly contacts.
4. At 0% strain, contact force chains are uniformly distributed.
5. As the material shears, contact force chains become thicker and more concentrated in the shear direction.

TPSI and Contact Force Chain Dynamics

TPSI values were linked to the dynamics of contact force chains.

1. Enhanced rough interlocking as TPSI values increased contributed to higher shear forces.
2. Samples with higher TPSI values demonstrated greater strength and a more stable structure for force chains.
3. Strong force chains in higher TPSI samples formed a more substantial portion of the assembly contacts, influencing the formation of shear bands.
4. These points encapsulate the relationship between different shape indexes and the patterns of contact force chains within granular materials under shear stress.

Summary

These findings suggest that SPH, SI, and TPSI play a role in the formation and behaviour of contact force chains in granular materials. Lower sphericity, higher SI, and higher TPSI values tend to lead to thicker and more concentrated contact force chains with higher shear forces. These findings have implications for the design of granular materials for applications such as construction.

3.7 Shear Zone and Particle Rotation Examination

3.7.1 SPH's Influence on Shear Zone Formation

Particle rotation is a fundamental method for assessing the formation of shear bands within granular assemblies under loading conditions (Oda and Kazama, 1998; Mahmood and Iwashita, 2011). While a direct shear test can provide insights into shear band formation, it is crucial to delve deeper into the influence of non-rounded particles compared to their rounded counterparts, explicitly concerning the positions and thickness of these shear bands. This nuanced analysis has been a focal point of our research, leading to Figure 4.31.

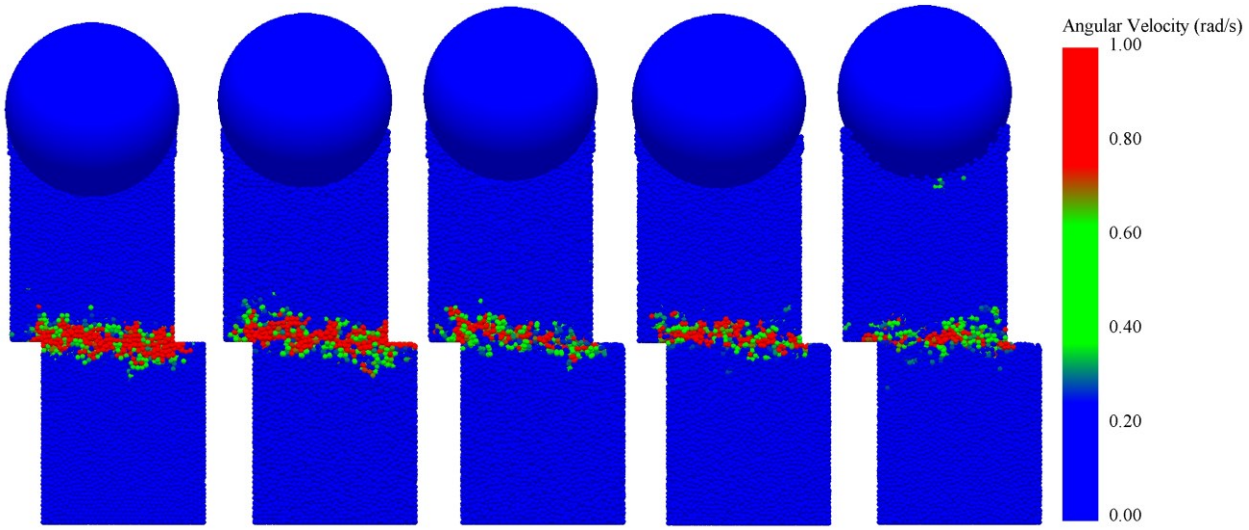

Figure 3.31. (Particle rotation at a shear strain of 15% and 15N normal load for SPH= 100%, 98%, 94%, 88%, 81%, respectively)

Figure 4.31 depicts the accumulated particle rotation within the sample at a strain of 15% under a normal load of 15N. The colours in the figure correspond to the rotations, where red indicates a higher average rotation, green indicates moderate rotation, and blue represents low rotation. Figure 4.31 illustrates where particles with higher rotations occur among rounded and non-rounded particles. Notably, non-rounded particles, especially those with an SPH of 81%, exhibit lower average accumulation rotation when compared to their spherical counterparts. This phenomenon is a direct result of increased interlocking among these particles. For instance, if the particle transitions from a spherical SPH of 100% to an elongated SPH of 81%, it results in a 40% reduction in the overall average particle rotation.

Figure 4.31 further substantiates these findings by depicting the distribution of the rounded particle rotation. The rounded particles exhibit a more uniform rotation distribution with a broader shear band encircling the shearing plane. Conversely, the sample with SPH 81% displays a higher degree of rotation but within a narrower shear band concentrated near the shearing plane. This intriguing observation underscores a critical trend: as shear strength increases, the width of the rotation zone and the average particle rotation concomitantly decrease (Danesh et al., 2020).

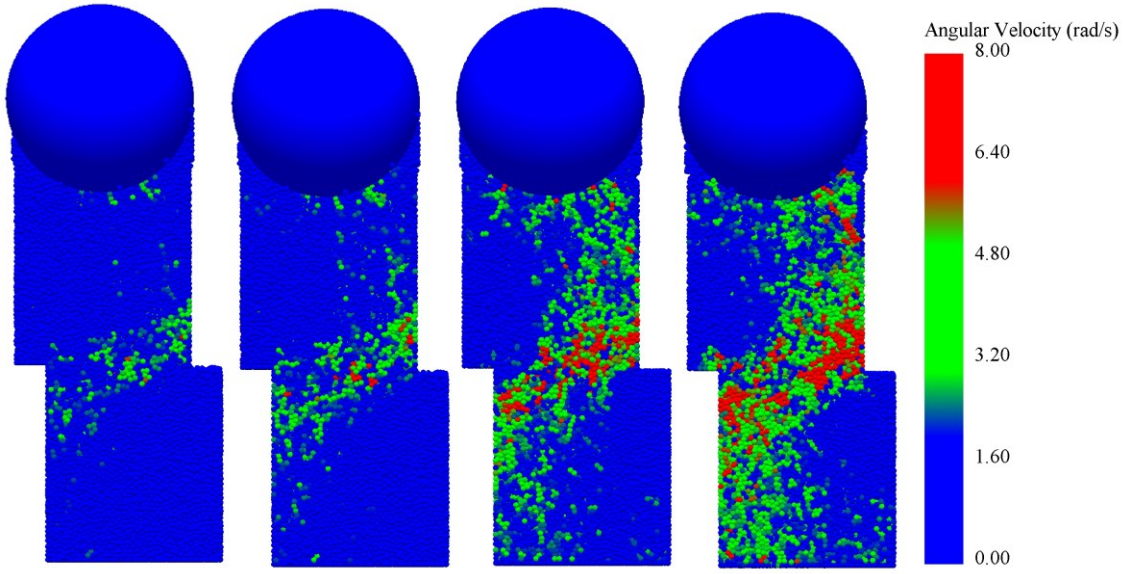

Figure 3.32. Particle rotation at the shear strain of 15% for the SPH = 81% at (different normal stress = 25 kPa, 50 kPa, 75 kPa, 100 kPa, respectively)

Understanding the movement behaviour of particles is pivotal. It can be conceptualised as layers of particles moving on top of one another. Two key factors influence this movement. To begin with, the interlocking between particles, as illustrated in Figures 4.30 and 4.31, plays a pivotal role in particle rotation. Furthermore, the normal stress, which enhances friction between particles due to improved particle interlocking, increases rotation interaction. The intriguing correlation between the particle rotation pattern and the distribution of forces within the particles results from rearrangements, as depicted in Figure 4.32; these rearrangements cause the shear band to form entirely from the upper right to the lower left of the shear cylinder. This structural arrangement ensures superior load transfer within the samples, creating a stable force chain structure. Particles outside the shear band do not actively carry the load, emphasising the significance of this intricate interplay between rotation, interlocking, and normal forces in understanding shear zone dynamics.

3.7.2 SI's Impact on Shear Zone and Particle Rotation

Particle rotation is fundamental in exploring shear bands within granular assemblies during loading. While the SST can offer insights into shear band formation, a more nuanced analysis of the particle SI is essential concerning the shear band's position and average angular velocity. This meticulous consideration has been a critical focus of our research, as depicted in Figure 4.33.

Figure 4.33 presents the cumulative particle rotations within the sample subjected to a 15% strain under normal stress of 30 kPa. The colour scheme denotes rotation magnitude, with red indicating high rotations, green moderate rotations, and blue low rotations. Notably, both small and large particles exhibit localised rotations. Interestingly, large particles with SI = 150% display a lower average cumulative rotation than small particles with SI = 50%. This observation aligns with the increased contact area between particles as SI increases, resulting in a higher frictional force. Quantitatively, the transition from SI = 50% to SI = 150% corresponds to a 66% reduction in the overall average particle rotation.

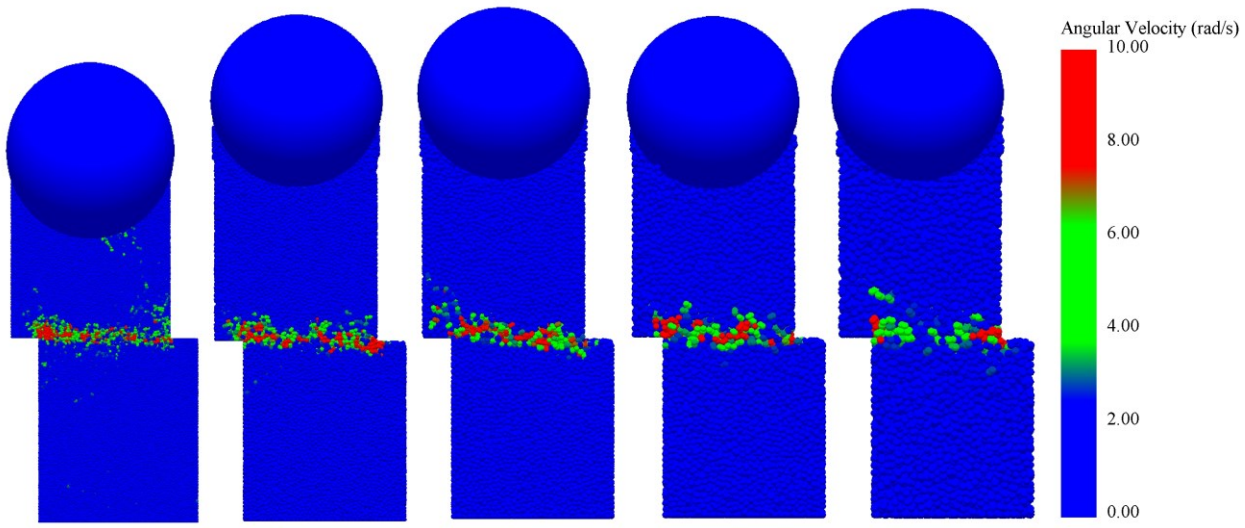

Figure 3.33. Particle rotation at the shear strain of 15% for (SI= 150%, 125%, 100%, 75%, and 50%, respectively) at 30kPa, normal stress

Figure 4.34 provides additional insights, presenting the average angular velocity for particles of various SI. It becomes evident that the increase in shear strength, attributed to higher SI values, corresponds with a decrease in the particle's average rotation.

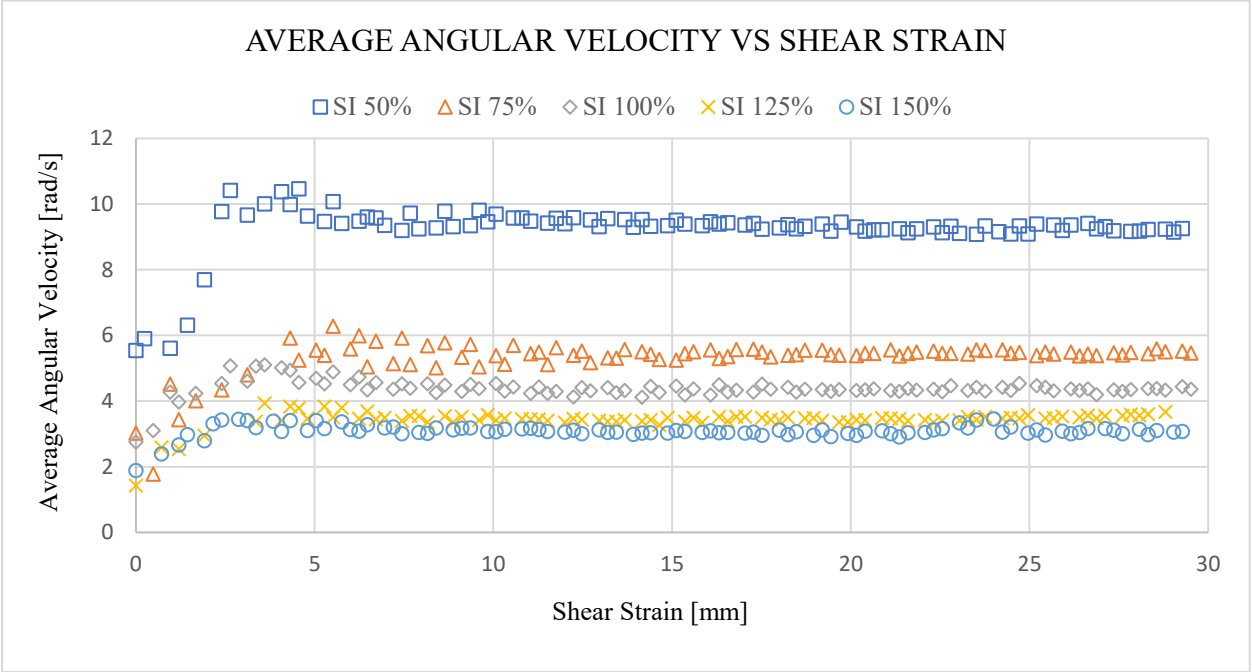

Figure 3.34. Average angular velocity for different size index particles under 30kPa normal stress

The movement dynamics of the particles are similar to layers shifting atop each other, a phenomenon illustrated in Figure 4.35. This rotational behaviour is intricately connected to two key factors: normal stress and particle interlocking. An increase in the normal load augments friction between particles due to enhanced locking, subsequently intensifying rotation interactions. This intricate relationship between rotation, interlocking, and normal loads is highlighted in the rotational patterns observed in Figures 4.33- 4.35. Rearrangements within the assembly cause the shear band to form entirely from the upper right to the lower left of the shear cylinder. This structural configuration ensures superior load transfer within the samples, emphasising the critical role of SI in shaping shear zone structures and dynamics.

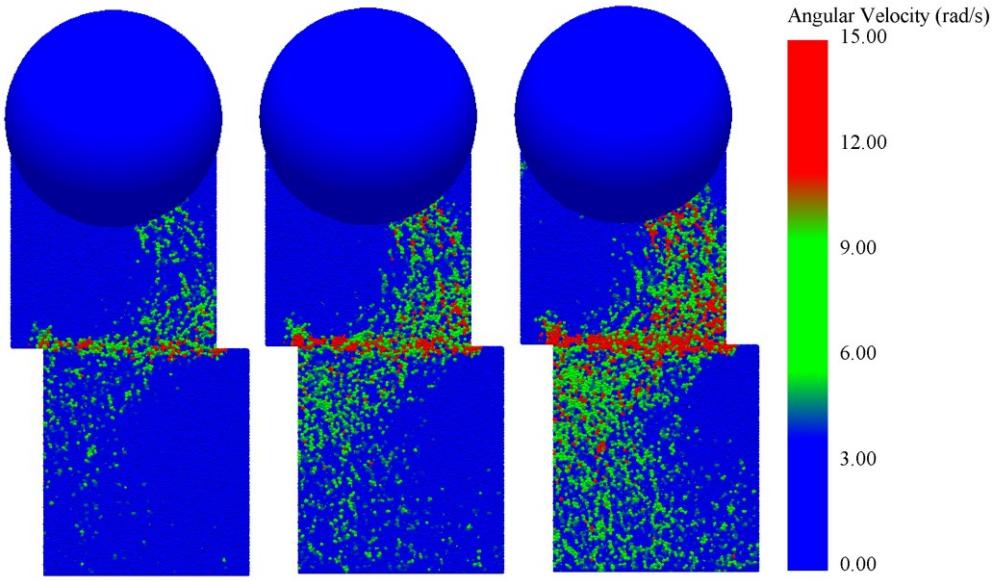

Figure 3.35. Particle rotation at the shear strain of 15% for the test of SI 75% at different normal stress = 30 kPa, 45 kPa, 60 kPa, respectively

3.7.3 TPSI and Shear Zone Behaviour

In granular assemblies' shear bands, particle rotation is a fundamental assessment tool during loading processes. While the SST can provide valuable data about shear band formation, an in-depth analysis of the TPSI is crucial, especially concerning the shear band's position and the average angular velocity. This nuanced perspective has been a focal point of our study, as highlighted in Figure 4.36.

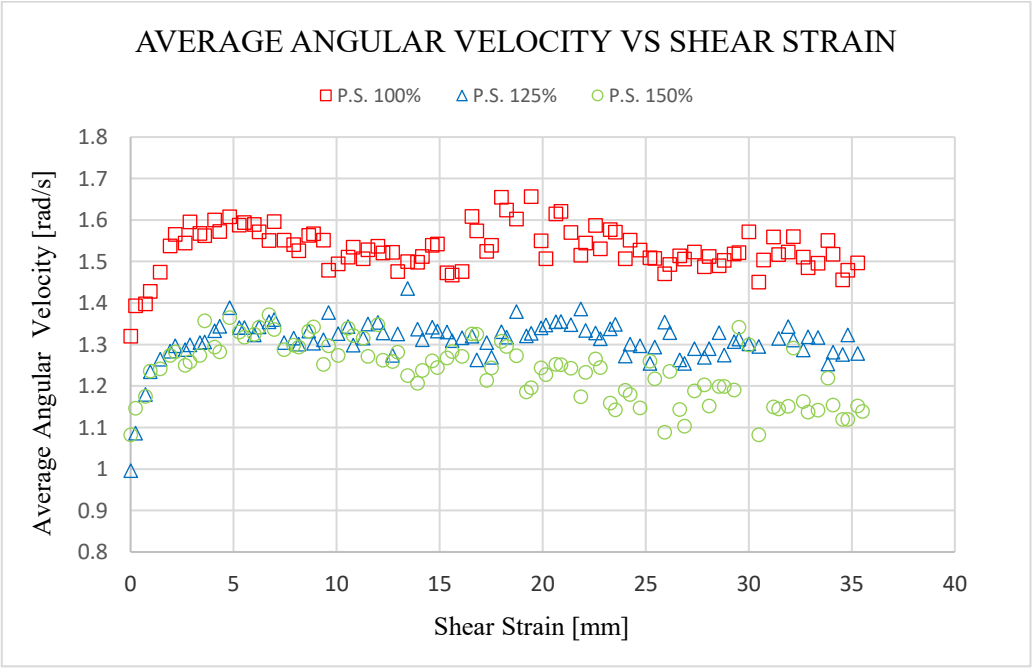

Figure 3.36. Average angular velocity for different size index particles under 8kPa normal stress

Figure 4.36 portrays the average angular velocity of particles in the sample, showcasing variations between small and large particles. Intriguingly, large particles with TPSI=150% exhibit lower average accumulation rotation than smaller counterparts with TPSI=100%. This trend aligns with the increase in interlocking among particles as TPSI escalates. For instance, as the particles

transition from TPSI=100% to TPSI=150%, a notable 24% reduction in the overall average particle rotation results.

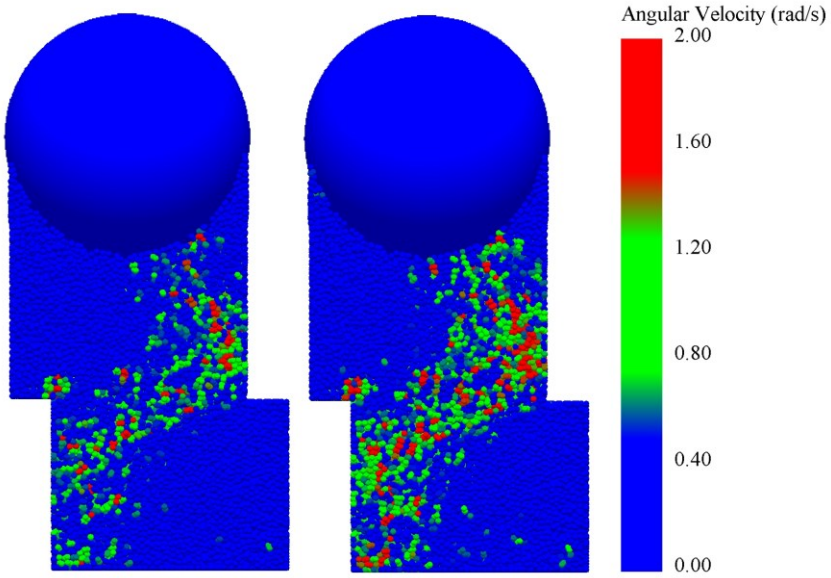

Figure 3.37. Particle rotation at the shear strain of 15% for the test of TPSI 100% at different normal stresses = 4 kPa, 8 kPa, respectively

Furthermore, this reduction in particle rotation corresponds with increased shear strength due to elevated TPSI values. This rotational behaviour is intricately connected to two key factors: the expected load and particle interlocking. An increase in the normal load augments friction between particles due to enhanced locking, subsequently intensifying rotation interactions.

Crucially, the rotation pattern mirrors the distribution of forces within the particles, a phenomenon emphasised in Figure 4.37. The rearrangements within the assembly lead to the shear band forming entirely from the upper right to the lower left of the shear cylinder. This specific structural configuration ensures a superior load transfer within the samples, underscoring the pivotal role of TPSI in shaping shear zone behaviour and dynamics.

3.7.4 Shear Zone and Particle Rotation under Various Shape Indexes

The study investigated the influence of SI, TPSI, and SPH on particle rotation and shear zone formation in granular materials. The results showed that:

SPH's Influence on Shear Zone Formation

1. Particle rotation is used to evaluate shear band formation.
2. Non-rounded particles showed lower average rotation, especially at SPH 81%.
3. Change in sphericity from SPH 100% to SPH 81% reduced average particle rotation by 40%.
4. The rotation pattern followed the force distribution, forming stable shear bands.
5. Non-rounded particles exhibit lower average accumulation rotation than rounded particles.
6. An increase in shear strength is accompanied by a reduction in the rotation zone width and average particle rotation.
7. The movement behaviour of particles is like layers shifting atop each other.
8. An increase in the normal force augments friction between particles due to enhanced locking, subsequently intensifying rotation interactions.

SI's Impact on Shear Zone Structure

1. Particle rotation is used to assess shear bands.
2. High SI particles exhibit lower average rotation due to the increased area of the contact points, interlocking, and effective stress transfer area.
3. Changing from SI=50% to SI=150% reduced overall particle rotation by 66%.
4. Shear band formation followed rearrangement, providing superior load transfer.
5. An increase in normal stress augments rotation interactions among particles.

TPSI and Shear Zone Behaviour

1. Higher TPSI (TPSI=150%) reduced average particle rotation by 24%.
2. Particle rotation is influenced by normal stress and particle interlocking, leading to enhanced friction and ensuring effective load transfer.
3. The rotation pattern is aligned with force distribution, ensuring effective load transfer.
4. A lower average accumulation rotation occurred with Larger particles of TPSI=150% compared to smaller counterparts with TPSI=100%.
5. This reduction in particle rotation corresponds with increased shear strength due to elevated TPSI values.

Summary

These findings suggest that SPH, SI, and TPSI all play a role in the formation of shear zones and the movement of particles in granular materials. Lower SPH, higher SI, and higher TPSI values all tend to lead to a lower average particle rotation, indicating that these factors contribute to forming more robust and stable shear zones. These findings have implications for the design of granular materials for applications such as construction and mining.

3.8 The Combined Effect of Normal Stress and Mechanical Vibration on Wheat Packing Density

3.8.1 Intensity Effect of the Applied Parameters

The influence of vibration period on data collection precision and efficiency concerning packing density has been investigated unless otherwise specified. Figure 4.38 presents the changes in wheat packing density as a function of vibration time, considering various vibration amplitudes and normal stresses. Several phenomena are observed. The wheat packing density initially exhibits a similar trend across all tests, characterised by an initial increase followed by a stabilisation at the highest packing density. In the freeloaded test, the packing density shows rapid growth until t = 3s, after which it reaches a stable value. In contrast, the loaded packing density test experiences faster growth until t = 2s, which is attributed to the effect of normal stress. Subsequently, a consistent packing density value is observed for all test conditions, with no further increase.

As illustrated in Figure 4.38a, the freeloading test revealed alignment only in the first two test lines. Suggests that the impact of vibration amplitude becomes significant only after exceeding a specific threshold. Conversely, the loaded test, Figure 4.38b, demonstrated a persistent influence of vibration amplitude regardless of its value. This disparity arises from the contrasting mechanisms of particle rearrangement in each test. Under freeloading, gravitational forces naturally induce particle rearrangement. In contrast, the loaded test involves externally applied normal stress, facilitating efficient vibration energy transfer and enhanced particle rearrangement due to improved particle interaction.

Consequently, even at lower vibration amplitudes, loaded tests exhibit a sequential reduction in particle voids, thereby influencing packing density. Furthermore, a vibration duration of 10 seconds was sufficient for generating stable and densely packed structures. This observation informed the selection of a 10-second vibration time for subsequent experiments.

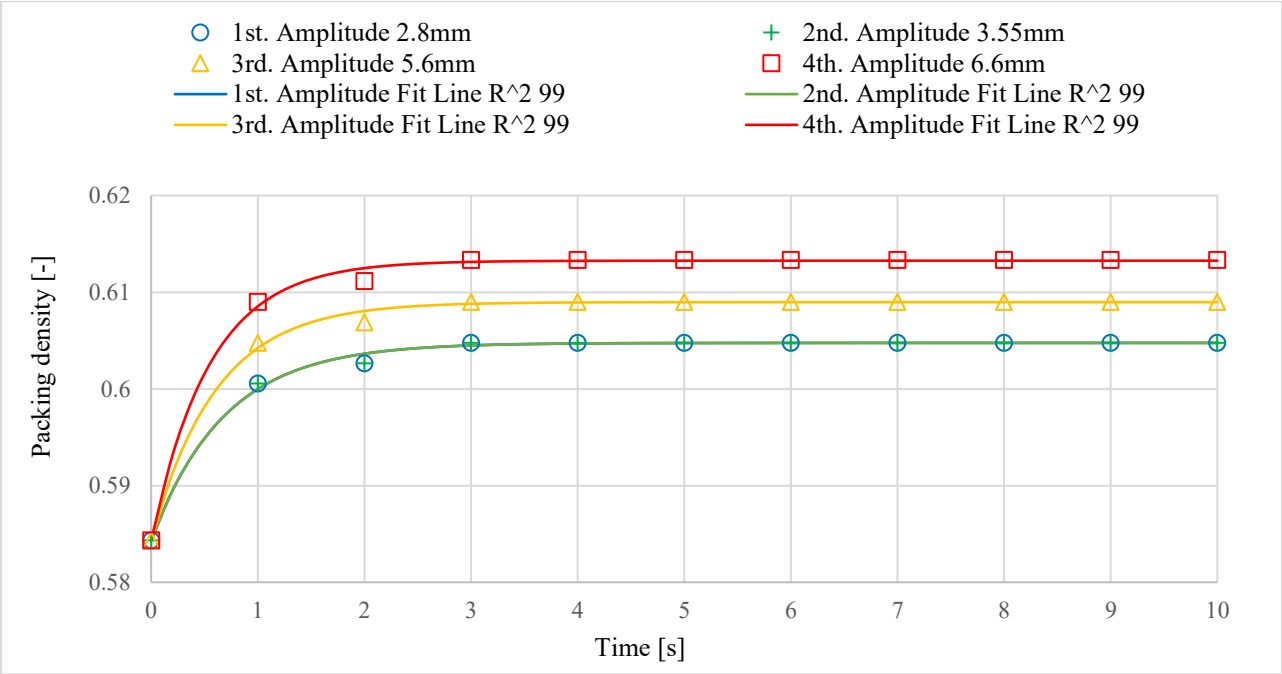

(a)

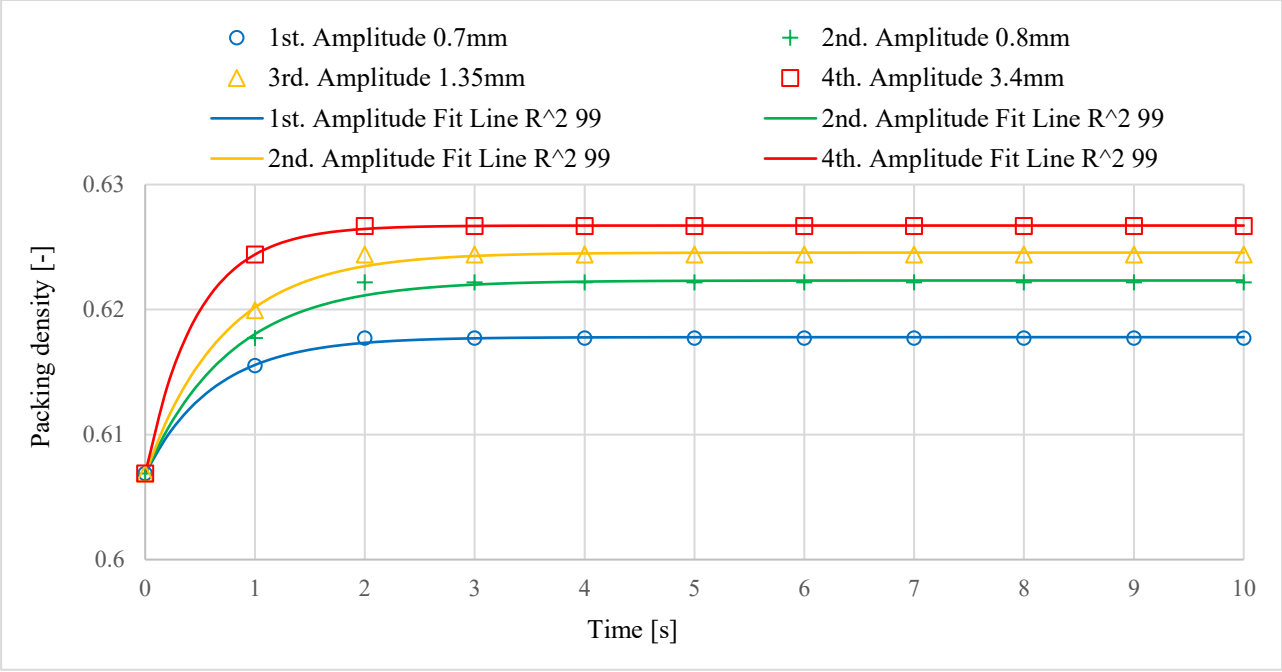

(b)

Figure 3.38. (a) Wheat packing density ρ vs. vibration time t for the freeload test (b) Wheat packing density ρ vs. vibration time t for the test 42.3kPa

Notably, the packing density and vibration time profiles conform with the exponential equation initially proposed for investigating the densification behaviour of monodisperse spherical glass particles (Knight et al., 1995). Subsequently, researchers expanded its applicability by attributing physical significance to equation 4.5 to describe the packing density of PMMA cylinder-sphere mixtures (Zhao et al., 2019). Therefore, the exponential equation 4.6 is employed to elucidate the packing density of wheat particles in the current study.

$$\rho_{(t)} = \left(\rho_i - \rho_f\right) \mathrm{e}^{-(t/\tau)} + \rho_f \quad \text{(Zhao et al., 2019)} \qquad 3.5)$$

The time-varying particle packing density, denoted as $\rho_{(t)}$[-], is characterised by the initial packing density ρ_i [-] and the final packing density ρ_f [-]. The vibration time is denoted as t [s], and the characteristic time of the process is represented as τ [s]. The parameter values for the fitted equations at t = 10 s are presented in Table 4.8. Moreover, the conclusion drawn from the study indicates that the evolution of freeloaded packing density reaches near completion after 3 s (i.e., t = 5 s). The loaded packing density evolution is nearly complete after 2 s (i.e., t = 3 s), consistent with the observation that the experimental function lines exhibit characteristic times of approximately 0.6 s.

Table 3.8. The exponential Equation 4.6 fitted parameters.

Unloaded test	$\boldsymbol{\rho_i}$	$\boldsymbol{\rho_f}$	**τ**	**Loaded test 42 kPa**	$\boldsymbol{\rho_i}$	$\boldsymbol{\rho_f}$	**τ**
1st Amp.	0.58434	0.60477	0.69	1st Amp.	0.60689	0.61774	0.63
2nd Amp.	0.58434	0.60477	0.69	2nd Amp.	0.60689	0.62218	0.78
3rd Amp.	0.58434	0.60903	0.61	3rd Amp.	0.60689	0.62443	0.72
4th Amp.	0.58434	0.61335	0.55	4th Amp.	0.60689	0.62669	0.47

3.8.2 Effects of Vibration Amplitude and Normal Stress

Figures 4.39a and b demonstrate the significant influence of vibration amplitude (A) and normal stress (σ) on wheat packing density (ρ). The initial state of wheat packing density is represented by Figure 4.39a, which reflects the condition by applying solely the normal stress to the wheat particles, demonstrating that a Higher wheat packing density can be achieved by using only normal stress. By curryon, figure 4.39b represents the wheat packing density under the influence of the vibration amplitude. Furthermore, a clear correlation exists between wheat packing density and vibration amplitude; an increase in amplitude leads to a subsequent rise in wheat ρ. Figures 4.39a and b also reveal that the maximum wheat packing density is attained by applying maximum vibration amplitude. However, a lower vibration amplitude is needed in the loaded test to achieve the maximum value of wheat ρ compared to the freeloaded test. The continuous increase in wheat packing density with rising vibration amplitude is due to the gradual delivery of energy, which densifies the initial loose structures by filling the voids within the packing. Consequently, the packing structure accumulates enough energy to facilitate ultimate particle rearrangement, enabling small wheat particles to fill the spaces between large wheat particles and enhance wheat ρ during this phase.

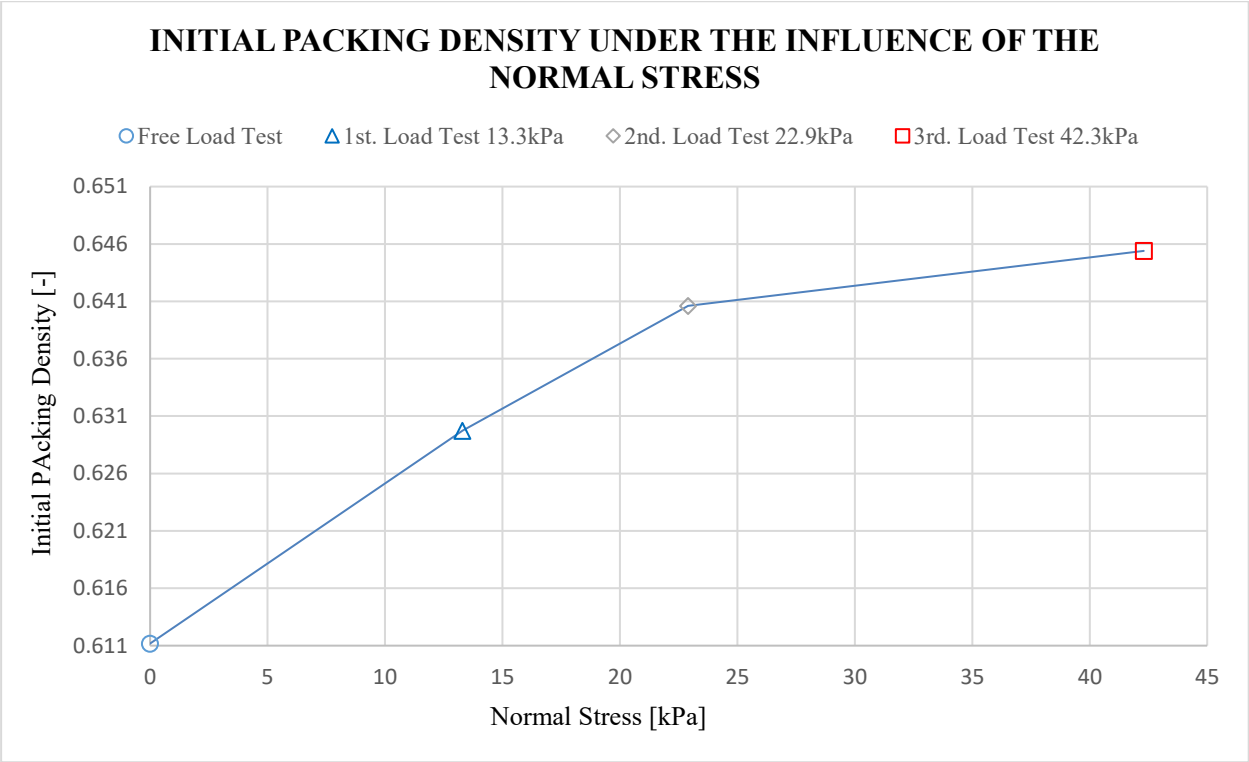

(a)

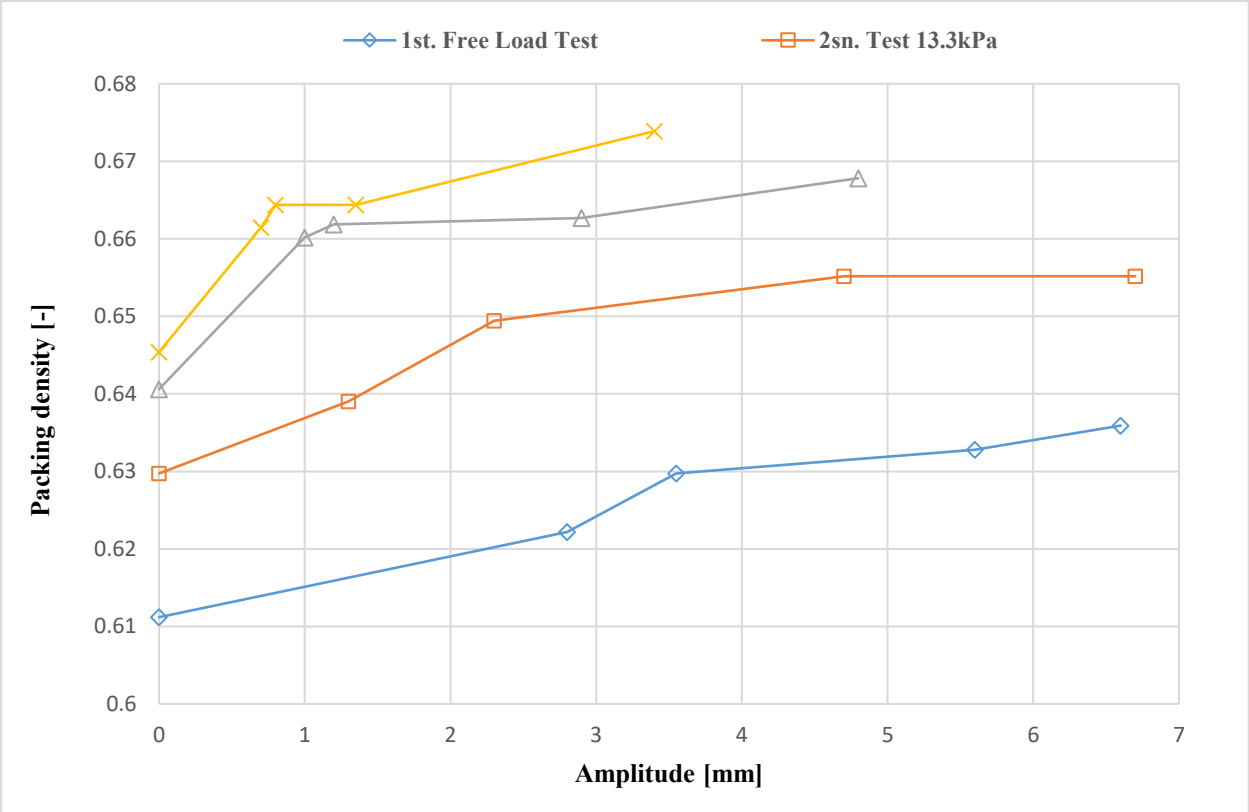

(b)

Figures 3.39a and b. The wheat packing density ρ vs the vibration amplitude A and the normal stress σ

Meanwhile, the "arch" and "bridge" configurations formed by the particles may undergo gradual breakage, leading to the development of a more stable structure, resulting in the highest packing

density of wheat. Similar trends can be observed in Figure 4.39, where an increase in vibration amplitude corresponds to achieving the densest packing structure. This finding is consistent with previous research that reported a similar outcome of high packing density with the combination of high vibration amplitude and low frequency (Zhao et al., 2019). This vibration amplitude and frequency effect has also been seen in other vibrated packing systems (Milewskl, 1978; Zhang et al., 2006; Li et al., 2011; An et al., 2015, 2016). Figure 4.40 further demonstrates the effect of normal stress on wheat packing density under the influence of vibration amplitude. The correlation pattern between vibration amplitude and packing density remains consistent for the loaded test, where higher normal stress results in sharper function lines. In contrast, the freeload test exhibits greater entropy due to the uncertain movement of particles, resulting in a deviation from the pattern of function lines observed in the loaded test, which is attributed to the absence of external normal stress. Furthermore, the loaded test shows a similar pattern of function lines due to the partial restriction of particle movement in the vertical direction due to the external normal stress.

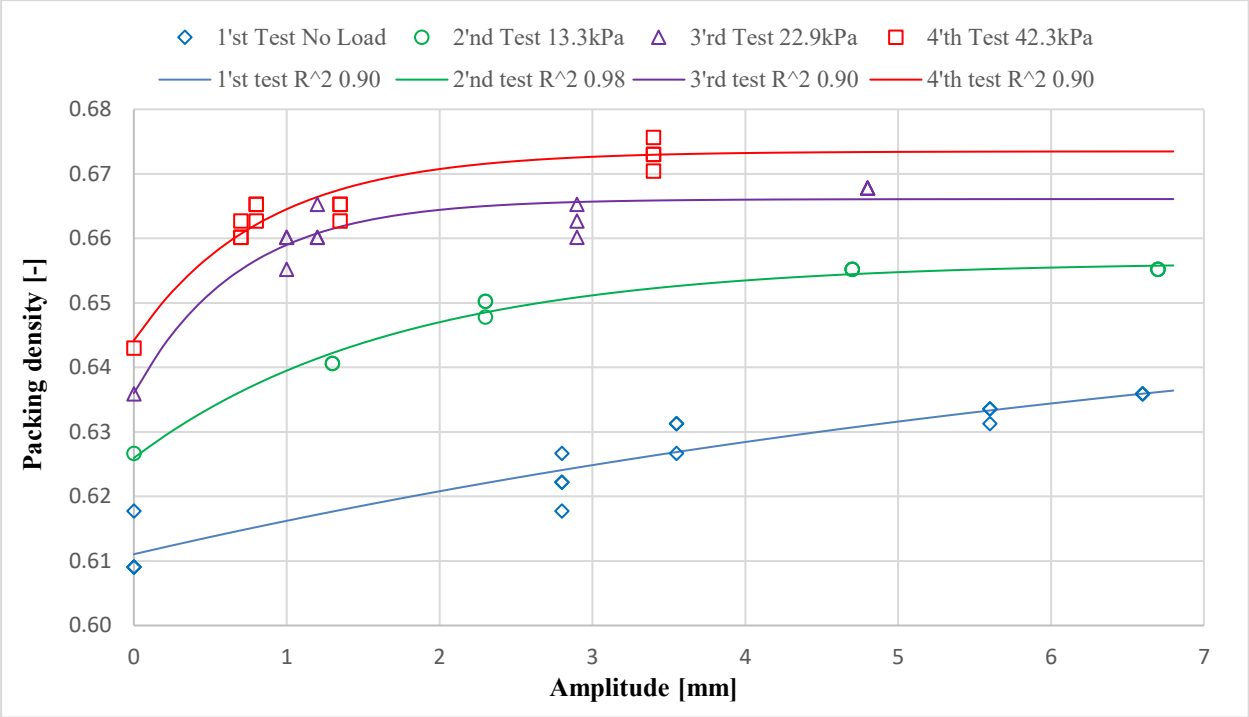

Figure 3.40. Wheat packing density ρ vs the vibration amplitude A

Another observed phenomenon is the increase in wheat packing density in response to the incremental application of external normal stress and amplitude until it remains constant. For instance, in tests conducted at 13.3 kPa, 22.9 kPa, and 42.3 kPa compared to the freeload test, the average wheat packing density increased by 3.1% for the 13.3 kPa test, 5.1% for the 22.9 kPa test, and 5.6% for the 42.3 kPa test. However, beyond a certain threshold, even with a doubling of the normal stress, the wheat packing density did not significantly increase, explaining the loss of the linearity behaviour of the function parameters as illustrated in Figures 4.39a and 4.40. The rearrangement of particles can explain this phenomenon by filling the voids between particles due to the presence of the vibration and increasing normal stress. Once the voids reach a minimum, no further increase in wheat packing density can be achieved, and the particles carry the excessive normal stress by themselves, resulting in compression of the wheat particles rather than rearrangement. Consequently, an exponential model was generated to describe the observed results, represented by Equation 4.6, which best fits the experimental data.

$$\rho_{(A)} = c_{51}\left(1 - e^{(-A\,c_{52})}\right) + \rho_i \qquad (3.6)$$

The amplitude-varying final packing density of wheat is denoted as $\rho_{(A)}$ [-], the initial wheat packing density is denoted by ρ_i [-], the function of the applied vibration amplitude A [mm], and influenced by two parameters c_{51} [-], c_{52} [mm^{-1}], which describes the relationship between the vibration amplitude and the exponential model, as illustrated in Figure 4.41 and Table 4.9.

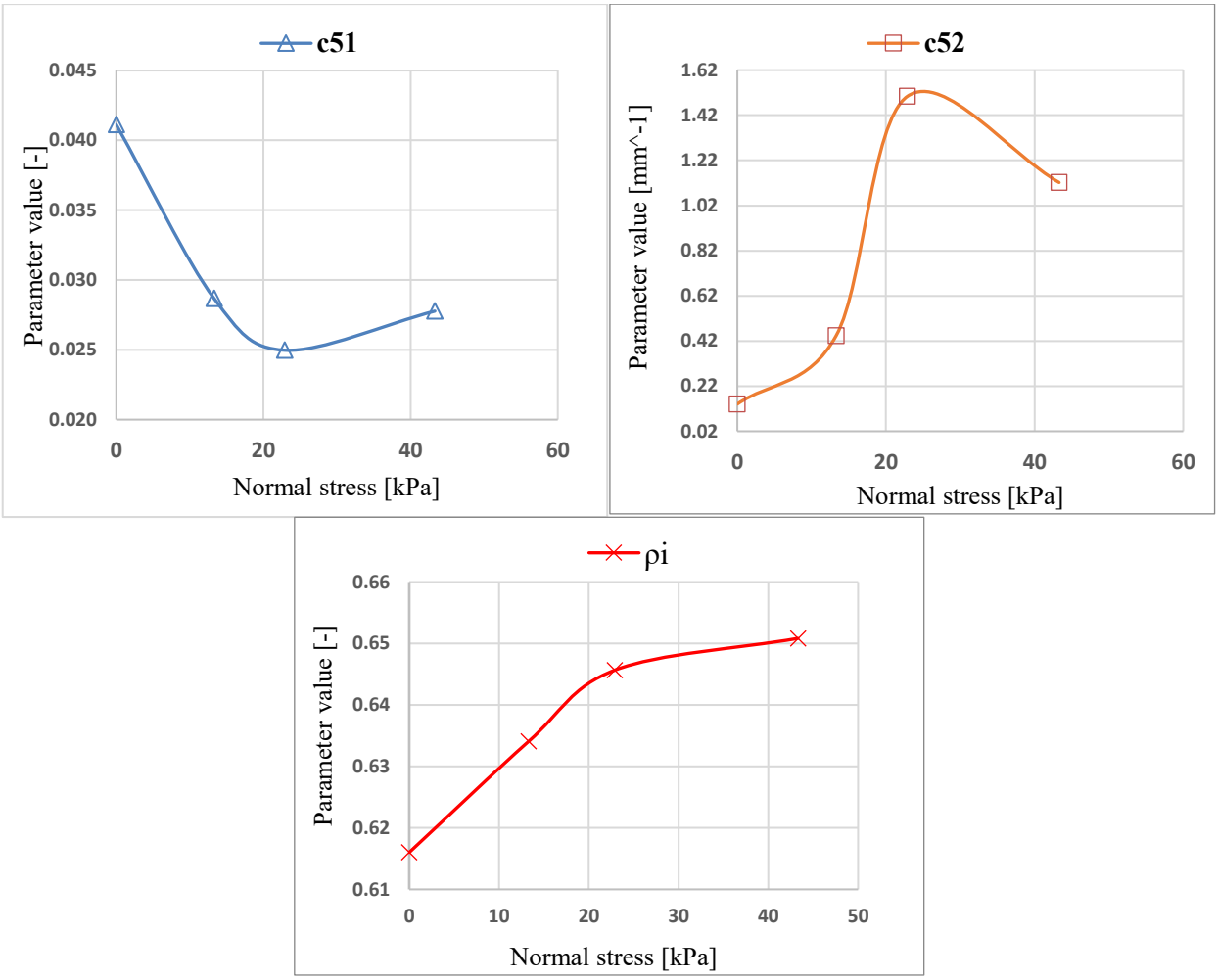

Figure 3.41. The exponential model obtained parameters.

Table 3.9. shows the parameters of the fitted exponential model.

Load	Constants			Correlation R^2
	c_{51}	c_{52}	ρ_i	
0 kPa	0.0411	0.1404 mm^{-1}	0.6110	0.9
13.3 kPa	0.0287	0.4434 mm^{-1}	0.6291	0.98
22.9 kPa	0.0249	1.5039 mm^{-1}	0.6406	0. 9
43.3 kPa	0.0278	1.1220 mm^{-1}	0.6458	0.9

In Figure 4.40, the value of $R^2 = 0.9$ represents the coefficient of determination, which assesses the goodness of fit of the regression model to the data points. An R^2 value of 0.9 suggests that the regression model can explain approximately 90% of the variability observed in the data. Generally, an R^2 value closer to 1 indicates a stronger fit of the model to the data, implying that the model effectively captures the variability in the data points. In this case, an R^2 value of 0.9 is considered high and indicative of a good fit of the regression model to the data.

Figure 4.41 illustrates the variation of the exponential model's parameters (c_{51}, c_{52}) concerning the external stress (σ). These parameters exhibit linear behaviour up to the stress limit of 23 kPa, beyond which nonlinearity becomes apparent. The values of these parameters are directly influenced by internal factors, such as particle micro-mechanical properties, shape, and size, and external factors, including σ and A. It can be inferred that varied materials have specific limitations in transitioning these parameters from linear to nonlinear behaviour. However, further experiments are needed to validate this conclusion. The physical interpretation of these parameters relates to the impact of σ on the curvature sharpness of the wheat ρ function lines. Precisely, decreases in c_{51} and increases in c_{52} under the influence of σ result in sharper exponential function curves, indicating higher wheat ρ values for the loaded tests than the freeloaded tests despite applying the same amplitude value.

3.8.3 Modell uncertainties and sensitivity

In light of the presented information, uncertainty analysis plays a pivotal role in comprehending the accuracy and reliability of the data obtained in our wheat packing density study. Using various analytical techniques, such as the Grubbs test, we identified and eliminated outliers from the dataset, thus ensuring the utmost precision in our results. As depicted in Figure 4.42, the uncertainty of wheat packing density is illustrated for different applications of normal stress with the applied amplitude, and the highlighted area within the fitted line represents the corrected standard deviation for the collected data. It is noteworthy that sensitivity analysis is also paramount in assessing the influence of diverse parameters on the obtained outcomes. By conducting a comprehensive uncertainty and sensitivity analysis, we can establish the robustness and reliability of our findings, thereby providing valuable insights for future research and practical applications in this field. The subsequent figures display the uncertainty of wheat packing density ρ versus the vibration amplitude A for various scenarios, including the freeload test, 13.3kPa, 22.9kPa, and 42.3kPa (Figures 4.42 a, b, c, d, respectively).

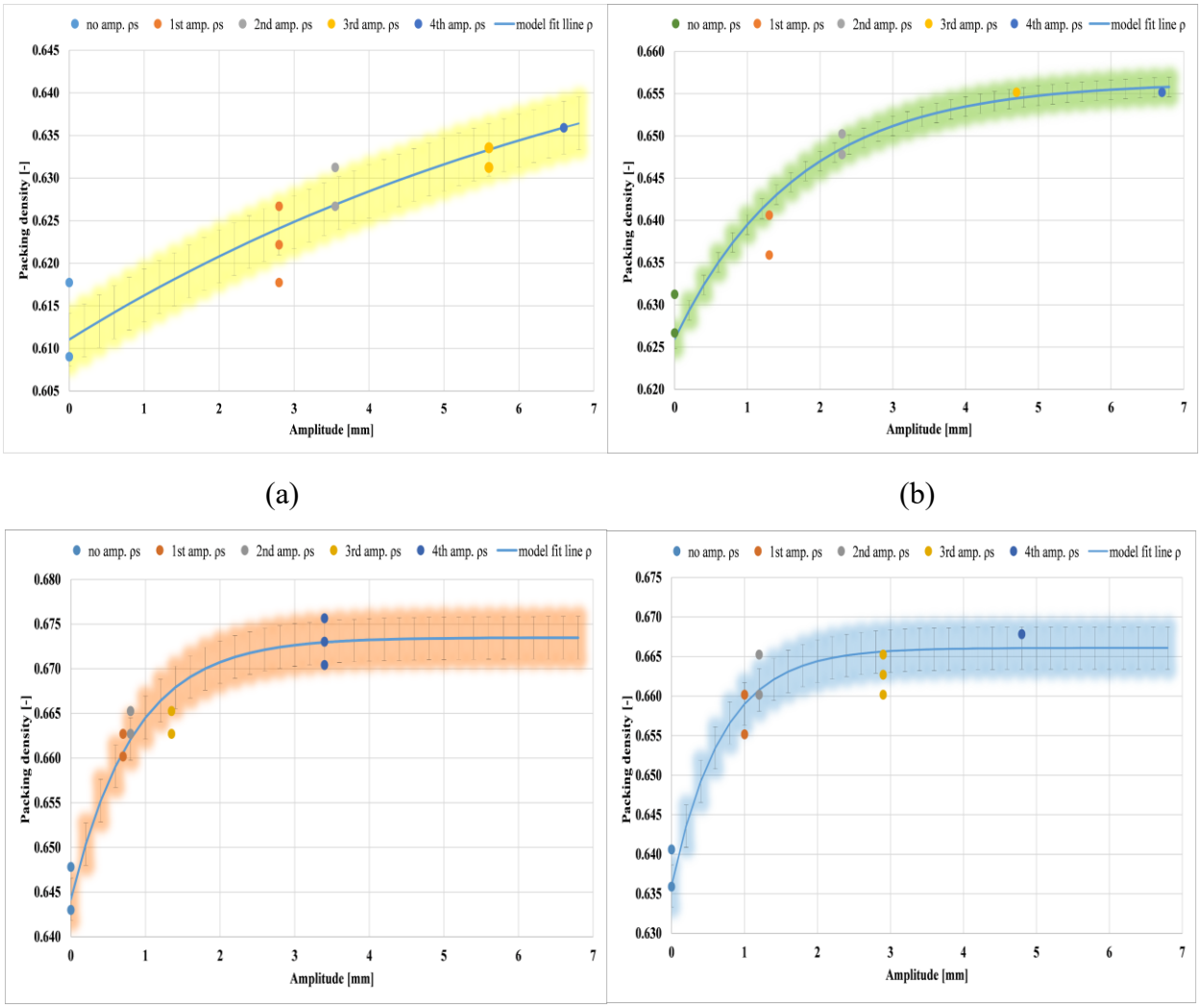

Figure 3.42. The uncertainty of wheat packing density ρ vs the vibration amplitude A for four different normal stresses

In our investigation of wheat packing density, we employed a sensitivity analysis using the Morris method, which involves systematically varying the model's input parameters within predefined ranges and observing the resulting output. The Morris indices were calculated to quantify the sensitivity of the model output to each input parameter, and these indices were ranked to determine their relative importance (ρ_i: 40.47%, A: 31.52%, c_{52}: 15.60%, c_{51}: 12.40%). As represented by Equation 4.6, the model can be divided into two sections. The initial term in the model, c_{51} * (1 - exp (-A * c_{52})), is susceptible to amplitude A, which exhibits a wide range of values (0 to 6.7 mm). However, the parameters c_{52} (ranging from 0.123 to 1.33) and c_{51} (ranging from 0.027 to 0.0448), with their narrower ranges, have a lesser effect on the outcome. The second section pertains to the input parameter ρ_i (ranging from 0.61 to 0.645), which establishes the baseline value for the model and exhibits the highest sensitivity among all input parameters, as supported by Figure 4.43. The sensitivity analysis used the Morris method Python code for 10,000 iterations to ensure robust analysis. These insights provide a valuable understanding of the factors influencing wheat packing density and can be used to optimise the packing process. The Morris method-based sensitivity analysis facilitates informed decision-making and recommendations for further research in this field.

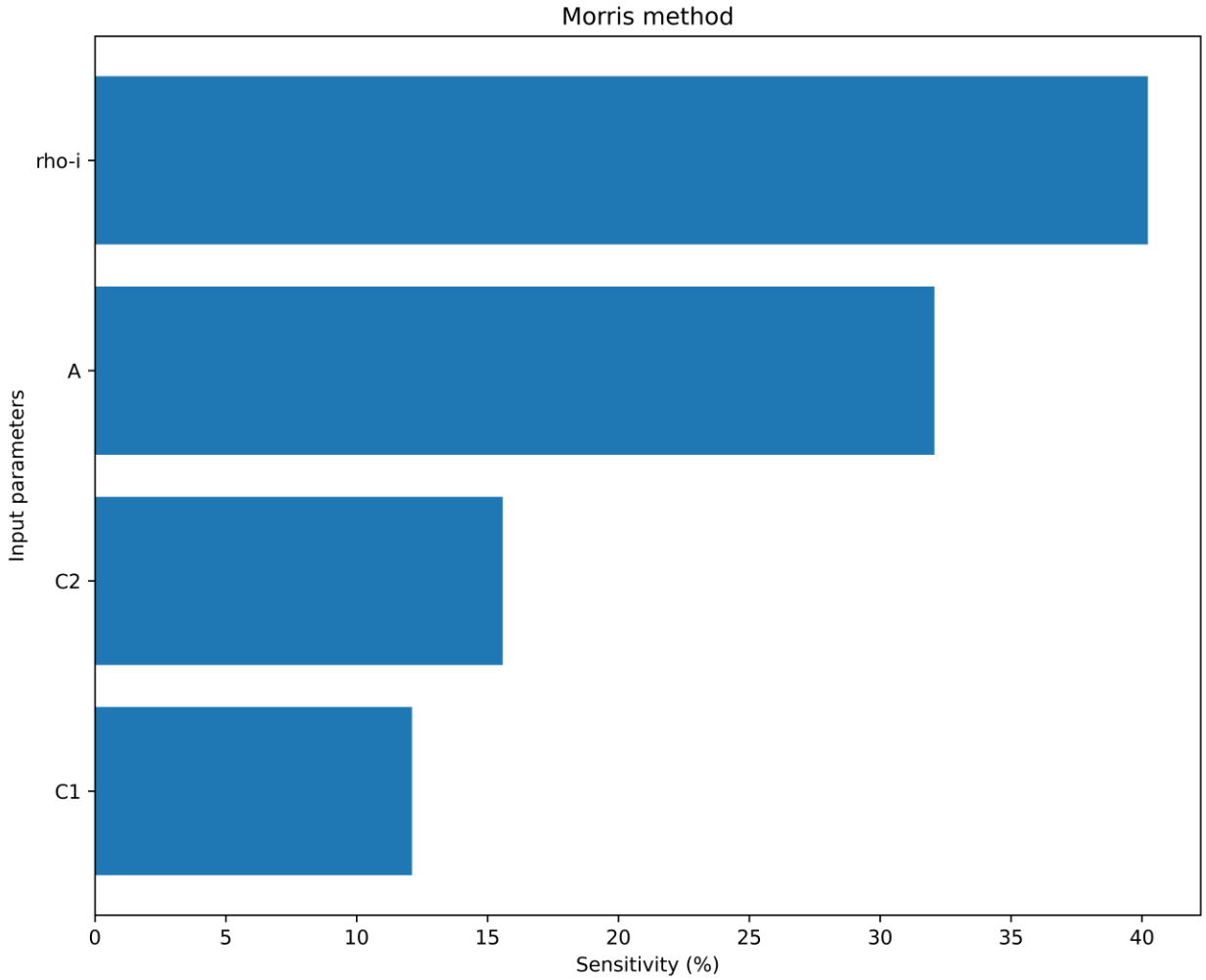

Figure 3.43. The sensitivity order of the input parameters.

4 CONCLUSION AND RECOMMENDATIONS

4.1 Decoding Granular Material Behaviour: Particle Shape and Mechanical Insights

In our exploration of granular material behaviour, the influence of particle shape, characterised by the Sphericity Index (SPH), Aspect Ratio (AR), Size Index (SI), and Triple Particle Size Index (TPSI), profoundly shapes mechanical responses. This study delves into how these shape factors affect mechanical aspects, including shear stress, volumetric strain, average contact numbers, contact force chains, shear zones, and particle rotation. By understanding these relationships, we illuminate the complex interplay between particle geometry, stress, and various mechanical behaviours in granular materials.

This study investigated the influence of various particle indices on the mechanical behaviour of granular materials, focusing on particle shape's crucial role in shaping their response. The sphericity index (SPH) proved a significant factor, with lower values leading to enhanced interlocking and increased shear strength. This effect was further amplified by higher normal stresses, highlighting the importance of particle shape under these conditions. An exponential model based on the aspect ratio (AR) effectively captured this non-linear relationship, demonstrating its potential for predicting shear behaviour. The size index (SI) and triple particle size index (TPSI) also positively correlated with internal friction angle and shear strength. Larger particles, with increased contact points and effective stress transfer area, displayed superior resistance to deformation and displacement, contributing to their more substantial shear characteristics. These findings underscore the significant impact of particle indices, particularly

shape, on the mechanical behaviour of granular materials. They provide valuable insights for researchers and engineers working with these materials in various applications.

This study delved further into the influence of particle indices on granular materials, focusing on their impact on volumetric strain. The sphericity index (SPH) played a key role, with lower values leading to increased dilatancy, particularly under higher normal stresses. Suggests a strong correlation between particle shape and dilation behaviour under varying loading conditions. Assemblies with more elongated particles exhibited significantly higher dilation compared to spherical ones. Similarly, the size index (SI) and triple particle size index (TPSI) displayed positive correlations with dilation, indicating that larger particles generally experienced more significant volume expansion. Higher TPSI values further amplified this effect, highlighting the combined influence of particle size and shape on volumetric response.

Interestingly, normal stress consistently exhibited an inverse relationship with dilation, with higher stress leading to lower volume expansion across all particle index variations. These findings unveil the complex interplay between particle indices, normal stress, and volumetric strain, providing valuable insights into the behaviour of granular materials under various loading conditions. They can inform researchers and engineers working with these materials in applications requiring control over deformation and volume change.

This study further examined the impact of particle indices on the mechanical behaviour of granular materials, specifically focusing on their influence on average contact numbers (CN). The sphericity index (SPH) exhibited a clear inverse relationship with CN, with lower SPH leading to increased contact numbers. This finding aligns with previous research on elliptical particles and highlights the intricate interplay between particle shape and contact formation. Interestingly, both size index (SI) and triple particle size index (TPSI) did not significantly impact CN, suggesting that particle size variations primarily affect shape features rather than inherent sphericity. This observation contributes to understanding the stability of particle connections within the assembly. Nevertheless, high stress consistently increased CN for all indices, emphasising its role in promoting contact points. These findings reveal the complex interplay between particle shape, size, and stress in shaping contact number characteristics. Understanding these interactions is crucial for predicting the behaviour of granular materials in various applications, such as powder flow and soil mechanics, where contact formation plays a critical role in material properties and performance.

This study delved deeper into the influence of particle indices on the dynamics of contact force chains in granular materials under shear stress. The sphericity index (SPH) played a crucial role, with lower SPH values leading to stronger contact forces and a more robust network. Aligns with the observed concentration of forces near the shear zone in these samples, facilitating effective load transmission. Interestingly, lower SPH values exhibited higher shear forces due to the formation of distinct shear bands, suggesting alternative force transmission mechanisms. The size index (SI) also significantly impacted contact forces. Larger particles (higher SI) exhibited enhanced interlocking and stronger force chains, leading to greater shear strength and stability. These samples' increased contact area and efficient force transmission were attributed to them. Similarly, the triple particle size index (TPSI) positively correlated with force chain strength and stability. Higher TPSI values resulted in rougher interlocking, contributing to stronger force chains and influencing shear band formation. These findings highlight the complex interplay between particle shape, size, and contact force chain dynamics under shear stress. Understanding these interactions is essential for predicting and controlling the behaviour of granular materials in various applications, such as soil mechanics and powder flow, where force chains play a critical role in material properties and performance.

This study further explored the impact of particle indices on the formation and characteristics of shear zones in granular materials under shear stress. The sphericity index (SPH) played a

significant role, with lower SPH values (non-rounded particles) leading to decreased average particle rotation and thinner shear bands. It suggests a link between particle shape and shear zone localisation, with stronger interlocking and less rotation, facilitating efficient load transfer in less-rounded materials. Notably, a reduction in average rotation coincided with increased shear strength, highlighting the influence of particle shape on mechanical behaviour. The size index (SI) also exhibited an apparent effect, with larger particles (higher SI) exhibiting reduced average rotation and wider shear bands. They are attributed to the increased contact area and interlocking in larger particles, promoting more efficient stress transfer and stabilisation of the shear zone. Similarly, the triple particle size index (TPSI) positively correlated with reduced particle rotation and wider shear bands. Again, this suggests a link between particle size and shear zone formation, with larger size distributions influencing interlocking and load transfer within the shear zone. These findings demonstrate the complex interplay between particle shape, size, and shear zone dynamics, highlighting the importance of considering these factors when predicting and controlling the behaviour of granular materials in various applications. Understanding these interactions is crucial for optimising soil mechanics, powder flow, and geotechnical engineering performance, where shear zone behaviour significantly impacts material properties and stability.

This comprehensive study unravels the multifaceted relationship between particle shape, interlocking dynamics, and external stress in granular materials. These findings deepen our understanding of granular material behaviour and offer invaluable knowledge applicable to various fields, guiding more efficient and informed practices in fields ranging from construction to agriculture.

4.2 Dynamic Insights into Wheat Packing: Stress, Vibration, and Optimization

This study investigated the influence of vibration parameters (amplitude and duration) and normal stress on the packing density of wheat grains. The findings revealed a crucial interplay between these factors.

Vibration duration had a significant impact, with packing density reaching near completion within 3 seconds for freeloaded tests and 2 seconds for loaded tests. An exponential model effectively captured this time-dependent behaviour.

Vibration amplitude also played a key role, with higher amplitudes leading to denser packing. It was attributed to the gradual densification of loose structures and improved particle rearrangement. However, a threshold effect was observed, with loaded tests requiring lower amplitudes to achieve maximum packing density.

Normal stress further influenced packing density, increasing stress and leading to higher densities until a limiting value was reached. The filling of voids between particles and the compression limit of individual grains explained this phenomenon.

The exponential model effectively described the relationship between vibration amplitude, normal stress, and final packing density. The model parameters (c_{51} and c_{52}) exhibited a linear relationship with stress up to a specific threshold, suggesting material-specific limitations in their behaviour.

These findings provide valuable insights into the packing behaviour of granular materials under vibration and stress. They have potential applications in various fields, such as agricultural engineering, food processing, and pharmaceutical manufacturing, where optimising packing density is crucial for product quality and storage efficiency.

Moreover, our study incorporated uncertainty and sensitivity analyses, which are essential for ensuring the robustness and reliability of our findings. Utilising techniques such as the Grubbs test, outliers were identified and eliminated, enhancing the precision of our results. The sensitivity analysis, employing the Morris method, revealed the varying impacts of input parameters on wheat packing density. Notably, the initial term of the model, primarily influenced by vibration

amplitude, played a pivotal role, while the baseline value (ρ_i) exhibited the highest sensitivity value among the input parameters. These findings contribute to a nuanced understanding of wheat packing density and provide crucial information for optimising the packing process in agricultural and industrial applications.

This comprehensive exploration illuminates the intricate behaviours of wheat particles under external loads and lays the foundation for informed decision-making in agricultural practices and industrial applications. By elucidating the combined effects of everyday stress and mechanical vibration on wheat packing density, this study opens avenues for further research and practical implementations, ensuring the efficient handling and processing of granular materials in diverse fields.

4.3 Recommendations

Our research has revealed valuable insights into the particles' behaviour under varying stress conditions and the influence of particle shape indexes. Regarding the wheat packing density, critical parameters like c_{51} and c_{52} transition from linear to nonlinear behaviour beyond a stress limit of 23 kPa. We propose several recommendations for future research to enhance our understanding and effectively apply these findings.

To begin with, we encourage researchers to delve deeper into the effects of particle shape under dynamic stress scenarios. Granular materials' behaviour under changing, real-world stress conditions will provide a more comprehensive understanding of their response to external forces.

Furthermore, considering the multifaceted nature of particle geometry, additional research should focus on the influence of unexplored shape indexes and morphological parameters. A comprehensive evaluation of these factors will enrich our knowledge of how particle shape impacts material behaviour.

Moreover, it is crucial to investigate the impact of particle shape in diverse environmental conditions. The behaviour of granular materials may vary significantly under conditions like elevated temperatures, varying moisture levels, or particle crushing factors. Understanding these variations is essential, mainly when designing structures or systems exposed to such environmental factors.

Finally, while our research points to the nonlinear transition in c_{51} and c_{52} parameters, further experiments are vital to validate this conclusion. These experiments can help confirm the specific limitations of varied materials in transitioning from linear to nonlinear behaviour, contributing to a deeper understanding of granular material mechanics.

By following these recommendations, researchers can build upon our findings and advance the field's knowledge. They lead to more accurate predictions and practical applications of granular materials in various industries, from construction to geotechnical engineering.

5 NEW SCIENTIFIC RESULTS

1. This study has established a novel correlation between vibration amplitude (A) and wheat packing density (ρ). The findings demonstrate that vibration amplitude significantly determines wheat packing density, with higher A values leading to higher ρ values. This relationship is captured by an exponential model, as expressed in the following equation:

$$\rho_{(\mathrm{A})} = c_{51}\left(1 - \mathrm{e}^{(-A\,c_{52})}\right) + \rho_i$$

This model was validated for vibration amplitudes ranging from 0 to 6.7 mm and normal stresses ranging from 0 to 42.3 kPa. The model's ability to accurately predict wheat packing density across various conditions is valuable for optimising packing processes in multiple applications.

2. This study has established a novel correlation between the sphericity index (SPH) and shear stress behaviour in granular materials, focusing on particle shape influence. Among the three shape indexes investigated – sphericity particle shape index (SPH), size index (SI), and triple particle size index (TPSI) – SPH emerged as the most influential factor, directly impacting the interlocking between particles. Decreasing SPH from 100% to 81% resulted in a substantial 80% enhancement in shear strength, surpassing the contributions of SI and TPSI. The findings demonstrate that the sphericity index plays a significant role in determining shear stress, with lower SPH values leading to higher shear stress values due to increased particle interlocking. This relationship is captured by an exponential model, as expressed in the following equation:

$$T_{AR} = c_{12}\, N\, e^{(-AR\, c_{11})}$$

This model exhibits an impressive R-squared value of 0.96, confirming its remarkable ability to predict shear load under varying normal load conditions. The findings highlight the importance of particle shape in influencing the shear stress behaviour of granular materials, providing valuable insights for designing and optimising granular structures and processes.

3. This study has uncovered an inverse correlation between sphericity index (SPH) and volumetric strain in granular materials. The findings indicate that volumetric strain increases as SPH values decrease, suggesting that less spherical particles tend to exhibit more significant dilation. The following equation accurately describes this nonlinear relationship:

$$V_{SPH} = c_{31}\, SPH^2 + c_{32}\, SPH + c_{33}$$

This equation provides a valuable tool for predicting volumetric strain in granular systems with varying sphericity. The inverse correlation between SPH and V has essential implications for understanding the behaviour of granular materials in various applications, such as soil mechanics, civil engineering, and food processing.

4. This study uncovers a significant correlation between the size index (SI) and the shear stress behaviour of granular materials. The findings reveal a positive linear relationship between SI and shear stress, as evidenced by the high R-squared value. Indicates that a corresponding rise in shear stress accompanies increased SI. This correlation is well-described by linear regression equations, as expressed in the following equation:

$$T_{SI} = SI\, c_{21} + N\, c_{22}$$

This finding highlights the importance of SI in influencing the shear stress behaviour of granular materials. It suggests that the size distribution of particles plays a crucial role in determining their resistance to shearing loads. This understanding is essential for designing and optimising granular structures and processes, such as packing, compaction, and filtration.

5. This study has unveiled a significant impact of size index (SI) on the volumetric strain behaviour of granular materials. The findings reveal a positive linear correlation between SI and volumetric strain, indicating that an increase in SI leads to an increase in volumetric strain. The following equation captures this relationship:

$$V_{SI} = c_{41}\, SI + c_{42}$$

This correlation holds for a wide range of SI values, as evidenced by the regression model's high R-squared value. This finding is significant because it can provide insights into the behaviour of granular materials under varying conditions.

6. This study has identified a critical threshold for vibration amplitude (A) and external normal stress (σ) that maximises wheat packing density (ρ), as shown in Figure 4.40. Beyond this threshold, further vibration amplitude or normal stress increases do not significantly enhance packing density. Once voids between particles are fully occupied due to rearrangement induced by vibration and increasing normal stress, additional stress primarily leads to compression rather than rearrangement, resulting in a plateauing of packing density. Moreover, an intriguing threshold effect of vibration amplitude (A) on

wheat packing density (ρ) under different loading conditions has been revealed. Freeload tests demonstrated that the influence of vibration amplitude was only observed once it exceeded a specific threshold value. In contrast, loaded tests showed that even small vibration amplitudes (A) significantly impacted wheat packing density (ρ), as illustrated in Figure 4.38. This observation underscores the complex interplay between vibration amplitude, external normal stress, and wheat packing density, highlighting the critical thresholds that govern the densification process in granular materials.

7. This study has uncovered a novel finding regarding the effect of external normal stress (σ) on stabilising wheat packing density (ρ). The results demonstrate that external normal stress expedites the process of ρ reaching a stable value. This acceleration is attributed to the enhanced particle rearrangement facilitated by the applied normal stress. Within the experimental timeframe, the loaded test, subjected to external normal stress, reached the final stable ρ significantly faster (2 s) than the freeloading test (3 s), which operated without external normal stress. This observation underscores the significant role of external normal stress in accelerating the packing densification process and highlights its potential for enhancing the efficiency of wheat storage and handling operations.
8. This study has unveiled a notable non-linear pattern in the exponential model parameters (c_{51}, c_{52}, ρ_i) governing the relationship between vibration amplitude (A) and wheat packing density (ρ) across varying normal stresses (σ). The investigation reveals that the linear trend of these parameters ceases beyond a stress threshold of 23 kPa. This deviation from linearity is ascribed to internal and external factors impacting the parameters' values. Internal factors encompass the mechanical and physical properties of the wheat particles themselves, while external factors include normal stress and vibration amplitude. As depicted in Figures 4.38 and 4.40, the packing density nearly reaches its final value at the 23 kPa limit. Therefore, further increases in normal stress have diminishing effects on packing density, even with a doubling of the normal stress, elucidating the non-linear behaviour observed. This non-linearity manifests in the function lines curvature sharpness of the wheat packing density, as demonstrated in Figure 4.40. Higher σ values yield sharper curves, indicating higher wheat ρ values for loaded tests than freeloading tests despite applying the same amplitude value. This non-linear trend underscores the intricate relationship between vibration amplitude, normal stress, and wheat packing density.

6 SUMMARY

This study delves into the intricate dynamics of particle behaviour in granular materials, focusing on critical parameters such as sphericity index, particle size, and mechanical vibrations. The investigation aimed to comprehensively understand these factors' influences, thereby optimising industrial processes and achieving optimal packing density. The research begins by providing an insightful introduction, highlighting the importance of granular materials in various industrial applications. It delineates the scope of the study, emphasising the criticality of understanding the mechanical behaviour of particles for practical applications.

Moving into the literature review, a thorough exploration of existing knowledge illuminates the gaps in understanding, emphasising the need for detailed research in areas such as particle interlocking, shape indexes, and the impact of external loads. This review contextualises the current study and underlines the significance of the research objectives in advancing the field's knowledge.

The core of the study lies in its meticulous experiments and analyses. This study investigates the influence of particle sphericity index SPH and double particle size index SI on granular material behaviour, and the research provides novel insights into the Simple Shear Test (SST) outcomes. The triple particle size index TPSI examination further enriches this understanding, contributing valuable data to the field's body of knowledge. Additionally, this study ventures into the synergistic

impact of mechanical vibration and normal stress on wheat particles' packing density. The results highlight the delicate balance between these loads, demonstrating the intricate relationship between vibration amplitude, normal stress, and wheat packing density. Notably, an exponential model accurately captures these complex relationships, shedding light on the behaviour of wheat particles under external loads.

In the conclusion and recommendations section, the study synthesises its findings. It underscores the significance of both vibration amplitude and normal stress in influencing wheat packing density, revealing patterns that contribute substantially to the field's understanding. Incorporating uncertainty and sensitivity analyses ensures the robustness of the results, providing a methodological foundation for future research endeavours. The study concludes by emphasising the practical implications of these findings, envisioning optimised agricultural practices and enhanced industrial processes. It opens avenues for further research, underlining the potential for efficient handling and processing of granular materials across diverse applications.

This research illuminates the nuanced behaviours of granular materials under external loads, offering scientific insights and practical solutions. Its multidimensional approach, encompassing experimental precision, rigorous analyses, and practical implications, marks a significant contribution to the field, paving the way for innovative applications and informed decision-making in industries reliant on granular materials.

7 References

Al-Maharma, A. Y., Patil, S. P., and Markert, B. (2020): Effects of porosity on the mechanical properties of additively manufactured components: a critical review, Materials Research Express, 7(12), 122001

Alias, R., Kasa, A., and Taha, M. R. (2014): Particle size effect on shear strength of granular materials in direct shear test, International Journal of Civil and Environmental Engineering, 8(11), 1144–1147

Altuhafi, F. N., Coop, M. R., and Georgiannou, V. N. (2016): Effect of particle shape on the mechanical behavior of natural sands, Journal of Geotechnical and Geoenvironmental Engineering, 142(12), 4016071

An, X., Li, C., and Qian, Q. (2016): Experimental study on the 3D vibrated packing densification of binary sphere mixtures, Particuology, 27, 110–114

An, X. Z., He, S. S., Feng, H. D., and Qian, Q. (2015): Packing densification of binary mixtures of spheres and cubes subjected to 3D mechanical vibrations, Applied Physics A: Materials Science and Processing, 118(1), 151–162. https://doi.org/10.1007/S00339-014-8835-Z

Andrade, J. E., Chen, Q., Le, P. H., Avila, C. F., and Evans, T. M. (2012): On the rheology of dilative granular media: bridging solid-and fluid-like behavior, Journal of the Mechanics and Physics of Solids, 60(6), 1122–1136

Andreotti, B., Forterre, Y., and Pouliquen, O. (2013): *Granular media: between fluid and solid*. Cambridge University Press. Available at: https://www.cambridge.org/us/universitypress/subjects/physics/condensed-matter-physics-nanoscience-and-mesoscopic-physics/granular-media-between-fluid-and-solid?format=HB&isbn=9781107034792

Arthur, J. R. F., Bekenstein, S., Germaine, J. T., and Ladd, C. C. (1981): Laboratory shear strength of soil, ASTM Spec. Tech. Publ, 740

Asadi, R., and Mirghasemi, A. A. (2018): Numerical investigation of particle shape on mechanical behaviour of unsaturated granular soils using elliptical particles, Advanced Powder Technology,

29(12), 3087–3099. https://doi.org/10.1016/j.apt.2018.08.018

Baule, A., and Makse, H. A. (2014): Fundamental challenges in packing problems: from spherical to non-spherical particles, Soft Matter, 10(25), 4423–4429

Bertrand, F., Leclaire, L.-A., and Levecque, G. (2005): DEM-based models for the mixing of granular materials, Chemical Engineering Science, 60(8–9), 2517–2531

Bharathi, P., and Sampath kumar, T. (2022): Latest research and developments of ceramic reinforced magnesium matrix composites—A comprehensive review, Proceedings of the Institution of Mechanical Engineers, Part E: Journal of Process Mechanical Engineering, 09544089221126044

Bishop, A. W., and Henkel, D. J. (1962): The measurement of soil properties in the triaxial test

Börzsönyi, T., and Stannarius, R. (2013): Granular materials composed of shape-anisotropic grains, Soft Matter, 9(31), 7401–7418

Campbell, C. S. (2002): Granular shear flows at the elastic limit, Journal of fluid mechanics, 465, 261–291

Campbell, C. S. (2006): Granular material flows–an overview, Powder Technology, 162(3), 208–229

Cante, J. C., Riera, M. D., Oliver, J., Prado, J. M., Isturiz, A., and Gonzalez, C. (2011): Flow regime analyses during the filling stage in powder metallurgy processes: experimental study and numerical modelling, Granular matter, 13, 79–92

Chatham, C. A., Long, T. E., and Williams, C. B. (2019): A review of the process physics and material screening methods for polymer powder bed fusion additive manufacturing, Progress in Polymer Science, 93, 68–95

Chen, W., Yang, T., Dong, L., Elmasry, A., Song, J., Deng, N., Elmarakbi, A., Liu, T., Lv, H. B., and Fu, Y. Q. (2020): Advances in graphene reinforced metal matrix nanocomposites: Mechanisms, processing, modelling, properties and applications, Nanotechnology and Precision Engineering, 3(4), 189–210

Cheng, Y. P., Nakata, Y., and Bolton, M. D. (2003): Discrete element simulation of crushable soil, Geotechnique, 53(7), 633–641

Cividini, A., and Gioda, G. (1992): A finite element analysis of direct shear tests on stiff clays, International journal for numerical and analytical methods in geomechanics, 16(12), 869–886

Cleary, P. W. (2010): DEM prediction of industrial and geophysical particle flows, Particuology, 8(2), 106–118. https://doi.org/10.1016/j.partic.2009.05.006

Cleary, P. W., and Sawley, M. L. (2002): DEM modelling of industrial granular flows: 3D case studies and the effect of particle shape on hopper discharge, Applied Mathematical Modelling, 26(2), 89–111

Cui, L., and O'sullivan, C. (2006): Exploring the macro-and micro-scale response of an idealised granular material in the direct shear apparatus, Géotechnique, 56(7), 455–468

Cundall, P. A., and Strack, O. D. L. (1979): A discrete numerical model for granular assemblies, Géotechnique, 29(1), 47–65. https://doi.org/10.1680/geot.1979.29.1.47

DallaValle, J. M. (1948): Micromeritics: the technology of fine particles

Danesh, A., Mirghasemi, A. A., and Palassi, M. (2020): Evaluation of particle shape on direct shear mechanical behavior of ballast assembly using discrete element method (DEM),

Transportation Geotechnics, 23, 100357. https://doi.org/10.1016/j.trgeo.2020.100357

Danesh, A., Palassi, M., and Mirghasemi, A. A. (2018): Evaluating the influence of ballast degradation on its shear behaviour, International Journal of Rail Transportation, 6(3), 145–162. https://doi.org/10.1080/23248378.2017.1411212

DeGennes, P. G., Duran, J., and Reisinger, A. (2000): Sands, Powders, and Grains: An Introduction to the Physics of Granular Materials (Partially Ordered Systems). Springer, New York

DEM Solution. EDEM 2.7.0 User Guide. Edinburgh, United... - Google Scholar (no date): Available at: https://scholar.google.com/scholar?q=DEM Solution. EDEM 2.7.0 User Guide. Edinburgh%2C United Kingdom %282015%29 (Accessed: 26 November 2021)

Dołżyk-Szypcio, K. (2019): Direct Shear Test for Coarse Granular Soil, International Journal of Civil Engineering, 17(3), 1871–1878. https://doi.org/10.1007/s40999-019-00417-2

Estrada, N., Taboada, A., and Radjai, F. (2008): Shear strength and force transmission in granular media with rolling resistance, Physical Review E, 78(2), 21301

Fennis, S., Walraven, J. C., and Den Uijl, J. A. (2013): Compaction-interaction packing model: regarding the effect of fillers in concrete mixture design, Materials and structures, 46, 463–478

Fitzgerald, S. G., Delaney, G. W., and Howard, D. (2020): A review of jamming actuation in soft robotics, in Actuators. MDPI, 104

Gámez, F., Acemel, R. D., and Cuetos, A. (2013): Demixing and nematic behaviour of oblate hard spherocylinders and hard spheres mixtures: Monte Carlo simulation and Parsons-Lee theory, Molecular Physics, 111(20), 3136–3146. https://doi.org/10.1080/00268976.2013.771802

Garneoui, S. (2020): Mixing Enhancement of Wheat Granules in a Hopper Bottom Lab-Scale Mixer Using Discrete Element Simulations, 868–873. https://doi.org/10.5937/fme2004868G

de Gennes, P.-G. (1999): Granular matter: a tentative view, Reviews of modern physics, 71(2), S374

German, R. M. (1989): Particle Packing ChaGerman, R. M. (1989). Particle Packing Characteristics Metal Powder Industries Federation. Princeton, New Jersey.racteristics Metal Powder Industries Federation, Princeton, New Jersey

German, R. M. (1994): Powder metallurgy science, metal powder industries federation, New Jersey, 69

Gingold, R. A., and Monaghan, J. J. (1977): Smoothed particle hydrodynamics: theory and application to non-spherical stars, Monthly notices of the royal astronomical society, 181(3), 375–389

Gong, J., and Liu, J. (2017): Effect of aspect ratio on triaxial compression of multi-sphere ellipsoid assemblies simulated using a discrete element method, Particuology, 32, 49–62. https://doi.org/10.1016/j.partic.2016.07.007

Green, G. E., and Reades, D. E. (1975): Boundary conditions, anisotropy and sample shape effects onthe stress-strain behaviour of sand in triaxial compression and plane strain, Geotechnique, 25(2), 333–356

Guo, P. (2008): Modified direct shear test for anisotropic strength of sand, Journal of Geotechnical and Geoenvironmental Engineering, 134(9), 1311–1318

Hayta, M., and Hendek Ertop, M. (2018): Evaluation of microtextural properties of sourdough wheat bread obtained from optimized formulation using scanning electron microscopy and image

analysis during shelf life, Journal of food science and technology, 55(1), 1–9

Hertz, H. (1881): Ueber den kontakt elastischer koerper, J. Reine Angew. Math, 92(156)

Hinrichsen, H., and Wolf, D. E. (2004): *The Physics of Granular Media*

Huang, H. (2010): *Discrete element modeling of railroad ballast using imaging based aggregate morphology characterization*. University of Illinois at Urbana-Champaign

Hudson, D. R. (1947): Packing of Materials in Bulk, Machinery, 70, 617–622

Idelsohn, S. R., Oñate, E., and Del Pin, F. (2003): A Lagrangian meshless finite element method applied to fluid–structure interaction problems, Computers & Structures, 81(8–11), 655–671

Idelsohn, S. R., Oñate, E., and Pin, F. Del (2004): The particle finite element method: a powerful tool to solve incompressible flows with free-surfaces and breaking waves, International journal for numerical methods in engineering, 61(7), 964–989

Ishihara, K. (1996): Soil behaviour in earthquake geotechnics

Jaeger, J. C., Cook, N. G. W., and Zimmerman, R. (2009): *Fundamentals of rock mechanics*. John Wiley & Sons

Janssen (1895): Versuche uber getreidedruck in silozellen, ci.nii.ac.jp. Available at: https://ci.nii.ac.jp/naid/10029334428/ (Accessed: 16 June 2019)

Jasti, V. K., Marinack, M. C., Patil, D., and Fred Higgs III, C. (2019): The granular lubricated journal bearing: evidence of lift formation, Journal of Tribology, 141(4), 44503

Jenike, A. W. (1987): A theory of flow of particulate solids in converging and diverging channels based on a conical yield function, Powder Technology, 50(3), 229–236. https://doi.org/10.1016/0032-5910(87)80068-2

Ji, S., and Shen, H. H. (2006): Effect of contact force models on granular flow dynamics, Journal of engineering mechanics, 132(11), 1252–1259

Jing, L., and Stephansson, O. (2007): *Fundamentals of discrete element methods for rock engineering: theory and applications*. Elsevier

Johanson (1965): Method of calculating rate of discharge from hoppers and bins, ci.nii.ac.jp. Available at: https://ci.nii.ac.jp/naid/20000744915/ (Accessed: 16 June 2019)

Johnson, K. L. (1972): Rolling resistance of a rigid cylinder on an elastic-plastic surface, International Journal of Mechanical Sciences, 14(2), 145–148

Jovičić, V., Coop, M. R., and Simić, M. (1996): Objective criteria for determining G max from bender element tests, Géotechnique, 46(2), 357–362

Kaye, B. H. (2008): *A random walk through fractal dimensions*. John Wiley & Sons

Keppler, I., Kocsis, L., Oldal, I., Farkas, I., and Csatar, A. (2012a): Grain velocity distribution in a mixed flow dryer, Advanced Powder Technology, 23(6), 824–832. https://doi.org/10.1016/j.apt.2011.11.003

Keppler, I., Kocsis, L., Oldal, I., Farkas, I., and Csatar, A. (2012b): Grain velocity distribution in a mixed flow dryer, Advanced Powder Technology, 23(6), 824–832. https://doi.org/10.1016/j.apt.2011.11.003

Keppler, I., Varga, A., Szabo, I., Katai, L., and Fenyvesi, L. (2016): Particle motion around open mixing screws: optimal screw angular velocity, Engineering Computations, 33(3)

Kiełbasa, K., Sreńscek-Nazzal, J., and Michalkiewicz, B. (2021): Impact of tailored textural properties of activated carbons on methane storage, Powder Technology, 394, 336–352

Knight, J. B., Fandrich, C. G., Lau, C. N., Jaeger, H. M., and Nagel, S. R. (1995): Density relaxation in a vibrated granular material, Physical Review E, 51(5), 3957–3963. https://doi.org/10.1103/PHYSREVE.51.3957

Kodicherla, S. P. K., Gong, G., Yang, Z. X., Krabbenhoft, K., Fan, L., Moy, C. K. S., and Wilkinson, S. (2019): The influence of particle elongations on direct shear behaviour of granular materials using DEM, Granular Matter, 21(4), 1–12. https://doi.org/10.1007/s10035-019-0947-x

Kruggel-Emden, H., Stepanek, F., and Munjiza, A. (2010): A study on adjusted contact force laws for accelerated large scale discrete element simulations, Particuology, 8(2), 161–175

Kuo, H.-P. (2001): Numerical and experimental studies in the mixing of particulate material, The University of Birmingham, UK

Kuwano, R., Connolly, T. M., and Jardine, R. J. (2000): Anisotropic stiffness measurements in a stress-path triaxial cell, Geotechnical Testing Journal, 23(2)

Li, C. X., An, X. Z., Yang, R. Y., Zou, R. P., and Yu, A. B. (2011): Experimental study on the packing of uniform spheres under three-dimensional vibration, Powder technology, 208(3), 617–622

Li, L., Chen, Y., Yang, L., Wang, Z., and Liu, H. (2020): Recent advances in applications of metal–organic frameworks for sample preparation in pharmaceutical analysis, Coordination Chemistry Reviews, 411, 213235

Lim, W. L., and McDowell, G. R. (2005): Discrete element modelling of railway ballast, Granular Matter, 7, 19–29

Liu, S. H. (2006): Simulating a direct shear box test by DEM, Canadian Geotechnical Journal, 43(2), 155–168

Lucy, L. B. (1977): A numerical approach to the testing of the fission hypothesis, Astronomical Journal, vol. 82, Dec. 1977, p. 1013-1024., 82, 1013–1024

Luerkens, D. W. (1991): *Theory and application of morphological analysis: fine particles and surfaces*. CRC press

Ma, H., Zhou, L., Liu, Z., Chen, M., Xia, X., and Zhao, Y. (2022): A review of recent development for the CFD-DEM investigations of non-spherical particles, Powder Technology, 117972

Mahmood, Z., and Iwashita, K. (2011): A simulation study of microstructure evolution inside the shear band in biaxial compression test, International Journal for Numerical and Analytical Methods in Geomechanics, 35(6), 652–667. https://doi.org/10.1002/nag.917

Merkus, H. G., and Merkus, H. G. (2009): Particle size, size distributions and shape, Particle Size Measurements: Fundamentals, Practice, Quality, 13–42

Milewski, J. V (1973): A study of the packing of milled fibreglass and glass beads, Composites, 4(6), 258–265

Milewskl, J. V. (1978): The Combined Packing of Rods and Spheres in Reinforcing Plastics, Industrial and Engineering Chemistry Product Research and Development, 17(4), 363–366. https://doi.org/10.1021/I360068A016

Mindlin, R. D. (1949): Compliance of elastic bodies in contact

Mindlin, R. D., and Deresiewicz, H. (1953): Elastic spheres in contact under varying oblique forces

Minglani, D., Sharma, A., Pandey, H., Dayal, R., Joshi, J. B., and Subramaniam, S. (2020): A review of granular flow in screw feeders and conveyors, Powder Technology, 366, 369–381

Mishra, B. K. (2003): A review of computer simulation of tumbling mills by the discrete element method: part I—contact mechanics, International journal of mineral processing, 71(1–4), 73–93

Mishra, B. K., and Murty, C. V. R. (2001): On the determination of contact parameters for realistic DEM simulations of ball mills, Powder Technology, 115(3), 290–297

Mitarai, N., and Nori, F. (2006): Wet granular materials, Advances in Physics, 55(1–2), 1–45

Nedderman, R. M. (1992): *Statics and kinematics of granular materials*. Cambridge University Press Cambridge

Neumann, B. S. (1953): Flow Properties of Disperse Systems, Chap. X, ed. by JJ Hermans (Leiden)

Obert, L., Brady, B. T., and Schmechel, F. W. (1976): The effect of normal stiffness on the shear resistance of rock, Rock mechanics, 8, 57–72

Oda, M., and Iwashita, K. (1999): An Introduction mechanics of granular materials, AA BALKEMA, (1), 1–5

Oda, M., and Kazama, H. (1998): Microstructure of shear bands and its relation to the mechanisms of dilatancy and failure of dense granular soils, Géotechnique, 48(4), 465–481. https://doi.org/10.1680/geot.1998.48.4.465

Oldal, I., and Safranyik, F. (2015): Extension of silo discharge model based on discrete element method, Journal of Mechanical Science and Technology, 29(9), 3789–3796. https://doi.org/10.1007/s12206-015-0825-3

Oñate, E., Idelsohn, S. R., Del Pin, F., and Aubry, R. (2004): The particle finite element method—an overview, International Journal of Computational Methods, 1(02), 267–307

Pennington, D. S., Nash, D. F. T., and Lings, M. L. (2001): Horizontally mounted bender elements for measuring anisotropic shear moduli in triaxial clay specimens, Geotechnical testing journal, 24(2), 133–144

Peters, B., and Džiugys, A. (2002): Numerical simulation of the motion of granular material using object-oriented techniques, Computer methods in applied mechanics and engineering, 191(17–18), 1983–2007

Potts, D. M., Dounias, G. T., and Vaughan, P. R. (1987): Finite element analysis of the direct shear box test, Geotechnique, 37(1), 11–23

Pradhan, T. B. S., Tatsuoka, F., and Horii, N. (1988): Simple shear testing on sand in a torsional shear apparatus, Soils and Foundations, 28(2), 95–112

Qi, H., Zhou, G., Yu, F., Ge, W., and Li, J. (2015): Researches on mixing of granular materials with discrete element method, Progress in Chemistry, 27(1), 113

Qian, Q., An, X., Wang, Y., Wu, Y., and L Wang (2016): Physical study on the vibrated packing densification of mono-sized cylindrical particles, Particuology, 29, 120–125. https://doi.org/10.1016/j.partic.2016.01.009

R. L. BROWN, and RICHARDS, J. C. (1971): Principles of Powder Mechanics, Powder Technology, 4(2), 114. https://doi.org/10.1016/0032-5910(71)80014-1

Raji, A. O., and Favier, J. F. (2004): Model for the deformation in agricultural and food particulate materials under bulk compressive loading using discrete element method . I : Theory , model

development and validation, 64, 359–371. https://doi.org/10.1016/j.jfoodeng.2003.11.004

Di Renzo, A., and Di Maio, F. P. (2004): Comparison of contact-force models for the simulation of collisions in DEM-based granular flow codes, Chemical engineering science, 59(3), 525–541

Di Renzo, A., and Di Maio, F. P. (2005): An improved integral non-linear model for the contact of particles in distinct element simulations, Chemical engineering science, 60(5), 1303–1312

Richard, P., Nicodemi, M., Delannay, R., Ribiere, P., and Bideau, D. (2005): Slow relaxation and compaction of granular systems, Nature materials, 4(2), 121–128

Richards, J. C. (1966): *The Storage and Recovery of Particulate Solids: A Report of a Working Party of the Institution of Chemical Engineers*. Institution of Chemical Engineers

Richards, K., Bithell, M., Dove, M., and Hodge, R. (2004): Discrete–element modelling: methods and applications in the environmental sciences, Philosophical Transactions of the Royal Society of London. Series A: Mathematical, Physical and Engineering Sciences, 362(1822), 1797–1816

Rosenholm, J. B. (2023): Sizing and packing of particles–Characterization of mono-, di-and trimodal particle assemblies, Advances in Colloid and Interface Science, 102887

Rothenburg, L., and Bathurst, R. J. (1991): Numerical simulation of idealized granular assemblies with plane elliptical particles, Computers and Geotechnics, 11(4), 315–329. https://doi.org/10.1016/0266-352X(91)90015-8

Rothenburg, L., and Bathurst, R. J. (1992): Micromechanical features of granular assemblies with planar elliptical particles, Geotechnique, 42(1), 79–95. https://doi.org/10.1680/geot.1992.42.1.79

Saada, A. S., and Townsend, F. C. (1981): State of the art: laboratory strength testing of soils, Laboratory shear strength of soil, ASTM STP, 740, 7–77

Santamarina, J. C., and Cho, G.-C. (2004): Soil behaviour: The role of particle shape, in Advances in geotechnical engineering: The Skempton conference: Proceedings of a three day conference on advances in geotechnical engineering, organised by the Institution of Civil Engineers and held at the Royal Geographical Society, London, UK, on 29–31 . Thomas Telford Publishing, 604–617

Schofield, A. N., and Wroth, P. (1968): *Critical state soil mechanics*. McGraw-hill London

Schwager, T., and Pöschel, T. (1998): Coefficient of normal restitution of viscous particles and cooling rate of granular gases, Physical review E, 57(1), 650

Seville, J. P. K., Willett, C. D., and Knight, P. C. (2000): Interparticle forces in fluidisation: a review, Powder Technology, 113(3), 261–268

Seville, J. P., Tüzün, U., and Clift, R. (2012): *Processing of particulate solids*. Springer Science & Business Media

Smith, R., Frost, A., and Probert, P. J. (1997): Gyroscopic data fusion via a quaternion-based complementary filter, in Sensor Fusion: Architectures, Algorithms, and Applications. SPIE, 148–159

Syvitski, J. P. M. (1991): *Principles, methods, and application of particle size analysis*. Cambridge University Press Cambridge

Tabor, D. (1955): The mechanism of rolling friction II. The elastic range, Proceedings of the Royal Society of London. Series A. Mathematical and Physical Sciences, 229(1177), 198–220

Talafha, M. S., and Oldal, I. (2021): Evaluation the effect of particle sphericity on direct shear mechanical behavior of granular materials using discrete element method (DEM), International Journal for Engineering Modelling, 34(1), 1–18. https://doi.org/10.31534/engmod.2021.1.ri.01m

Talafha, M. S., and Oldal, I. (2022): The Effect of Triple Particle Sizes on the Mechanical Behaviour of Granular Materials using Discrete Element Method (DEM), FME Transactions, 50(1), 139–148. https://doi.org/10.5937/fme2201139T

Talafha, M. S., Oldal, I., and Garneoui, S. (2022): Study the particle size impact on the mechanical behaviour of granular material by discrete element method, FME Transactions, 50(3), 473–483

Tangri, H., Guo, Y., and Curtis, J. S. (2017): Packing of cylindrical particles: DEM simulations and experimental measurements, Powder Technology, 317, 72–82

Tejchman, J. (2005): FE analysis of shearing of granular bodies in a direct shear box, Particulate science and Technology, 23(3), 229–248

Thornton, C., and Zhang, L. (2003): Numerical simulations of the direct shear test, Chemical Engineering & Technology: Industrial Chemistry-Plant Equipment-Process Engineering-Biotechnology, 26(2), 153–156

Thornton, C., and Zhang, L. (2020): A DEM comparison of different shear testing devices, in Powders and Grains 2001. CRC Press, 183–190

Ting, J. M., Khwaja, M., Meachum, L. R., and Rowell, J. D. (1993): An ellipse-based discrete element model for granular materials, International Journal for numerical and analytical methods in geomechanics, 17(9), 603–623

Tsuji, Y., Kawaguchi, T., and Tanaka, T. (1993): Discrete particle simulation of two-dimensional fluidized bed, Powder technology, 77(1), 79–87

Tsuji, Y., Tanaka, T., and Ishida, T. (1992): Lagrangian numerical simulation of plug flow of cohesionless particles in a horizontal pipe, Powder technology, 71(3), 239–250

W. A. Beverloo, H. A. L. J. V. de velde (1961): The flow of granular magnesia, Journal of Pharmacy and Pharmacology, 18(7), 429–442. https://doi.org/10.1111/j.2042-7158.1966.tb07903.x

W. C. Krumbein (1941): Measurement and Geological Significance of Shape and Roundness of Sedimentary Particles, SEPM Journal of Sedimentary Research, Vol. 11(2), 64–72. https://doi.org/10.1306/d42690f3-2b26-11d7-8648000102c1865d

Wadell, H. (1932): Volume, shape, and roundness of rock particles, The Journal of Geology, 40(5), 443–451

Wang, D., and Abriak, N. E. (2015): Compressibility behavior of Dunkirk structured and reconstituted marine soils, Marine Georesources & Geotechnology, 33(5), 419–428

Wang, T., Zhang, F., Furtney, J., and Damjanac, B. (2022): A review of methods, applications and limitations for incorporating fluid flow in the discrete element method, Journal of Rock Mechanics and Geotechnical Engineering

Wang, W., Shen, A., Lyu, Z., He, Z., and Nguyen, K. T. Q. (2021): Fresh and rheological characteristics of fiber reinforced concrete——A review, Construction and Building Materials, 296, 123734

Wong, R. K. S., and Arthur, J. R. F. (1985): Induced and inherent anisotropy in sand, Geotechnique, 35(4), 471–481

Wood, D. M. (1990): *Soil behaviour and critical state soil mechanics*. Cambridge university press

Wornyoh, E. Y. A., Jasti, V. K., and Fred Higgs III, C. (2007): A review of dry particulate lubrication: powder and granular materials

Xie, Y. H., Yang, Z. X., Barreto, D., and Jiang, M. D. (2017): The influence of particle geometry and the intermediate stress ratio on the shear behavior of granular materials, Granular Matter, 19, 1–13

Yan, Z., Wilkinson, S. K., Stitt, E. H., and Marigo, M. (2015): Discrete element modelling (DEM) input parameters: understanding their impact on model predictions using statistical analysis, Computational Particle Mechanics, 2, 283–299

Yang, R. Y., Zou, R. P., and Yu, A. B. (2003): Microdynamic analysis of particle flow in a horizontal rotating drum, Powder Technology, 130(1–3), 138–146

Yang, Y., Wang, J. F., and Cheng, Y. M. (2016): Quantified evaluation of particle shape effects from micro-to-macro scales for non-convex grains, Particuology, 25, 23–35. https://doi.org/10.1016/j.partic.2015.01.008

Yang, Z. X., Yang, J., and Wang, L. Z. (2012): On the influence of inter-particle friction and dilatancy in granular materials: a numerical analysis, Granular matter, 14, 433–447

Yong, R. N. (1981): *Laboratory shear strength of soil: a symposium*. ASTM International

Yu, A. -B, Standish, N., and McLean, A. (1993): Porosity Calculation of Binary Mixtures of Nonspherical Particles, Journal of the American Ceramic Society, 76(11), 2813–2816. https://doi.org/10.1111/J.1151-2916.1993.TB04021.X

Yuan, Y., Liu, L., Zhuang, Y., Jin, W., and Li, S. (2018): Coupling effects of particle size and shape on improving the density of disordered polydisperse packings, Physical Review E, 98(4), 42903

Zenger, D. C., Cai, H., McNeill, J., and Ludwig, R. (1997): Classification strategy to identify and classify common cracks in green-state powdered metallurgy compacts, Review of Progress in Quantitative Nondestructive Evaluation: Volume 16A, 1443–1450

Zhang, C., Jian, X., and Lu, W. (2015): Structure and percolation of one-patch spherocylinders, Soft Matter, 11(7), 1362–1368

Zhang, W., Thompson, K. E., Reed, A. H., and Beenken, L. (2006): Relationship between packing structure and porosity in fixed beds of equilateral cylindrical particles, Chemical Engineering Science, 61(24), 8060–8074

Zhao, H., An, X., Qian, Q., Wu, Y., Wang, L., Li, W., and Yang, X. (2019): Experimental study on the packing densification of mixtures of spherical and cylindrical particles subjected to 3D vibrations, Particulate Science and Technology, 37(2), 251–260. https://doi.org/10.1080/02726351.2017.1373378

Zhou, Y. C., Wright, B. D., Yang, R. Y., Xu, B. H., and Yu, A. B. (1999): Rolling friction in the dynamic simulation of sandpile formation, 269, 536–553

Zuo, W., Zhang, L., Wei, L., Kong, X., and She, W. (2022): Effect of packing conditions and materials properties on loose packing fraction of rigid particles: a theoretical and experimental review, Journal of Sustainable Cement-Based Materials, 1–12

8 APPENDICES

Publications:

Title	Year	Quarter
The Combined Effect of Normal Stress and Mechanical Vibration on Wheat Packing Density MS Talafha, I Oldal Journal of Engineering Mechanics 150 (1), 04023111	2024	Q1
Study the particle size impact on the mechanical behaviour of granular material by discrete element method MS Talafha, I Oldal, S Garneoui FME Transactions 50 (3), 473-483	2022	Q2
The effect of Triple Particle sizes on the mechanical behaviour of granular materials using Discrete element method (DEM) MS Talafha, I Oldal FME Transactions 50 (1), 139-148	2022	Q2
Numerical study on the impact of particles filling pattern and screw parameters on the mixing uniformity of wheat grains in a screw mixer S Garneoui, I Keppler, P Korzenszky, MS Talafha Applied and Computational Mechanics 15 (2)	2021	Q4
Enhancement of Pulley and Belt Mechanism using Finite Element Analysis MS Talafha, I Oldal Journal of Engineering and Technology (JET) 12 (1), 33-52	2021	-
Evaluation the effect of particle sphericity on direct shear mechanical behavior of granular materials using discrete element method (DEM) MS Talafha, I Oldal International Journal for Engineering Modelling 34 (1 Regular Issue), 1-18	2021	Q4
Thermal analysis and improvement of pulley MS TALAFHA, I OLDAL Mechanical Engineering Letters, Szent István University, 136		-